

UNIVERSITÀ DEGLI STUDI DI FIRENZE  
Dipartimento di Fisica



**Tesi di Dottorato in Fisica – XX ciclo**  
**Settore disciplinare: FIS/03**

# **Ultracold bosonic mixtures: cold collisions and optical lattices**

*Dottorando:* Luigi De Sarlo

*Supervisore:* Prof. Massimo Inguscio

*Coordinatore:* Prof. Alessandro Cuccoli



# Contents

<b>Introduction</b>	<b>7</b>
<b>I A way to a Bose-Bose mixture</b>	<b>11</b>
<b>1 Theoretical framework</b>	<b>13</b>
1.1 How lasers can cool (and trap) atoms . . . . .	13
1.1.1 Laser cooling . . . . .	13
1.1.2 $^{87}\text{Rb}$ and K: level scheme . . . . .	15
1.1.3 Dipole traps and optical lattices . . . . .	17
1.2 Bose-Einstein condensation in trapped gases . . . . .	21
1.2.1 Ideal gas . . . . .	22
1.2.2 Interacting gas . . . . .	23
1.3 Two coupled condensates: topology of the ground state . . . . .	27
<b>2 Experimental apparatus</b>	<b>35</b>
2.1 Laser sources and vacuum apparatus . . . . .	36
2.1.1 Laser sources . . . . .	36
2.1.2 Vacuum apparatus . . . . .	38
2.2 The 2D-MOT . . . . .	43
2.2.1 General principle . . . . .	43
2.2.2 Experimental parameters . . . . .	45
2.2.3 Flux density measurement . . . . .	47
2.2.4 Loading of the mixed 3D-MOT . . . . .	49
2.2.5 Preparation of the atoms for magnetic trapping . . . . .	51
2.3 The magnetic millimetric trap . . . . .	52
2.3.1 General principle . . . . .	52
2.3.2 Mechanical structure . . . . .	54
2.3.3 Transfer from the 3D-MOT . . . . .	59
2.4 Evaporation and hyperfine transfer . . . . .	62

## 4 CONTENTS

---

2.5	Detection procedure . . . . .	65
2.5.1	Hardware setup . . . . .	67
2.5.2	Data analysis . . . . .	67
<b>II</b>	<b>Experiment with <math>^{39}\text{K}</math></b>	<b>71</b>
	<b>Introduction</b>	<b>73</b>
<b>3</b>	<b>Cold collisions</b>	<b>75</b>
3.1	$s$ -wave scattering in atoms . . . . .	75
3.1.1	Zero energy scattering . . . . .	78
3.1.2	Effective range approximation . . . . .	80
3.2	Feshbach-resonances . . . . .	82
<b>4</b>	<b>Collisional properties of <math>^{39}\text{K}</math></b>	<b>87</b>
4.1	Sympathetic cooling of $^{39}\text{K}$ with $^{87}\text{Rb}$ . . . . .	88
4.2	Measurement of the scattering length . . . . .	90
4.2.1	Cross-dimensional thermalization . . . . .	91
4.2.2	Determination of the triplet scattering length . . . . .	93
4.2.3	Numerical simulation . . . . .	98
<b>III</b>	<b>Experiments with <math>^{41}\text{K}</math>-<math>^{87}\text{Rb}</math> mixture</b>	<b>103</b>
	<b>Introduction</b>	<b>105</b>
<b>5</b>	<b>Bose-Einstein condensates in periodic potentials</b>	<b>107</b>
5.1	Non-interacting Bose-Einstein condensates . . . . .	107
5.1.1	Bloch bands . . . . .	108
5.1.2	Wannier picture . . . . .	110
5.2	The Bose-Hubbard model . . . . .	111
5.2.1	From Gross-Pitaevskii to Bose-Hubbard . . . . .	111
5.2.2	Phase diagram of the homogeneous system . . . . .	113
5.2.3	Inhomogeneous systems . . . . .	117
5.3	Two Bose-Einstein condensates in an optical lattice . . . . .	118
5.3.1	Dominant interspecies interaction . . . . .	120
5.3.2	Commensurate total filling . . . . .	121
5.3.3	The trapping potential . . . . .	125

---

<b>6 Degenerate Bose-Bose mixture in a 3D optical lattice</b>	<b>127</b>
6.1 A double condensate . . . . .	128
6.2 A 3D optical lattice . . . . .	131
6.2.1 The lattice laser . . . . .	131
6.2.2 Experimental setup . . . . .	132
6.2.3 Lattice calibration . . . . .	134
6.2.4 Loading of $^{87}\text{Rb}$ in the lattice . . . . .	141
6.3 Experimental results . . . . .	142
6.3.1 The superfluid to Mott insulator transition in $^{87}\text{Rb}$ . . .	143
6.3.2 Adding the second species . . . . .	146
6.4 Theoretical scenarios . . . . .	152
6.4.1 The issue of finite temperature . . . . .	152
6.4.2 Effective potentials . . . . .	156
6.4.3 Polarons . . . . .	158
<b>7 The quest for Feshbach resonances</b>	<b>163</b>
7.1 Experimental procedure . . . . .	164
7.2 Preliminary results . . . . .	166
<b>Conclusions</b>	<b>171</b>
<b>Bibliography</b>	<b>173</b>
<b>Index</b>	<b>183</b>



# Introduction

What allowed quantum physics to quit the small world of pure research and to penetrate deeply the daily life of billion of people across the world is its effectiveness at explaining the observed natural phenomena and at guiding the development of new devices based on the results of these explanations.

Among the most peculiar phenomena are without doubt superfluidity and superconductivity. These two phenomena brought the quantum world to a mesoscopic scale and promise to enter our daily life in a future which looks not too far. Bose-Einstein condensation in dilute atomic gases is another example of system for which quantum phenomena are observable at mesoscopic scale [1]. Not surprisingly, this perspective drew the attention of a larger community than that of atomic physics and now many people started experiments aimed at the realization of a “universal” quantum simulator in which models once peculiar of solid state physics are realized with atomic Bose-Einstein condensates [2, 3, 4].

One of the key ingredient of this simulators are optical lattices: periodic potentials generated by a laser standing wave in which atoms can be trapped and their properties changed with unprecedented accuracy including the ability to prepare systems of reduced dimensionality [5]. Among the many important results one needs to cite at least the observation of the superfluid to Mott insulator transition in 3D [6] and in reduced dimensions [7], the observation of a Tonks-Girardeau gas [8] and of the Berezinskii-Kosterlitz-Thouless transition to quasi-long range order in two dimensions [9].

This scenario is even richer if two distinguishable condensates are present in the system: this was recognized as early as ten years ago when the first mixture of condensates was produced [10]. In this work for the first time two different hyperfine states of  $^{87}\text{Rb}$  were brought to Bose-Einstein condensation by directly cooling one of the two and letting the temperature of the two gases equilibrate. This technique of sympathetic cooling, as

## 8 Introduction

---

predicted by the authors of [10], became the workhorse for the cooling of fermionic species<sup>1</sup>:  ${}^6\text{Li}$  with  ${}^7\text{Li}$  [12],  ${}^{23}\text{Na}$  [13] and  ${}^{87}\text{Rb}$  [14] and  ${}^{40}\text{K}$  with  ${}^{87}\text{Rb}$  [15]. Furthermore the same technique allowed to reach the degenerate regime for  ${}^{41}\text{K}$  whose direct cooling was problematic [16].

An extensive literature exists for Fermi-Bose mixture for which –among others– interspecies Feshbach resonances [17, 18, 19] and boson-induced collapse of the Fermi gas [20, 21] have already been observed. On the other hand, concerning Bose-Bose mixtures, soon after the realization of a condensate of  ${}^{41}\text{K}$  by sympathetic cooling with  ${}^{87}\text{Rb}$  the first mixture of two different superfluid was realized at LENS [22], but no experimental efforts followed this seminal work. This fact, together with the intriguing possibility of exploiting Feshbach resonances to control the interspecies interactions, motivated us in starting a new experiment devoted to the study of a mixture of two degenerate bosonic species in an optical lattice.

Feshbach resonances can be used to convert pairs of atoms into molecules as it was demonstrated starting both from a Fermi gas [23, 24] and from a Bose-Einstein condensate [25, 26, 27]. While in the fermionic case the molecules are relatively stable and a Bose-Einstein condensate of these molecules could be observed [28, 29], in the Bose-Bose case Feshbach molecules are highly unstable under molecule-molecule and atom-molecule collisions due to their high vibrational energy. The observation of a long living sample of such molecules has been possible only in an optical lattice with a occupation of one molecule per site [30]. In view of the creation of heteronuclear bosonic molecules, Bose-Bose mixtures of two different species in a 3D optical lattice are therefore the most promising candidates, given the complexity of experiments with two different fermionic species [31, 32, 33]. Once molecules are produced they can in principle be stabilized by transferring them to their vibrational ground state: at this stage the lattice is no longer necessary and a totally unexplored quantum phase of dipolar molecules can be created [34].

Several open questions lie between us and this fascinating perspective: an answer to the first, most basic, but by no means trivial of these is offered by this thesis. The thesis is divided in three parts which reflect the chronological development of my work. The first part, after a short theoretical introduction to the topics underlying the physics that we want to explore (chapter 1), presents a description of the experimental apparatus

---

<sup>1</sup>The first degenerate Fermi gas was however produced with a different technique [11].

for cooling  $^{87}\text{Rb}$  and  $^{39}\text{K}$  or  $^{41}\text{K}$  (chapter 2). This apparatus has been build almost entirely during my PhD and features several novel improvements including a new kind of magnetic trap. In the second part, after introducing the physics of cold atomic collisions in chapter 3, I will present the results on a collisional measurement on  $^{39}\text{K}$  which explored the possibility of using this isotope as the second condensate of our mixture (chapter 4): considering the outcome of these measurements we decided to shift to  $^{41}\text{K}$ . We indeed were able to repeat the simultaneous condensation of  $^{87}\text{Rb}$  and  $^{41}\text{K}$  and to load for the first time a mixture of two condensates in an optical lattice. These results are described in the third and last part. After presenting a short theoretical introduction to quantum phases of atoms in optical lattices (chapter 5), I will detail the most important result of this first study of two condensates in a 3D optical lattice: the effect of the presence of a condensate of  $^{41}\text{K}$  on the superfluid to Mott insulator transition in  $^{87}\text{Rb}$ . These results are presented in chapter 6. Finally preliminar results concerning heteronuclear Feshbach resonances on the  $^{87}\text{Rb}$ - $^{41}\text{K}$  mixtures are presented in chapter 7.



## **Part I**

# **A way to a Bose-Bose mixture**



# Chapter 1

## Theoretical framework

Never underestimate the joy people derive from hearing something they already know.

(Enrico Fermi)

In this chapter I will very quickly review on the theoretical side concepts that are at the foundation of the experimental work presented in this thesis. The material is presented mainly with the purpose of establishing a notation that can be consistently used in the following: more advanced and specific topics are presented closed to the place where the experiment is described. As a consequence a reader already familiar with laser cooling and trapping and Bose-Einstein condensation in harmonic potentials might probably entirely skip the chapter. An exception is probably given by § 1.3 where the theory of two interacting condensates in a harmonic trap is presented. On the other hand a reader that is completely unfamiliar with these topics will hopefully find a good introduction of the physics issue and certainly good references to improve his knowledge.

### 1.1 How lasers can cool (and trap) atoms

#### 1.1.1 Laser cooling

Consider an atom at rest with an isolated level with energy  $h\nu_0$  and lifetime  $\Gamma^{-1}$ . The mechanical action of a laser light of frequency  $\nu$  on this atom can

## 14 Theoretical framework

---

be expressed as a force given by <sup>1</sup> [35]:

$$\mathbf{F}(\mathbf{r}) = -\hbar \left( \boldsymbol{\alpha}(\mathbf{r}) \Delta + \boldsymbol{\beta}(\mathbf{r}) \frac{\Gamma}{2} \right) \frac{S(\mathbf{r})}{1 + S(\mathbf{r})}, \quad (1.1)$$

where  $\Delta = 2\pi(\nu - \nu_0)$  is the detuning,  $S$  is the saturation parameter which depends on the Rabi frequency  $\Omega$  as

$$S(\mathbf{r}) = \frac{\Omega^2(\mathbf{r})/2}{\Delta^2 + \Gamma^2/4} \quad (1.2)$$

and the two vectors  $\boldsymbol{\alpha}$  and  $\boldsymbol{\beta}$  are given by:

$$\begin{aligned} \boldsymbol{\alpha} &= \nabla\Omega(\mathbf{r})/\Omega \\ \boldsymbol{\beta} &= \nabla\phi(\mathbf{r}) \end{aligned} \quad (1.3)$$

where  $\phi(\mathbf{r})$  is here the phase profile of the laser electric field. The force originated by  $\boldsymbol{\alpha}$  is the so called *dipole force* which is conservative, while the other contribution is the *radiation pressure* which is given by the interplay between the absorption and the spontaneous emission. If the atom is in motion with velocity  $v \ll c$  the above formulas remain valid with the change  $\delta \rightarrow \delta - \mathbf{k} \cdot \mathbf{v}$  which takes into account the Doppler shift.

If the atom interacts with two counterpropagating red-detuned laser beams, in the limit of weak saturation, the force acting on the atom has a linear dependence from the velocity along the direction of the beams and acts as a viscous force. This scheme, repeated with six laser beams along three orthogonal directions, can be used to cool the atom and it is called *optical molasses*. The viscous force arises because absorption is more probable from the beam which the atom is moving against because in this case Doppler shift compensates the detuning. The effect of absorption, which removes a momentum  $\hbar k$  from the atoms is counter-balanced by the spontaneous emission which reintroduces this momentum in a random direction at a rate  $\Gamma$ . The minimum temperature corresponding to the equilibrium between the two processes is given by

$$k_B T_D = \frac{\hbar\Gamma}{2} \quad (1.4)$$

and it is called *Doppler temperature*.

For a two level atom the Doppler temperature is the lower limit of laser cooling techniques. A more efficient cooling mechanism arises if the two levels are manifold corresponding to non-zero total angular momentum  $F$  and  $F + 1$ <sup>2</sup>. In this case in fact the degeneracy of the magnetic sublevels is

---

<sup>1</sup>The atomic transition is assumed to satisfy the following condition:  $m\Gamma \gg \hbar k_0^2$ , where  $k_0 = 2\pi\nu_0/c$ .

<sup>2</sup>Could be also  $F - 1$  but it is much less common [36].

lifted by the interaction with the polarization of the laser. If this polarization is constant and  $\sigma^\pm$ , the resulting effect will be the well known Zeeman optical pumping toward the  $|F, \pm F\rangle$  ground state. If the polarization is not constant as it is the case if the two counterpropagating beams have orthogonal linear polarization or opposite circular polarization, the different magnetic components of the ground state manifold couple differently with the laser light. This coupling can be represented as a spatially dependent effective potential. Under certain condition, the dynamics of the atom is such that it displaces climbing up the potential hill until a cycle of absorption and spontaneous emission occurs which transfers the atom to a state with lower potential energy. During this process the atom loses kinetic energy and it is therefore cooled: since the cooling process occurs as the atom always climbs up a potential hill before being re-transferred at the bottom of the hill this process is named *Sisyphus cooling*. The lowest temperature that can be achieved with this technique depends on the angular momentum of the level involved but it is on the order of

$$k_B T_S \simeq \frac{\hbar \Omega^2}{\Delta}. \quad (1.5)$$

The above formula is valid if the resulting temperature is still well above the recoil temperature  $T_{\text{rec}}$  defined as the temperature corresponding to the kinetic energy gained by the atom after a recoil with momentum  $\hbar k$ :

$$E_{\text{rec}} = k_B T_{\text{rec}} = \frac{\hbar^2 k^2}{2m} = \frac{h^2}{2m\lambda^2}. \quad (1.6)$$

This temperature is therefore the ultimate limit which cannot be overcome using laser light. A further cooling mechanism, decisive for the reach Bose-Einstein condensation is presented in § 2.4 and make use of radio-frequency photons whose recoil energy is negligible.

### 1.1.2 <sup>87</sup>Rb and K: level scheme

The results presented in § 1.1.1 are derived for a two level atom. The hyperfine structure of the levels involved in the  $D2$  line of <sup>87</sup>Rb is shown in figure 1.1. The  $|^2S_{1/2}, F = 2\rangle \rightarrow |^2P_{3/2}, F = 3\rangle$  transition is closed and well isolated from any other transition. The theoretical results of § 1.1.1 can be reproduced quantitatively in the experiment and this is the transition of choice for laser cooling. However, a laser red detuned from this transition is brought closer to the resonance with the  $|^2S_{1/2}, F = 2\rangle \rightarrow |^2P_{3/2}, F =$

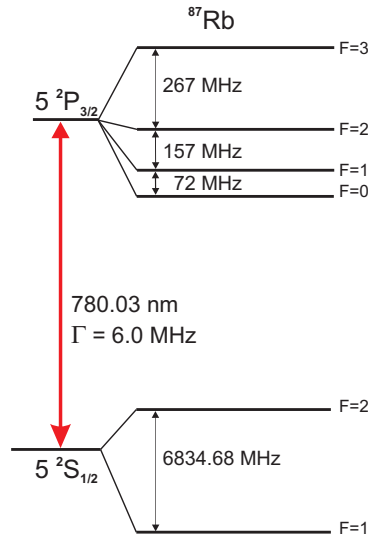


**Figure 1.1.** Scheme of the hyperfine structure of the D2 line of  $^{87}\text{Rb}$ .

2) and some optical pumping toward the  $|^2S_{1/2}, F = 1\rangle$  state cannot be avoided. To counter this effect a second laser, called *repumper* is tuned close to the  $|^2S_{1/2}, F = 1\rangle \rightarrow |^2P_{3/2}, F = 2\rangle$  transition: this effectively closes the transition and laser cooling can occur without losses. Furthermore Sisyphus cooling can be realized and temperature lower than  $T_D \simeq 140 \mu\text{K}$  can be obtained.

The situation is completely different for the two bosonic isotopes of potassium,  $^{39}\text{K}$  and  $^{41}\text{K}$ , whose D2 lines level scheme is shown in figure 1.2. In these two species in fact the hyperfine structure of the excited level is so small compared to the natural linewidth, that it is not possible to simply think in terms of two isolated levels even in presence of an auxiliary repumping beam. Opposite, the dynamics of the internal degrees of freedom of the atoms involves all the hyperfine components of the P state and therefore the force is due to both the lasers from the  $|S, F = 1\rangle$  and  $|S, F = 2\rangle$  states.

A careful balance of the two intensities and detuning is required to reach the Doppler temperature [37] and even sub-Doppler cooling can be realized although in a regime of intensity and detuning unsuitable for loading a high number of atoms in a trap. These results agree with a model based on the integration of the optical Bloch equations for all the levels involved in the transition [38, 37]. The absence of an easy mechanism for reaching sub-Doppler is one of the obstacles toward the direct realization of a Bose-

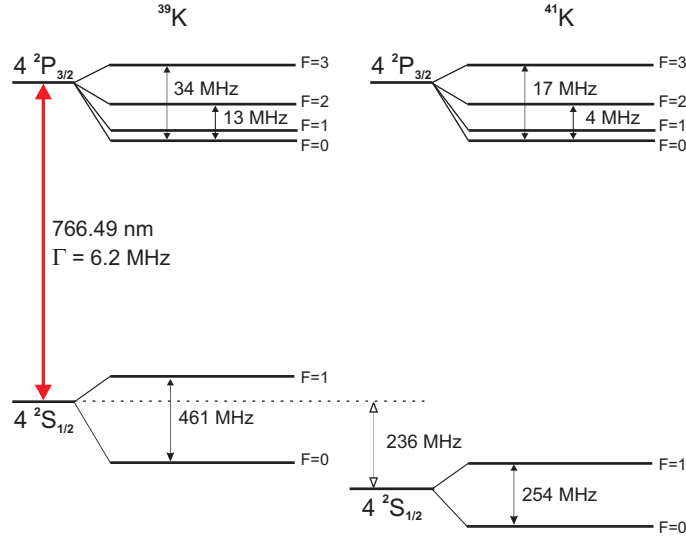


**Figure 1.2.** Scheme of the hyperfine structure of the D2 line of  $^{39}\text{K}$   $^{41}\text{K}$ . The relative abundances are about 93% and 7% respectively.

Einstein condensate of  $^{39}\text{K}$  and  $^{41}\text{K}$ : we will come back on this point when discussing the experimental setup for the laser cooling of K in chapter 2.

### 1.1.3 Dipole traps and optical lattices

As it was shown in § 1.1.1, beside the “classical” effect of the radiation pressure, laser light interacts also with the internal degrees of freedom of the atoms through the so called *dipole force*. It can be shown that, in the special case of alkali atoms in their ground state  $|F, m_F\rangle$  this dipole potential is related to the laser parameters by [39]:

$$U_{dip}(\mathbf{r}) = \frac{\pi c^2 \Gamma}{2\omega_0^3} \left( \frac{2 + P_\epsilon g_F m_F}{\Delta_{2,F}} + \frac{1 - P_\epsilon g_F m_F}{\Delta_{1,F}} \right) I(\mathbf{r}) = U_0 I(\mathbf{r}), \quad (1.7)$$

where  $\Delta_{2,F}$  ( $\Delta_{1,F}$ ) is the detuning from the D2 (D1) line,  $g_F$  is the Landé  $g$ -factor,  $I$  is the intensity of the laser and  $P_\epsilon$  takes into account the polarization state of the light as seen by the atom (0 for linear and  $\pm 1$  for  $\sigma^\pm$  polarization respectively). This potential can be repulsive or attractive depending on the sign of the expression in parentheses, but the shape of the potential depends only on the intensity profile of the laser light.

In this work we make extensive use of two particular configurations known as crossed dipole trap and optical lattice that will be analyzed in some detail in the following. One should remark however, that these kind

of potential are by no means the only structure that can be realized to trap atoms with light (see for instance [39]).

### Crossed dipole trap

In this configuration the trapping is provided by two orthogonal beams that intersect at their beam waist. A single Gaussian beam in the so-called TEM<sub>00</sub> mode generates a potential given by:

$$U(\rho, z) = U_0 I_0 \frac{\exp(-2\rho^2/w(z)^2)}{1 + (z/z_R)^2}, \quad (1.8)$$

where  $z$  is the direction of propagation of the laser beam,  $\rho$  is the radial distance from the center of the beam,  $I_0$  the peak laser intensity,  $w(z) = w_0(1 + (z/z_R)^2)^{1/2}$  is the width of the beam and  $z_R = \pi w_0^2/\lambda$  is the so called *Rayleigh range*.

If  $\lambda > \lambda_0$  (red detuning) the atoms will be trapped in the maximum of the intensity, around ( $\rho = 0, z = 0$ ). Furthermore, if the size of the atomic cloud is much smaller than  $w_0$  in the radial plane and  $z_R$  along the axial direction one can expand the potential around the potential minimum:

$$U(\rho, z) = \frac{1}{2} m(\omega_{\parallel}^2 z^2 + \omega_{\perp}^2 \rho^2), \quad (1.9)$$

where we have neglected a constant term and set:

$$\begin{aligned} \omega_{\parallel}^2 &= \frac{2|U_0| I_0 \lambda^2}{\pi^2 w_0^4} \\ \omega_{\perp}^2 &= \frac{4|U_0| I_0}{w_0^2}. \end{aligned} \quad (1.10)$$

As one could expect, the confinement is much bigger in the radial plane where the intensity gradient is substantial. As we shall see in the following, a very useful parameter characterizing a harmonic trap is the so called *aspect ratio* defined as  $\mathcal{A}_R = \omega_{\perp}/\omega_z$ : when it is bigger than 1 the trapped cloud is cigar shaped<sup>3</sup>.

It is clear that with a single beam it is very hard to obtain a spherical trap, a feature which is often desirable in the experiments. This problem

---

<sup>3</sup>There is considerably less consensus on how to define the shape corresponding to the opposite limit  $\mathcal{A}_R \ll 1$ : the unavoidable American bias of international literature has collected some consensus speaking of pancake shaped condensates. This has the obvious disadvantage of being totally neutral for those who have never see a pancake. I humbly propose to adopt the denomination of pizza shaped condensates.

can be overcome by adding a second laser beam perpendicular to the previous one. If the frequency or the polarization of the two beams is sufficiently different to neglect the interference between the two, the resulting potential is barely the sum of two potentials like that of Eq. (1.9). If for instance we take the two orthogonal beams along the  $x$  and  $y$  directions the resulting potential is still harmonic but the frequencies are given by:

$$\begin{aligned}\omega_z^2 &= \omega_{\perp,x}^2 + \omega_{\perp,y}^2 \\ \omega_y^2 &= \omega_{\perp,x}^2 + \omega_{\parallel,y}^2 \\ \omega_x^2 &= \omega_{\perp,y}^2 + \omega_{\parallel,x}^2\end{aligned}\tag{1.11}$$

In the following we will almost always neglect  $\omega_{\parallel}$  with respect to  $\omega_{\perp}$ : the resulting trapping potential acquires cylindrical symmetry on the plane of the two beams and the aspect ratio is given by  $\sqrt{2}/2$ .

Before moving to the optical lattice configuration we will discuss briefly two important issues of the optical trapping of neutral atoms: the heating rate and the trap depth.

As it was clearly stated in the previous section the spontaneous emission can be small but cannot be eliminated. It can be shown (see for example [39]) that the heating rate induced by spontaneous emission for a red detuned trap is:

$$\dot{E} \simeq \frac{\Gamma}{\hbar} \frac{U_0 I}{\Delta^2} E_{\text{rec}}.\tag{1.12}$$

By comparing Eq. (1.7) with Eq. (1.12) one can see a peculiar feature of dipole traps: the potential height depends on the ratio  $I_0/\Delta$ , while the heating rate depends on  $I_0/\Delta^2$ . Since, neglecting technical noise, the heating rate is the only factor that limits the lifetime of the atoms, a trap at both high intensity and large detuning can be considered conservative: in practice an atom is kicked out of a trap by other mechanisms before any event of spontaneous emission occurs.

As one can clearly see from Eq. (1.8), the trap depth is simply given by  $V_0 = U_0 I_0$  but this is strictly true only if the dipole force is the only force acting on the atoms. In practice the experiments are always performed in presence of the gravity<sup>4</sup> which adds a potential gradient such that the total potential is given by:

$$V(x) = V_0 \exp(-2x^2/w^2) - mgx,\tag{1.13}$$

<sup>4</sup>This statement is not fully correct as there is a growing interest for experiment in microgravity in which atoms in free fall can be interrogated for long time. See for example [40].

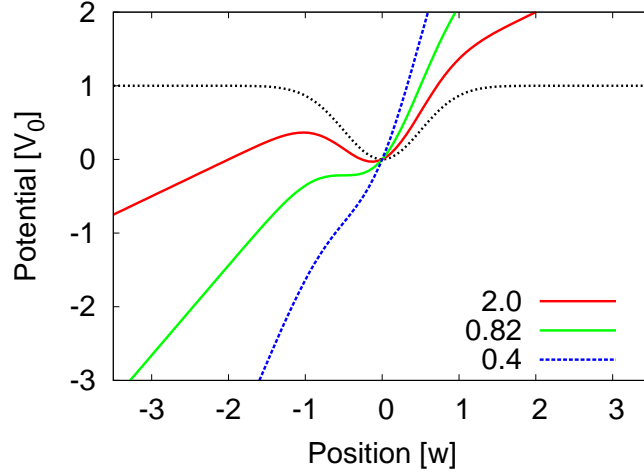


**Figure 1.3.** Total trapping potential in the presence of gravity for different indicated values of the ratio  $V_0/(mgw)$ . Dotted line is the potential shape for  $g = 0$ .

where, for the sake of simplicity, we restricted to 1D. From this expression we see that the curvature of the potential on the bottom is not changed while the position of the minimum is shifted; however the strongest effect is on the trap depth as it is clearly shown in Fig. 1.3. It is easy to derive from Eq. (1.13) a condition for having a nonzero trap depth:

$$\frac{V_0}{mgw} > \sqrt{e}/2 \sim 0.82$$

This effect is even more relevant for the case of a single beam trap because the dependence of  $w$  on  $z$  shortens the effective size of the trap along the axial direction.

Further detail on our implementation of a crossed dipole trap can be found in chapter 7.

### Optical lattices

If the two beams generating the optical trap are allowed to interfere and form an angle  $\theta$  with the  $z$  direction, it is straightforward to see that the intensity profile exhibit interference along the  $z$  direction. Setting an equal intensity  $I_0$  for each of the two beams one has:

$$I(\mathbf{r}) = 4I_0 \frac{\exp(-2\rho^2/w(z)^2)}{1 + (z/z_R)^2} \cos^2(\pi z/d).$$

As we can clearly see, this intensity profile will give rise to a trapping potential similar to that one of Eq. (1.8) but with the important feature of a

periodic modulation with a periodicity given by

$$d = \lambda / (2 \cos \theta).$$

In the experiments reported in this work the geometry of the beams is always counter-propagating ( $\theta = \pi$ ) and therefore the period of the lattice is given by:

$$d = \lambda / 2. \tag{1.14}$$

Expanding this expression around the center of the trap ( $\rho \ll w_0, z \ll z_R$ ) we find the sum of a periodic potential and a harmonic confinement:

$$V(\mathbf{r}) = \frac{1}{2} m \omega_L^2 \rho^2 + V_L \cos^2(\pi z / d), \tag{1.15}$$

where

$$V_L = 4|U_0|I_0 = s E_{\text{rec}} \tag{1.16}$$

$$\omega_L^2 = \frac{8|U_0|I_0}{m w_0^2} = \frac{4V_L}{m w_0^2} \tag{1D} \tag{1.17}$$

where we have defined the parameter  $s$  that will be extensively used in the following to characterize the height of the lattice.

If we now repeat this reasoning along the other spatial directions, it is easy to see that an arrangement with three pairs of counter-propagating beams can realize a cubic 3D optical lattice if interference along different directions is adequately suppressed. The periodic part is given by each beam separately, while the harmonic confinement is increased with respect to the 1D case because each direction has a contribution from two beams (see Eq. (1.11)) and therefore

$$\omega_L^2 = \frac{8V_L}{m w_0^2} \tag{3D}. \tag{1.18}$$

The residual harmonic confinement introduced by this realization of the periodic potential increases with increasing lattice height and will play an important role in the physics of the Mott insulator as we shall see in § 6.4.1.

## 1.2 Bose-Einstein condensation in harmonically trapped gases

The problem of the equation of state of an ideal and uniform gas of particles obeying the Bose statistics was solved long time ago by Einstein and owed

him to add his name to the statistics of particle with integer spin [41]. Here I shall briefly review some fundamental results about a Bose gases confined in a harmonic trap which is the case of main interest from the experimental point of view. The reader interested in this topic will find both a clear compendium of the subject and a nice starting point for further study in reference [42].

### 1.2.1 Ideal gas

A gas of  $N$  non interacting particles can be described as a collection of  $3N$  single-particle, one-dimensional Hamiltonians:

$$h_{i,\alpha}(r, p) = \frac{p_{i,\alpha}^2}{2m} + \frac{1}{2}m\omega_\alpha^2 r_{i,\alpha}^2 \quad \begin{cases} i = 1 \dots N \\ \alpha = x, y, z. \end{cases}$$

From this we have immediately the eigenvalues of the system

$$E_{\{n_{i,\alpha}\}} = \sum_{i,\alpha} \hbar\omega_\alpha(n_{i,\alpha} + 1/2)$$

and we can already draw an important (although not surprising) conclusion: at  $T = 0$  the ground state of the system is given by the non degenerate multiset  $\{n_{i,\alpha}\} = 0 \forall i, \alpha$ . This means that the wavefunction of the *total* system is given by:

$$\psi(\mathbf{r}) = \sqrt{N} (\pi)^{-3/4} \bar{a}_{ho}^{-3} \prod_{\alpha} \exp(-r_\alpha^2/a_{ho}^{(\alpha)}) \quad (1.19)$$

where we have introduced the geometric average of trap frequencies  $\bar{\omega}$  and the harmonic oscillator length  $a_{ho}$  given by

$$\bar{\omega} = (\omega_x \omega_y \omega_z)^{1/3} \quad (1.20)$$

$$a_{ho}^{(\alpha)} = (m\omega_\alpha/\hbar)^{-1/2}. \quad (1.21)$$

At finite temperature one needs to take into account the occupation of the excited states. If  $k_B T \gg \hbar\bar{\omega}$  the number of multiset  $\{n_{i,\alpha}\}$  with a energy around  $k_B T$  becomes very big and it is correct to make a semiclassical approximation using a continuous density of state [43]

$$g(E) = \frac{E^2}{2(\hbar\bar{\omega})^3},$$

obtained taking the zero of the energy at the ground state. With this approximation, it is straightforward to evaluate the total population in the

excited states:

$$N - N_0 = \int_0^\infty \frac{g(E)dE}{e^{\beta(E-\mu)} - 1} = \left( \frac{k_B T}{\hbar \bar{\omega}} \right)^3 g_3(z) \quad (1.22)$$

where  $\beta = (k_B T)^{-1}$ ,  $\mu$  is the chemical potential,  $z = \exp(\beta\mu)$  is the fugacity and  $g_3(z) = \sum_n z^n/n^3$  is a polylogarithm ( $g_3(1) = \zeta(3) \simeq 1.20$ , the Riemann zeta function). The important point is that, as long as  $\mu < 0$ ,  $0 < g_3(z) < \zeta(3)$ . This means that, for any given temperature, the population in the excited states has a maximum value: if the number of atoms exceeds this value (or equivalently, if the density increases so that  $\mu$  becomes positive) this excess of atoms will accommodate in the ground state building up the Bose-Einstein condensate.

From the experimental point of view the transition is not crossed increasing the density, but decreasing the temperature: for a given  $N$  the condensate starts to accumulate at a temperature  $T_C$  such that  $N = \max_\mu(N - N_0)$ . Inserting this condition in Eq. (1.22) one obtains

$$k_B T_c = \hbar \bar{\omega} (N/\zeta(3))^{1/3} \simeq 0.94 \hbar \bar{\omega} N^{1/3}. \quad (1.23)$$

The typical order of magnitude of  $T_C$  for the experiments reported in this work ( $N \sim 10^5$ ,  $\bar{\omega} \sim 2\pi \times 100$  Hz) is 200 nK. In this regime the semiclassical approximation is still very well verified and finite size effect (see [42]) play only a minor role.

We will not enter the detail of the ideal gas thermodynamics since –as we will see in the next section– interactions play a crucial role. Again we shall point to reference [42] for further information.

### 1.2.2 Interacting gas

As we have shown in the previous section, Bose-Einstein condensation is a pure consequence of the statistics of the particles and therefore do not require interactions. Rather, one could expect that the presence of interactions would put extra energy in the system and therefore increase the number of particles that are allowed to be in an excited state at a given temperature. This would lead to a reduction in the critical temperature either eliminating the phenomenon of condensation or making it impossible to see at the lowest temperature available in the lab. It turns out that, although qualitatively the mechanism outlined above plays a role, Bose-Einstein condensation is possible even in the presence of interactions

among the particles which in our case are due to binary atomic collisions [44, 45].

The topic of ultracold collisions between atoms is a subtle one and we will give a short introduction to it in chapter 3. For the present analysis we shall only remind that, for sufficiently low energy, the cross section for elastic scattering does not depend on the energy of the two colliding partners and therefore decouples from the kinetic part of the Hamiltonian. Furthermore, if the interparticle separation is much bigger than the range of the potential (i.e. at low density), it is reasonable to approximate the interaction by a two body hard sphere collision:

$$V_{int}(\mathbf{r}, \mathbf{r}') = g\delta(\mathbf{r} - \mathbf{r}'). \quad (1.24)$$

In chapter 3 we will see that the coupling constant  $g$  is related to the  $s$ -wave scattering length  $a$  by

$$g = \frac{4\pi\hbar^2}{m} a, \quad (1.25)$$

for the present analysis we only remind that if  $a > 0$  ( $a < 0$ ) the interaction is repulsive (attractive).

### **The Gross-Pitaevskii equation**

Within the approximation (1.24) it is possible to express the Hamiltonian in second quantization as:

$$\mathcal{H} = \hat{\Psi}^\dagger(\mathbf{r}, t)L(\mathbf{r})\hat{\Psi}(\mathbf{r}, t) + \frac{g}{2}\hat{\Psi}^\dagger(\mathbf{r}, t)\hat{\Psi}^\dagger(\mathbf{r}, t)\hat{\Psi}(\mathbf{r}, t)\hat{\Psi}(\mathbf{r}, t), \quad (1.26)$$

where we have defined the single particle Hamiltonian as

$$L(\mathbf{r}) = -\frac{\hbar^2}{2m}\nabla^2 + V_{ext}(\mathbf{r}) \quad (1.27)$$

At zero temperature it is easy to carry out a mean field expansion  $\hat{\Psi}(\mathbf{r}, t) = \Phi(\mathbf{r}, t) + \delta\hat{\psi}(\mathbf{r}, t)$  which leads to the very well known Gross-Pitaevskii equation, both in its time dependent

$$i\hbar\frac{\partial}{\partial t}\Phi(\mathbf{r}, t) = \left(L(\mathbf{r}) + g|\Phi(\mathbf{r}, t)|^2\right)\Phi(\mathbf{r}, t) \quad (1.28)$$

and time-independent form

$$\left(L(\mathbf{r}) + g\phi^2(\mathbf{r})\right)\phi(\mathbf{r}) = \mu\phi(\mathbf{r}). \quad (1.29)$$

The latter is obtained by setting  $\Phi(\mathbf{r}, t) = \phi(\mathbf{r})\exp(-i\mu t/\hbar)$  with  $\mu$  chemical potential and  $\phi(\mathbf{r})$  a real function [42].

### Thomas-Fermi approximation

Much of the intriguing physics of the condensates is generated by the non-linearity present in the Gross-Pitaevskii equation which is due to the interactions among the particles. It is therefore not surprising that the ground state of the system is deeply influenced by the sign of the coupling  $g$ . For *repulsive* interaction ( $g > 0$ ) the nonlinear term contributes to the stability of the system because it dominates on the kinetic term. If we call  $\ell$  the size of the system it is easy to see that:

$$\begin{aligned} E_{kin} &\sim (h^2/m)\ell^{-2} \\ E_{int} &\sim gN\ell^{-3} \end{aligned}$$

and therefore, using Eq. (1.25),

$$\frac{E_{kin}}{E_{int}} \sim \frac{\ell h^2}{gNm} \sim \frac{\ell}{Na}.$$

In the limit of an infinite system ( $N \rightarrow \infty$ ,  $\ell \rightarrow \infty$ , but  $N\ell^{-3} \rightarrow \bar{n}$  finite) the kinetic term becomes completely negligible and Eq. (1.29) is immediately solved:

$$n_0(\mathbf{r}) = \phi^2(\mathbf{r}) = \max \left\{ g^{-1}(\mu - V_{\text{ext}}(\mathbf{r})), 0 \right\}. \quad (1.30)$$

This is the so-called Thomas-Fermi regime. For a harmonically trapped gas the Thomas-Fermi profile is an inverted parabola and it represents a good approximation of the actual density profile if

$$Na \gg a_{ho}, \quad (1.31)$$

which is obtained from the above analysis with the obvious change  $\ell \rightarrow a_{ho}$ . In the experiments presented in this work  $a$  is in the range of a few nanometers while  $a_{ho}$  is on the order of  $3 \mu\text{m}$ : this means that the approximation is reasonable for  $N > 10^4$ . Remembering that  $\int d\mathbf{r} n_0(\mathbf{r}) = N$  it is easy to obtain an expression for the chemical potential from Eq. (1.30)

$$\mu_{TF} = \frac{1}{2} \hbar \bar{\omega} \left( 15 \frac{Na}{a_{ho}} \right)^{2/5}. \quad (1.32)$$

### Attractive condensates: instability

If the interaction is repulsive the spectrum of the Gross-Pitaevskii equation becomes unbounded from the lower side: the energy of the system can be always minimized increasing the density. This situation corresponds to the

collapse of the atomic cloud and poses severe limitations to the realization of an attractive condensate. Actually only the presence of the harmonic potential which establishes a zero-point kinetic energy allows the system to equilibrate: by the same argument given in the above section one can expect that the condensate is stable as long as the condition Eq. (1.31) for the absolute value of  $a$  is *not* satisfied. We therefore expect collapse for atoms in the range

$$N_{\text{cr}} \sim \frac{a_{ho}}{|a|} \sim 10^3. \quad (1.33)$$

I will not review all the results for the dynamics of this mean field collapse [46]. Still the topic is of some importance because the interaction among  $^{39}\text{K}$  atoms is attractive and therefore it is impossible to obtain a stable condensate of this species with more than a few  $10^3$  atoms without using some control of the interaction. We will come back to this point in part II.

### Excitation of the condensate

The excitation of the condensate is contained in the fluctuations around the mean field solution that we indicated with  $\delta\hat{\psi}(\mathbf{r}, t)$ . These fluctuations exist at zero temperature (*quantum depletion*) and grow further at finite temperature. Eventually, as the temperature increases these fluctuations become more and more important and the mean field approximation is no longer meaningful.

The spectrum of excitation of a condensate can be calculated using the Bogolioubov approximation which amounts to expand the Hamiltonian up to second order in the fluctuations and diagonalize the quadratic part so that:

$$H = E_0 + \sum_n \hbar\omega_n \hat{b}_n^\dagger \hat{b}_n.$$

The transformation to this basis is given by:

$$\delta\hat{\psi}(\mathbf{r}, t) = \sum_n (u_n(\mathbf{r})e^{-i\omega_n t} \hat{b}_n - v_n^*(\mathbf{r})e^{i\omega_n t} \hat{b}_n^\dagger) \quad (1.34)$$

where the  $b$  operators obey Bose-Einstein commutation rules and the two sets of function  $\{u_n\}$  and  $\{v_n\}$  satisfy the following Bogolioubov-De Gennes equations [45]:

$$\begin{cases} L(\mathbf{r})u_n(\mathbf{r}) + g\phi^2(\mathbf{r})(2u_n(\mathbf{r}) + v_n(\mathbf{r})) & = (\mu + \hbar\omega_n)u_n(\mathbf{r}) \\ L(\mathbf{r})v_n(\mathbf{r}) + g\phi^2(\mathbf{r})(2v_n(\mathbf{r}) + u_n(\mathbf{r})) & = (\mu - \hbar\omega_n)v_n(\mathbf{r}) \end{cases} \quad (1.35)$$

The solution of Eq. (1.35) is not a trivial task and depends both on the trapping potential and on the condensate wavefunction. Nevertheless numerical and analytical solutions exist for several different external potentials. For a uniform condensate with density  $n_0$ , the Bogolioubov spectrum can be evaluated analytically in the Fourier space [45]:

$$\hbar\omega_q = \sqrt{\left(\frac{\hbar^2 q^2}{2m}\right)^2 + \frac{gn_0}{m}\hbar^2 q^2}. \quad (1.36)$$

In the case of a trapped condensate, the low-lying excitations are the center of mass dipole oscillations which occur at the trap frequencies and can be therefore used to measure them.

Once the solution to the Bogolioubov-De Gennes equation are known, it is possible to calculate the depletion of the condensate due to finite temperature by carrying out a simple thermodynamic average taking into account the occupation number of the bosonic quasiparticles:

$$\langle \hat{b}_n^\dagger \hat{b}_n \rangle = \left( e^{\beta \hbar \omega_n} - 1 \right)^{-1}.$$

### 1.3 Two coupled condensates: topology of the ground state

One of the main experimental results presented in this work is the realization of a mixture of two atomic Bose-Einstein condensates in a periodic potential. These results are described in detail in part III, here we present a theoretical introduction to the issue of the topology of the system in presence of an interaction between the two condensates.

In the same way as we did for the single species case, one can assume that the interaction between the two condensates is short range and therefore write a contact potential depending on a single parameter  $g_{12}$  as in Eq. (1.24). With this approximation it is easy to write a system of two coupled Gross-Pitaevskii equations:

$$\begin{cases} (L_1(\mathbf{r}) + g_1 \phi_1^2(\mathbf{r}) + g_{12} \phi_2^2(\mathbf{r})) \phi_1(\mathbf{r}) = \mu_1 \phi_1(\mathbf{r}) \\ (L_2(\mathbf{r}) + g_2 \phi_2^2(\mathbf{r}) + g_{12} \phi_1^2(\mathbf{r})) \phi_2(\mathbf{r}) = \mu_2 \phi_2(\mathbf{r}); \end{cases} \quad (1.37)$$

we will now look for the topology of the solutions of these two equations starting from the simple case of an homogeneous system and assuming that the two condensate are stable:  $g_1, g_2 > 0$ .

### Homogeneous system

The analysis of the realistic situation of an external harmonic confinement in the gravity field and for arbitrary interaction parameters can be found in [47] and we shall briefly review their conclusion later. Before the details however, one can have a good insight into the problem by considering the simpler case of a box potential without the presence of gravity but with repulsive interspecies interaction [48]. In this case, once the volume  $V$  of the box and the number of particle in each condensate  $N_1$  and  $N_2$  are fixed, the condensate densities are by definition  $n_i = \phi_i^2 = N_i/V$  uniform in the box and the coupled Gross-Pitaevskii equations simply give the chemical potential as:

$$\begin{cases} \mu_1 &= g_1 n_1 + g_{12} n_2 \\ \mu_2 &= g_2 n_2 + g_{12} n_1. \end{cases}$$

The energy of this uniform mixed state is easily evaluated from the full Hamiltonian of the system as

$$E_{\text{mix}} = \frac{1}{2V}(g_1 N_1^2 + g_2 N_2^2 + 2g_{12} N_1 N_2). \quad (1.38)$$

If we now consider a phase separated state in which each species occupies a volume  $V_i$  and neglect for the moment the energy associated to the interface, the energy is simply given by  $\sum_i g_i (N_i^2/V_i)$ . Applying the constraint  $V_1 + V_2 = V$ , it is easy to find that the energy of the system has a minimum

$$E_{\text{sep}} = \frac{1}{2V}(g_1 N_1^2 + g_2 N_2^2 + 2\sqrt{g_1 g_2} N_1 N_2) \quad (1.39)$$

corresponding to

$$V_1 = (1 + \sqrt{g_2/g_1}(N_2/N_1))^{-1} V \quad (1.40)$$

and

$$V_2 = V - V_1. \quad (1.41)$$

It is straightforward to see that:

$$\mu_i = g_i N_i / V_i. \quad (1.42)$$

This phase separated state is the one with lower energy if

$$E_{\text{sep}} - E_{\text{mix}} < 0 \Rightarrow \Delta g = g_{12} - \sqrt{g_2 g_1} > 0. \quad (1.43)$$

A more accurate treatment which allows fluctuations of the condensate densities from the uniform value shows that if the condition (1.43) is satisfied, the population of condensate 1 decays exponentially in the volume  $V_2$

with a characteristic length given by [48]:

$$\Lambda_1 = \left( \frac{\sqrt{g_1 g_2}}{\Delta g} \right)^{1/2} \xi_1,$$

where  $\xi_1$  is the so called healing length:

$$\xi_1 = \left( \frac{\hbar^2}{2m \mu_1} \right)^{1/2}. \quad (1.44)$$

Note that  $\Lambda \rightarrow \infty$  as  $\Delta g \rightarrow 0$  as we expect from (1.43). In turn this penetration into the opposite region modifies the density distribution of the majority condensate. In particular if  $\Lambda_1 \gg \sqrt{2} \xi_2$  (strong separation) the condensate 2 is depleted on a length scale given by  $\xi_2$ , while in the opposite limit (weak separation), condensate 2 follows the profile of condensate 1 and it is therefore depleted on a scale  $\Lambda_1$ . In particular, assuming that the interface occurs at  $z = 0$ , one can show that  $n_1(z) = (N_1/V_1)\rho_1(z)$ , where the function  $\rho_1(z)$  is given by [48]

$$\rho_1(z) = \begin{cases} 1 - \left( \frac{\sqrt{2}\xi_1}{\sqrt{2}\xi_1 + \Lambda_1} \right) \exp(-\sqrt{2} z/\xi_1) & \text{if } z > 0 \\ \frac{\Lambda_1}{\sqrt{2}\xi_1 + \Lambda_1} \exp(2z/\Lambda_1) & \text{if } z < 0 \end{cases} \quad (1.45)$$

in the strongly separated regime and by

$$\rho_1(z) = \begin{cases} 1 - \left( \frac{\xi_2}{\xi_1 + \xi_2} \right) \exp(-2 z/\Lambda_2) & \text{if } z > 0 \\ \frac{\xi_1}{\xi_1 + \xi_2} \exp(2z/\Lambda_1) & \text{if } z < 0 \end{cases}, \quad (1.46)$$

in the weakly separated regime. The corresponding functions for condensate 2 are obtained with the following changes:  $1 \rightarrow 2$ ,  $2 \rightarrow 1$  and  $z \rightarrow -z$ .

The two functions  $\rho(z)$  are plotted in figure 1.4 for both cases of strong and weak separation. As we can see in the strong separated case the total density (dashed green line) is depleted near the interface, while this does not happen in the regime of weak separation. In the case of the  $^{87}\text{Rb}$ - $^{41}\text{K}$  mixture, we have that the  $^{41}\text{K}$  condensate is the strong regime (decays with  $\xi$  before the interface), while the  $^{87}\text{Rb}$  condensate is in the weak one.

We note that the presence of the interface introduces an extra energy given by the surface tension: this can lead to a non-trivial topology of the two systems. Qualitatively, one can expect that the results of this simple model hold if the density modulation introduced by the external potential is small on the lengthscale of the interface. If this is not the case, in order to have a more quantitative prediction, one needs to include the harmonic confinement in the problem.

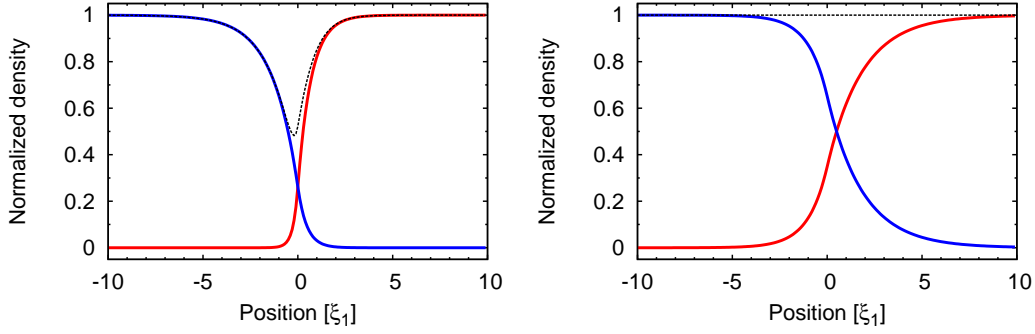


**Figure 1.4.** Plot of the density of two repulsively interacting condensates for strong (left) and weak (right) separation. The two solid lines indicate the density of each condensate while the dashed line marks the total density.

### Effects of the harmonic confinement

We will now consider the more general case of a harmonic confinement in the field of gravity, closely following the analysis of [47]. Under these assumptions, the single particle Hamiltonian becomes

$$L_i(\mathbf{r}) = -\frac{\hbar^2}{2m_i}\nabla^2 + \tilde{V}_{0,i} + \frac{m_i}{2}\sum_{\alpha}\omega_{\alpha,i}^2 r_{\alpha}^2 - m_i g z. \quad (1.47)$$

If the two masses are different (as it is the case with  $^{87}\text{Rb}$  and  $^{39,41}\text{K}$ ), the gravity displaces the center of the harmonic potential in a different way: this so-called *differential gravitational sag* has a big influence on the experimental results presented in part III. The displacement of each component is readily evaluated as

$$z_{0,i} = -g/\omega_{z,i}^2. \quad (1.48)$$

It is useful to shift the origin of the reference frame so that it coincides with one of the displaced position, say that of species 1. In this reference frame the displacement of species 2 is given by

$$z_0 = z_{0,2} - z_{0,1} = -g(\omega_{z,2}^{-2} - \omega_{z,1}^{-2}). \quad (1.49)$$

Furthermore, in the experiment the confining potential is determined by the coupling of the atoms with a static magnetic field (see section 2.3) or with the intensity of a laser radiation (see Eq. (1.7)) and therefore its shape is independent on the atomic species. As it is pointed out in [47] this allows one to perform a scaling on the spatial coordinates so that the trapping potential for *both* species is spherical:

$$r'_{\alpha} = (\bar{\omega}_1/\omega_{\alpha,1}) r_{\alpha} = (\bar{\omega}_2/\omega_{\alpha,2}) r_{\alpha} \quad (1.50)$$

With this transformation it is possible to rewrite Eq. (1.47) as

$$\begin{aligned} L_1(\mathbf{r}) &= -\frac{\hbar^2}{2m_1}\nabla^2 + V_{0,1} + \frac{1}{2}m_1\bar{\omega}_1^2(x'^2 + y'^2 + z'^2) \\ L_2(\mathbf{r}) &= -\frac{\hbar^2}{2m_2}\nabla^2 + V_{0,2} + \frac{1}{2}m_2\bar{\omega}_2^2(x'^2 + y'^2 + (z' - z_0)^2) \end{aligned} \quad (1.51)$$

where we have defined

$$V_{0,i} = \tilde{V}_{0,i} - \frac{m_i}{2} \left( \frac{g}{\omega_z} \right)^2.$$

If we now express all the lengths in units of  $\bar{a}_{ho,1}$  and all the energies in units of  $E_1 = \hbar\bar{\omega}_1$  we obtain the final expression

$$\begin{aligned} \tilde{L}_1(\mathbf{r}) - V_{0,1}/E_1 &= (1/2)(-\nabla^2 + x^2 + y^2 + z^2) \\ \tilde{L}_2(\mathbf{r}) - V_{0,2}/E_1 &= (1/2)(-\eta_m^{-1}\nabla^2 + \eta_E(x'^2 + y'^2 + (z' - z_0)^2)) \end{aligned} \quad (1.52)$$

where  $\eta_m = m_2/m_1$  and  $\eta_E = m_2\bar{\omega}_2^2/(m_1\bar{\omega}_1^2)$ . We will see in section 2.3 that for the  $^{87}\text{Rb}$ - $^{41}\text{K}$  mixture  $\eta_E = 1$ .

We are now in the position of rewriting the coupled Gross-Pitaevskii equation in the Thomas-Fermi approximation [47]:

$$\begin{aligned} (1/2)(x^2 + y^2 + z^2) + \tilde{g}_1\phi_1^2(\mathbf{r}) + \tilde{g}_{12}\phi_2^2(\mathbf{r}) &= \tilde{\mu}_1 \\ (1/2)\eta_E(x^2 + y^2 + (z - \tilde{z}_0)^2) + \tilde{g}_2\phi_2^2(\mathbf{r}) + \tilde{g}_{12}\phi_1^2(\mathbf{r}) &= \tilde{\mu}_2 \end{aligned} \quad (1.53)$$

where we have defined the rescaled couplings  $\tilde{g}_i = g_i\bar{a}_{ho,1}^{-3}/E_1$ , differential sag  $\tilde{z}_0/\bar{a}_{ho,1}$  and a shifted chemical potential  $\tilde{\mu}_i = (\mu_i - V_{0,i})/E_1$ .

We can now repeat the analysis of the previous section deriving two solutions one in the region of overlap and another one in the region of separation. These two solutions must be properly normalized and connect smoothly and this gives the shape of the interface and the amount of overlap between the two condensates. In particular one finds that the overlapping region is determined by the intersection of two spherical surfaces defined by [47]:

$$\begin{aligned} \Sigma_1 : R_1^2 &= x^2 + y^2 + (z - z_{c1})^2 \\ \Sigma_2 : R_2^2 &= x^2 + y^2 + (z - z_{c2})^2, \end{aligned} \quad (1.54)$$

where, defining  $\gamma_i = g_{12}/g_i$ , the two radii can be expressed as

$$\begin{aligned} R_1 &= \frac{2(\tilde{\mu}_1 - \gamma_2\tilde{\mu}_2)}{1 - \eta_E\gamma_2} + \frac{\eta_E\gamma_2}{(1 - \eta_E\gamma_2)^2}\tilde{z}_0^2, \\ R_2 &= \frac{2(\tilde{\mu}_2 - \gamma_1\tilde{\mu}_1)}{\eta_E - \gamma_1} + \frac{\eta_E\gamma_1}{(\eta_E - \gamma_1)^2}\tilde{z}_0^2 \end{aligned}$$

and the two offsets as

$$z_{c1} = -\frac{\eta_E \gamma_2}{1 - \eta_E \gamma_2} \tilde{z}_0,$$
$$z_{c1} = \frac{\eta_E}{\eta_E - \gamma_1} \tilde{z}_0.$$

From the normalization condition it is possible to see that the intersection of  $\Sigma_1$  and  $\Sigma_2$  is empty if

$$g_{12}^2 - g_1 g_2 > 0$$

which is equivalent to the condition (1.43) that we obtained for the homogeneous system. A detailed analysis of the possible topological configurations of  $\Sigma_1$  and  $\Sigma_2$  can be found in [47] and it is illustrated in figure 1.5.

To obtain the detailed shape of the interface between the two condensates it is necessary to go back to Eq. (1.37): however, based on the insight from the homogeneous case, we expect that the transition is blurred and some overlap occurs also for  $\Delta g$  small and negative.

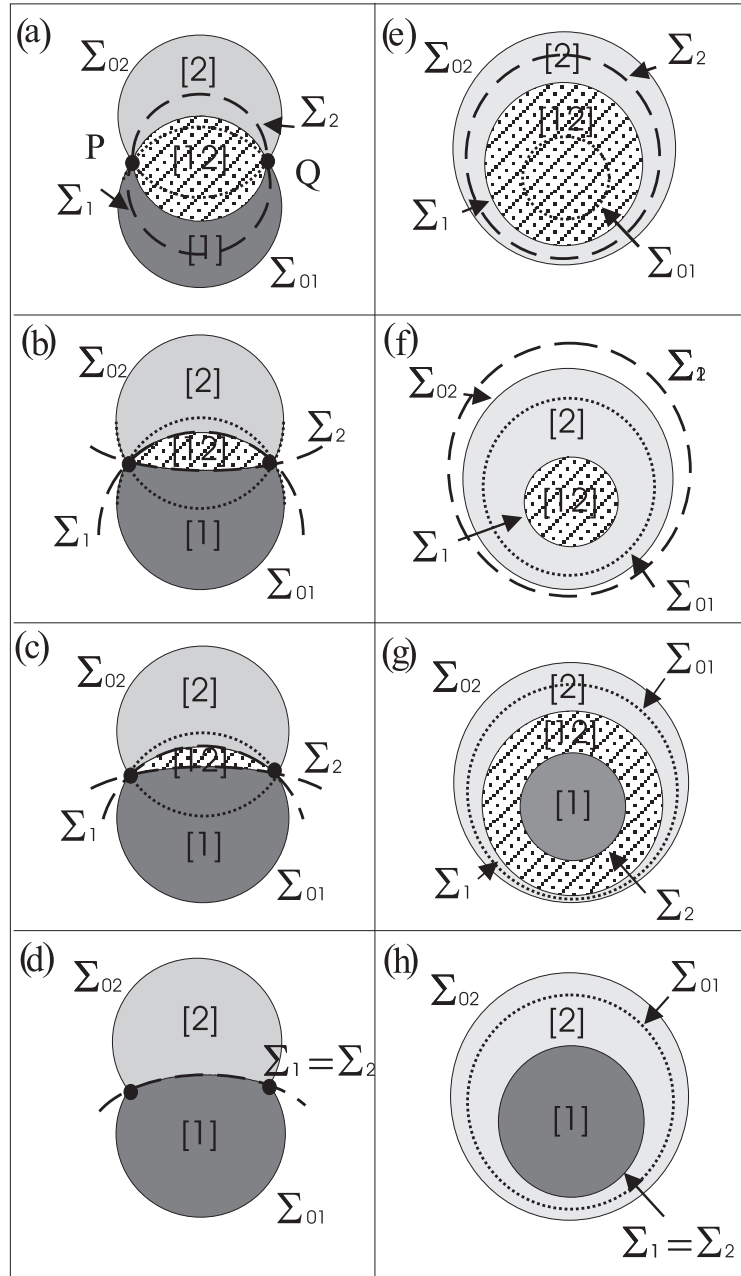


**Figure 1.5.** Possible topologies for a binary mixture of two Bose-Einstein condensates. We can distinguish external overlap ((a),(b) and (c)), phase separation ((d), (h)), full overlap ((e) and (f)) and partial overlap ((g)). Taken with permission from [47].



## Chapter 2

# Experimental apparatus

Machines should work. People should think.

(Richard Hamming)

The experiment reported in this work were realized on a new apparatus that was almost entirely build during my PhD. This new setup has been extensively described in the PhD thesis of my predecessor [49] and therefore I will only review some fundamental features. In particular I will describe in some detail our scheme for the initial cooling of  $^{39}\text{K}$  and  $^{41}\text{K}$  which was realized for the first time in our laboratory [50].

The outline of a typical experimental sequence is the following: two atomic jets of  $^{87}\text{Rb}$  and  $\text{K}$  with high flux density are generated from room temperature vapor in two separate vacuum chambers. These two atomic jets are then collected in a magneto-optical trap (MOT) operating in a third vacuum chamber maintained under ultra-high vacuum (UHV). The atoms from the MOT are then further cooled and transferred into a new kind of magnetic trap. The UHV condition allows to initiate a forced evaporation of the  $^{87}\text{Rb}$  sample in this trap without thermal contact with the vacuum chamber. This evaporative cooling of  $^{87}\text{Rb}$  allows to cool also  $\text{K}$  through interspecies elastic collisions (*sympathetic* cooling. This was demonstrated for the first time in the case of  $^{39}\text{K}$  as we shall see in section 4.1. The lowest temperature that is achieved in our laboratory allows us to enter the degenerate regime for both  $^{87}\text{Rb}$  and  $^{41}\text{K}$  simultaneously as it will be described in part III.

I will now briefly describe the different sections of the apparatus.

## 2.1 Laser sources and vacuum apparatus

Our experimental apparatus is deployed on two separate optical tables. The first one is used to generate and control the different laser frequencies that are needed for the experiment, while the vacuum chamber is located on the second table: this configuration is very useful to isolate the laser sources from vibrations and the atoms from stray light, but has the obvious disadvantage to require a longer optical path to deliver the light on the atoms. In our experiment this problem is overcome using 7 different optical fibers as we shall see later on.

### 2.1.1 Laser sources

As we have seen in section 1.1.1, the laser cooling of alkali atoms requires two different frequencies. For all the species considered in this work we will call *cooler* the laser tuned near the  $|^2S_{1/2}, F = 2\rangle \rightarrow |^2P_{3/2}, F = 3\rangle$  transition and *repumper* the one tuned near the  $|^2S_{1/2}, F = 1\rangle \rightarrow |^2P_{3/2}, F = 2\rangle$ . In the case of  $^{87}\text{Rb}$ , the leakage to the  $|F = 1\rangle$  ground state is small and therefore only a small intensity of repumping light is needed. On the other hand, for the two bosonic isotopes of K, the optical pumping to the  $|F = 1\rangle$  level is strong and the light intensity of the repumper must be at the same level as the cooling one. Actually in this case the force acting on the atom is given by the two lasers as a whole and therefore the distinction between cooler and repumper is only a matter of convention.

Our laser system involves only semiconductor sources and this proved to be very helpful for the stability of the experiment if compared to other schemes based on solid state sources such as Ti:Sa lasers.

### Rubidium

An all-semiconductor approach to the laser cooling of  $^{87}\text{Rb}$  is now traditional in this field as diode laser at the right wavelength of 780nm are readily available on the market.

Since the frequency difference between cooler and repumper for  $^{87}\text{Rb}$  is about 6.8 GHz it is easier to use two different laser diodes for the two colors. We use two Sanyo DL7140-201 laser diodes mounted in an extended cavity in Littrow configuration. Each laser is offset locked to a chosen line in the saturated absorption spectrum obtained from a reference cell.

The power of the laser diode ( $\sim 20$  mW) is enough for the repumper while the cooling light is amplified with a commercial tapered amplifier (Toptica DL-100), which delivers about 600 mW of power without corrupting the spatial mode characteristic.

### Potassium

As pointed out above, a greater power is needed for the repumper of bosonic potassium atoms. This is obtained in our system by means of a commercial grating-stabilized Tapered Amplifier from Toptica (DLX-110). This device delivers up to 600 mW of power and its emission is offset locked on the saturated absorption spectrum of  $^{39}\text{K}$  around 767 nm in the same way as  $^{87}\text{Rb}$ .

Since the frequency difference between cooler and repumper for  $^{39}\text{K}$  ( $^{41}\text{K}$ ) is 254 MHz (462 MHz), it is possible to obtain the cooler light by shifting the repumper with an acousto-optic modulator (AOM) without the need of a further locking scheme. For the sake of minimizing the modifications in the apparatus changing from  $^{41}\text{K}$  to  $^{39}\text{K}$ , this shift is obtained with a double passage in the AOM for  $^{39}\text{K}$  and with a triple passage for  $^{41}\text{K}$ . The cooling light obtained at the right frequency in this way is then fed into a home made tapered amplifier. The tapered amplifier chip (EagleYard EYP-TPA-0765) is optimized for potassium wavelength and delivers about 800 mW with an injected power of around 10 mW operating at around 2.5 A of current.

### Laser splitting and delivering

The power output of the four lasers described before is then split for the several needs of the cooling and transferring processes. In particular each species requires different frequencies for the pre-cooling, the operation of the MOT, the optical pumping toward the magnetic trap and the detection. Only the  $^{87}\text{Rb}$  repumper is held at a fixed frequency by a single passage AOM, while, in view of optimizing all the above mentioned processes, all the other beams have an independent control of frequency and amplitude. This requires a total of about 12 AOM for the three other colors. A schematic view of the splitting system is shown in figure 2.1. A system of  $\lambda/2$  waveplates and polarizing beam splitter cubes splits the power of each single beam which is then fed into a double passage AOM. The only exception to these scheme is the optical pumping beam for  $^{87}\text{Rb}$  which is slightly detuned on

the red side of the  $|S, F = 2\rangle \rightarrow |P, F = 2\rangle$  (see fig. 1.1): for this beam the AOM is used in single passage as shown in figure 2.1. The frequency of all the AOM's is controlled with a VCO and the amplitude of the radio-frequency can be modulated by an external voltage before being sent into a power amplifier.

After the frequency shift and amplitude control, the beams are delivered into seven polarization maintaining optical fibers (OZ Optics PMJ series, core PANDA,  $80\ \mu\text{m}$  cladding). These fibers guarantee the conservation of the linear polarization of the input beam if it is aligned on one of the two axes of their elliptic core. For the two optical fibers where only one color is used the alignment is straightforward, while for the two fibers with two colors, the laser beams are first superimposed with crossed polarization by a polarizing beam splitter cube. The two beams are then launched into the fibers: since the two polarization are crossed, when one of the two beam is aligned on the fast axis the other is automatically aligned on the slow axis and the polarization of both colors is maintained at the output. For the three fibers which are used for all the four colors simultaneously, it is necessary to use an extra trick. As it is shown in figure 2.1, first we superimpose the coolers and the repumpers for both species with the technique explained above, then we align the two polarization using a dichroic waveplate which acts as a  $\lambda/2$  for the K light without affecting the polarization of  $^{87}\text{Rb}$ . Finally we superimpose repumpers and coolers into another polarizing beam splitter: again once the coolers are aligned on one of the axis of the fibers the repumpers are aligned on the other axis and polarization is maintained for all the four colors.

### **2.1.2 Vacuum apparatus**

The design of the vacuum apparatus allows for two special feature of our experiment: separate chambers for the pre-cooling of the two different species and a new kind of magnetic trap which operates under UHV condition. Furthermore optical access to the magnetic trap is possible under three orthogonal direction which makes the installation of a 3D optical lattice easier. All these characteristics are visible in figure 2.2.

The pre-cooling chambers are machined from a single titanium block and rectangular BK7 windows are glued on it using a special purpose vacuum epoxy (Aremco 631C). A detail of the windows glued on the chamber is shown in figure 2.3. Titanium was preferred over stainless steel be-

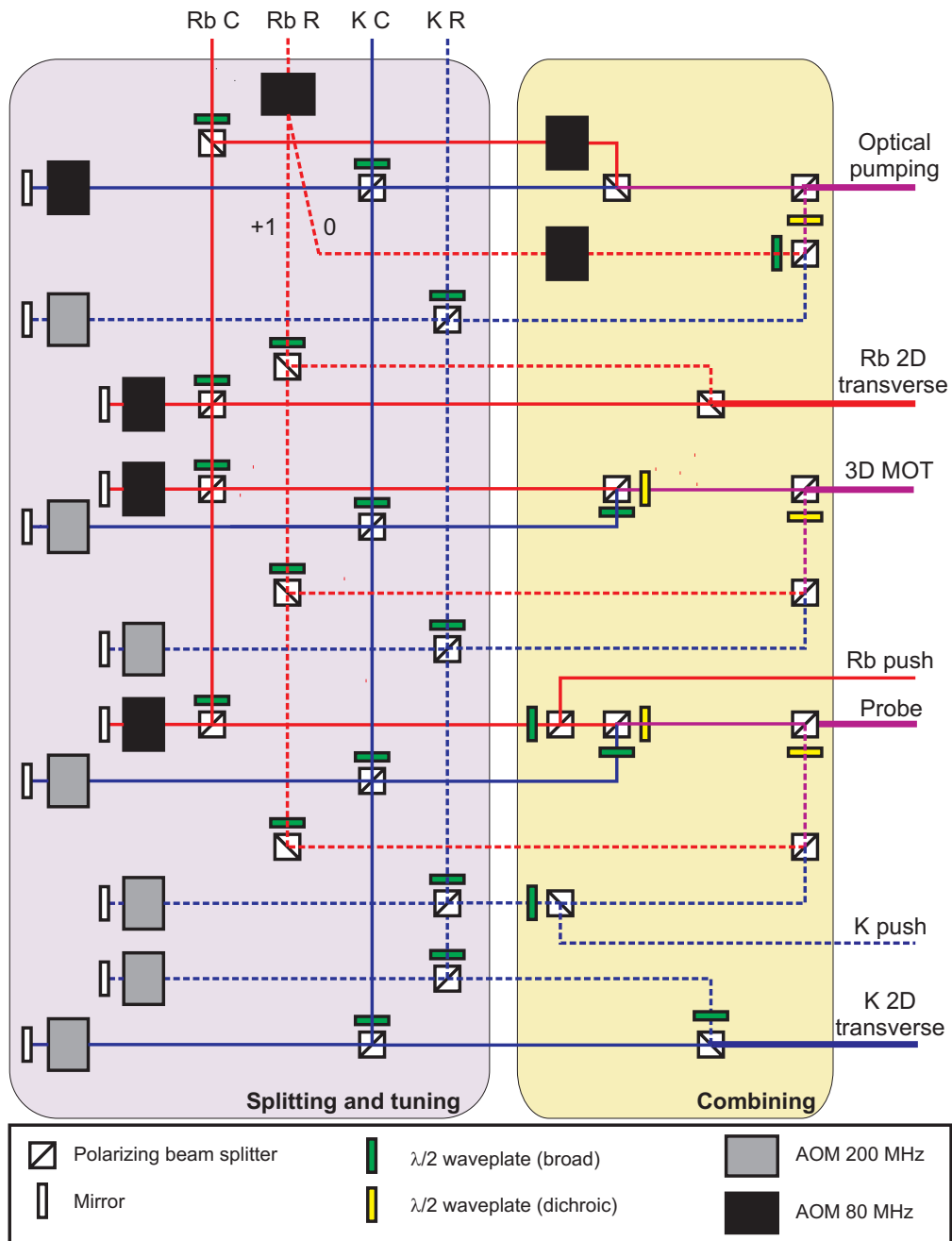


**Figure 2.1.** Scheme of the splitting and the recombining of the lasers for the input of the seven different fibers used in the experiment. Rubidium lasers are indicated in red, potassium in blue, while purple lines indicate where the two colors are superimposed. Dashed line indicates the repumping light. The lenses and the  $\lambda/4$  waveplates needed for the operation of double passage AOM's are not shown in the scheme.

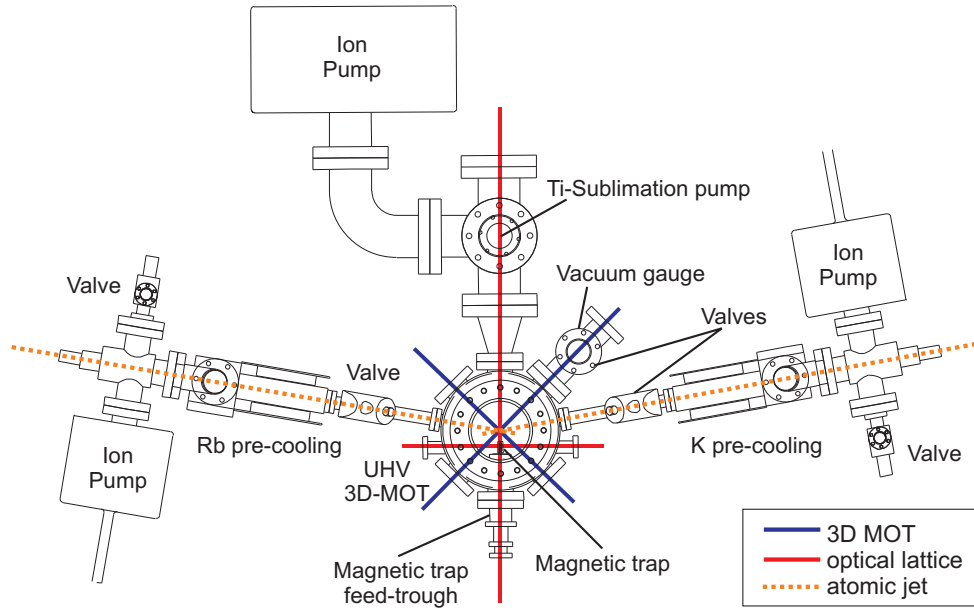


**Figure 2.2.** Sketch of the vacuum apparatus: the three chambers can be seen as well as the magnetic trap feed-through. The axes of the 3D MOT, optical lattice and atomic jets from the pre-cooling stages are indicated.

cause of its thermal expansion coefficient: the value of this parameter in the range  $0 \div 100^\circ\text{C}$  is  $8.9 \times 10^{-6} \text{K}^{-1}$  which is much closer to that of BK7 glass ( $7.0 \times 10^{-6} \text{K}^{-1}$  in the range  $20 \div 300^\circ\text{C}$ ) than the one of stainless steel ( $16 \div 18 \times 10^{-6} \text{K}^{-1}$  in the range  $20 \div 100^\circ\text{C}$ ). The similarity in the thermal expansion coefficient reduces stresses during the bake-out of the apparatus. The rear part of these cells allows for the connection to a vacuum ion pump (20l/s per chamber), to the getters for the alkali gases with their current feed-through and to an all-metal valve that connects each pre-cooling section with the outside. This valve was used at the end of the assembly to bring the pressure into the working range of the ion pump. Furthermore, on the K chamber, we have also connected a reservoir with an enriched sample of  $^{40}\text{K}$  which we have never used so far but in principle allows the apparatus to access the physics of Fermi-Bose mixtures.

To suppress the adsorption of the alkali atoms on the connection between the chamber and the pump, thereby increasing the lifetime of the dispensers, the connection between the pump and the chamber is heated to a temperature of about  $50^\circ\text{C}$ . The lifetime of a single dispenser under normal working condition is about 14 months. Dispensers allow to control the partial pressure of alkali gas in the chamber which is typically ranging

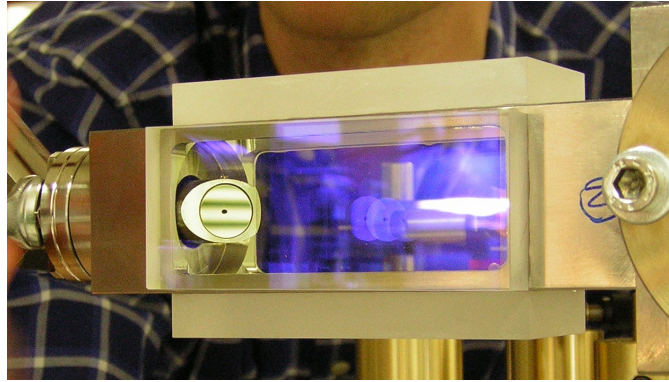


**Figure 2.3.** Detail of the pre-cooling chamber showing the rectangular window glued on the titanium frame of the chamber.

between  $10^{-8}$  and  $10^{-7}$  mbar: this pressure is needed to increase the number of atoms that can be cooled, but, as we already pointed out, is not low enough to obtain Bose-Einstein condensation. For this reason particular care has been used to maintain the biggest possible differential vacuum between each of the two pre-cooling section and the main chamber. This is accomplished first by purely conductive effect given by a 1 cm long hole with a diameter of 1 mm followed by a 10 cm long bellow. To increase further the differential vacuum, the bellow is filled with three cylindrical graphite getters of increasing inner diameter (6, 8 and 10 mm respectively). The bellow is directly connected to the main chamber and decreases the mechanical coupling between the different sections of the vacuum setup.

The main chamber consists of a cylindrical structure machined using nonmagnetic stainless steel. The cylinder has an outer diameter of 180 mm and a height of 45 mm as it is shown in the blueprint of figure 2.4. On the top and the bottom of the cylinder a fit is machined for two CF100 flanges while on the side there is a total of 10 flanges, 6 CF35 and 4 CF16. Two of the CF35 flanges are used to connect the vacuum feed-through of the magnetic trap and the vacuum pump, the other four are aligned on two orthogonal directions offset by  $45^\circ$  with respect to the axis of the magnetic trap and provide the access for the MOT beams. Furthermore, two of the CF16 flanges provide the optical access to the magnetic trap along an horizontal axis orthogonal to the axis of the magnetic trap (see § 2.3), while the other two, offset by  $10^\circ$  extra provide the connection with the bellows from the two pre-cooling chambers. This angle is needed to make sure that the two atomic jets coming from these flanges are not in

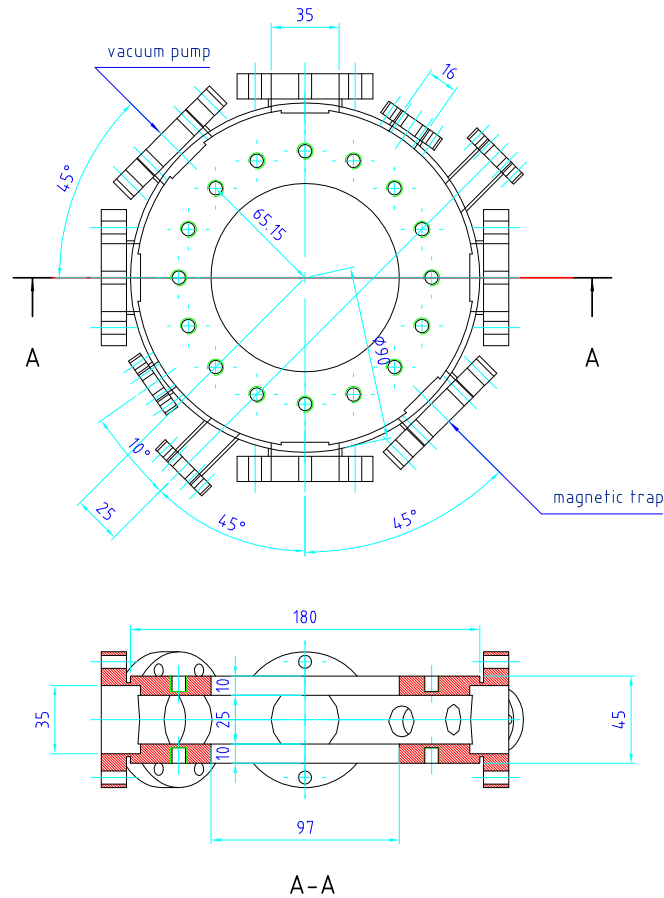


**Figure 2.4.** Blueprint of the main chamber of the experiment. The bigger flanges are CF35 while the small ones are CF16 as indicated. The section shown is taken in the vertical plane along one of the MOT beams direction. Note that two CF100 flanges are installed on top and bottom so that the total height of the chamber is around 90 mm.

the line of sight one of each other.

The flange opposite to the one with the magnetic trap feed-through is connected to the main pumps: one ion pump with a speed of 551/s and a titanium sublimation pump that it is used every month to suppress the throughput of the walls. The ion pump is placed at a relatively big distance from the main chamber to reduce the noise effect from its electric and magnetic field: however to preserve the pumping speed the connection between the pump and the main chamber is obtained with pipes with a 55 mm diameter.

One of the flanges for the access of the MOT beam is connected to a vacuum cross (see figure 2.2) that hosts both a UHV gauge and a valve to the outside environment that can be used in the same way as the one on

the pre-cooling chambers. The hot cathode gauge is not normally operated to avoid the light emission from the incandescent cathode and pressure is inferred from the current flowing in the ion pumps controllers: in particular no current is detected into the main ion pump which place an upper limit of the pressure in the central chamber to below  $10^{-10}$  mbar.

## 2.2 The 2D-MOT

In view of realizing experiments with all the isotopes of potassium (including in principle the least abundant  $^{40}\text{K}$ ) it is highly desirable to have a bright flux of relatively cold atoms. From a very general point of view the higher the partial pressure of the gas the bigger is the total flux of atoms that can be obtained. However the laser cooling is not efficient if the density of the particles is too high because of re-absorption of scattered photons. Furthermore the pressure should be limited in order to preserve the UHV condition near the magnetic trap. As we have shown in the previous section, in our experiment the differential vacuum limits the maximum pressure that can be safely used in the pre-cooling chamber to about  $10^{-7}$  mbar. In this pressure range several schemes have been reported for the generation of an intense flux of cold  $^{87}\text{Rb}$  atoms [51, 52, 53, 54, 55], while the only technique applied to bosonic potassium was the relatively poor transfer between two separated MOT [56, 16].

In our experiment, we extend the scheme of the so-called 2D-MOT already realized for  $^{87}\text{Rb}$  [53, 55] and  $^{40}\text{K}$  [21] to the bosonic isotopes of potassium [50]. This achievement was not totally granted *a priori* due to the peculiar hyperfine structure of these two isotopes that we introduced in section 1.1.2. I will now summarize the structure and operating principle of our 2D-MOT, further details can be found in [49, 50].

### 2.2.1 General principle

The mechanism responsible for the generation of a cold atomic jet from a 2D-MOT is simple: the atoms are cooled and trapped by the simultaneous action of a two counterpropagating laser beams and a quadrupolar magnetic field. The atoms are therefore free to move along a third direction and are allowed to escape the pre-cooling chamber through the small hole visible in fig. 2.3.

The velocity of the atoms can be decomposed into two parts: a velocity along the atomic jet  $v_{\parallel}$  and a velocity in the orthogonal plane  $v_{\perp}$ . The parallel components determines the amount of time the atom will stay in the capturing region of the 2D-MOT: this “cooling time”  $t_c$  will in turn fix how much of the orthogonal kinetic energy will be lost in the cooling process. Note that, since the gas is very dilute, very few collisions occur during the time  $t_c$  and therefore the two velocities distributions maintain different effective temperatures.

The atoms with a very high longitudinal velocity have a very short  $t_c$  and therefore are not cooled to low radial temperatures: these atoms are lost from the jet either before or shortly after leaving the cooling region due to collisions with the walls. On the other hand, atoms with a low  $v_{\parallel}$  will have a longer  $t_c$  and will be cooled to a very low temperature: these atoms will be very collimated (i.e.  $v_{\parallel} \gg v_{\perp}$ ) and will enter the main chamber. The jet formed by the 2D-MOT is therefore obtained with both an actual cooling in the orthogonal plane and a velocity selection along the axis of the trap. This process can be further enhanced by adding another laser beam along the direction of the atomic jet: this beam will push the atoms into the jet enabling the 2D-MOT to capture also the part of the atoms propagating backward and those having a poor collimation ( $v_{\parallel} \lesssim v_{\perp}$ ). We will come back to this point in the next section.

These qualitative insight into the mechanisms responsible for the formation of the cold atomic jet in a 2D-MOT are confirmed by numerical simulation based on the actual force acting on the atoms. These simulation are detailed in [50] and extend to the potassium case the model developed in [54] for  $^{87}\text{Rb}$ : this model assumes that the total force acting on the atoms is the radiation pressure of each beam separately. Starting from Eq. (1.1) one finds:

$$\mathbf{f} = \frac{\hbar\Gamma}{2} \sum_i \mathbf{k}_i \frac{S_i}{1 + S_T},$$

where  $S_T$  is the sum of all the six saturation parameters. The tricky part of extending this model to bosonic potassium is in the fact that the force is due to both cooler and repumper and that the two have the same intensity. However the qualitative agreement between the model and the experimental findings shown in the next section confirm that we understand the mechanism of the 2D-MOT. I note here that, after the publication of our work, another work devoted to a  $^{87}\text{Rb}$  2D-MOT operating in a slightly higher pressure range [57] confirmed our findings.

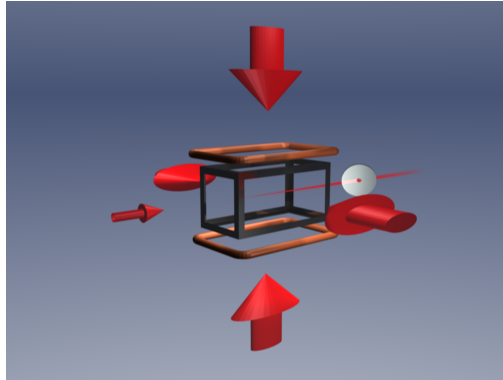


**Figure 2.5.** Scheme of our 2D-MOT: the frame of the vacuum chamber, the coils, the pierced mirror and the direction of the different laser beams are shown.

### 2.2.2 Experimental parameters

A schematic picture showing all the key element of our 2D-MOT is shown in figure 2.5. I will now describe all the parts of this pre-cooling stage.

#### Transverse beams

From the mechanism described in § 2.2.1, it is clear that the longer the cooling time  $t_c$  the larger is the velocity class that will enter the atomic jet in the main chamber. One way to increase this time is to stretch the interaction region along the axis of the trap: this is the reason why the window of the pre-cooling chamber have a rectangular  $80 \times 35$  mm shape (see fig. 2.3) and the beams have an elliptic shape with a minor waist of 9.4 mm and an aspect ratio of 1 : 3. This shape is obtained with a simple cylindrical telescope. The two beams are then retroreflected and polarization is rotated in such a way to achieve the usual  $\sigma^+ - \sigma^-$  configuration.

The optimal power and detuning of the 2D-MOT of  $^{87}\text{Rb}$ ,  $^{39}\text{K}$  and  $^{41}\text{K}$  are shown in table 2.1. Indeed we found that increasing the power still increase the flux density [50], but part of the power is needed to operate the 3D-MOT.

#### Magnetic field

The magnetic quadrupole field is created by two rectangular  $90 \times 40$  mm coils attached around the vertical windows and insulated from the vacuum apparatus with a 1 mm thick Teflon spacer. At the typical current of 4 A, the magnetic field gradient in the vertical and horizontal radial directions

	Power [mW]		Detuning [ $\Gamma$ ]	
	Cooler	Repumper	Cooler	Repumper
<sup>87</sup> Rb	50	3	-1.2	-0.5
<sup>41</sup> K	70	20	-3.0	-2.5
<sup>39</sup> K	70	20	-5.8	-3.9

**Table 2.1.** Optimal values for power and detuning of each of the two retroreflected transverse beams of the 2D-MOT with a magnetic field gradient of around 15 G for the isotopes used in this work.

is about 15 G, while, along the trap axis, it is much smaller and will be neglected in the following. The current in each coil can be controlled independently which allows to move the position of the zero of the magnetic field along the vertical direction. An additional coil can shift the beam along the horizontal radial direction, but, as a matter of fact, it isn't used.

### Push beam

The “push” beam has a diameter of about 1.5 mm and is reflected away from the chamber by a 45° metallic mirror in which the 1 mm exit hole is drilled<sup>1</sup>.

As expected from ref. [53, 55], within our pressure range, the presence of a push beam is required to have a significant flux and furthermore we have experimentally found that the parameters of the push beam are very critical. In particular we found for both Rb and K that if the push beam contains both cooler and repumper, flux is very much depleted. This is due to the fact that if both lights are present, the atoms are pushed also after leaving the pre-cooling chamber, while if only one radiation is present the atoms are optically pumped into a dark state shortly after leaving the interaction region. Beside the effect of an unwanted excessive acceleration, the persistent action of the push beam heats the atoms in the jet leading to the depletion of the flux because of collision with the graphite getters in the transfer bellow. This is the reason why the push beam for <sup>87</sup>Rb contains only cooling light as indicated in the scheme of Fig. 2.1. Surprisingly we find that for <sup>39,41</sup>K the flux is way better with only the repumping instead of the cooling beam. This can be again traced back to the tight hyperfine structure of these bosonic isotopes: a beam red detuned with respect to

---

<sup>1</sup>This mirror was originally placed in this position to allow the insertion of a beam propagating against the atomic jet (2D<sup>+</sup> configuration [55, 57]). However we found no improvement in this configuration within our pressure range.

the  $|S, F = 2\rangle \rightarrow |P, F = 3\rangle$  is nearly resonant with the  $|S, F = 2\rangle \rightarrow |P, F = 1, 2\rangle$  and therefore causes a strong optical pumping which requires a big amount of repumping light from the transverse beam. On the other hand, a beam red detuned from the  $|S, F = 1\rangle \rightarrow |P, F = 1, 2\rangle$  transition is closer to resonance with the  $|S, F = 1\rangle \rightarrow |P, F = 0\rangle$  transition which is closed and any repumping from the  $|S, F = 2\rangle$  manifold is carried over more easily since the cooling power in the transverse beam is bigger. Of course the optical pumping can be also reduced decreasing the overall intensity but this in turn weakens the pushing effect on the atoms; due to absorption the intensity is further reduced near the exit region of the chamber which is the most critical for the formation of a good atomic flux. The peculiar interplay between the intensity and the detuning of the push beam can be reproduced with the model outlined above and gives a good qualitative agreement with the observed behavior [50]. The optimal values for the parameters of the push beams are summarized in table 2.2.

	Transition	Power [mW]	Detuning [ $\Gamma$ ]
$^{87}\text{Rb}$	$2 \rightarrow 3$	5	-1.5
$^{39}\text{K}$	$1 \rightarrow 1, 2$	6	-5.2
$^{41}\text{K}$	$1 \rightarrow 1, 2$	6	-4.5

**Table 2.2.** Optimal transition and relative values for power and detuning of the 2D-MOT push beam for the isotopes used in this work.

### 2.2.3 Flux density measurement

A reliable measurement of the flux generated by the 2D-MOT is a very important tool to optimize the parameters both of the beams and of the magnetic field. This measurement is obtained measuring the decay of the fluorescence detected in the main chamber after blocking the atomic jet [53]. Once the operating point is found, the daily alignment of the 2D-MOT is performed measuring the load rate of the 3D-MOT as it is explained later on.

The atomic jet is exposed to a vertical sheet of light placed at a distance  $L = 30$  cm from the hole in the mirror and the fluorescence is collected with a lens on a broad area photodiode. The peak intensity of the probe beam is high enough to saturate the transition and power is divided between cooler and repumper with a 2 : 1 ratio. The jet is shut off shining a resonant

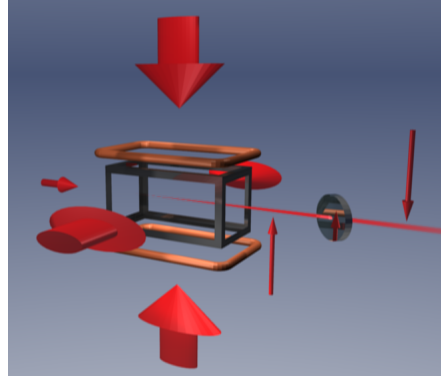


**Figure 2.6.** Schematic side view of the 2D-MOT: the thin red arrow near the exit hole marks the position of the “plug” beam which is used to interrupt the atomic flux in order to measure the flux density. The arrow behind the mirror represents the probe sheet of light.

beam before the mirror hole [58]: when this beam is on the atoms do not leave the pre-cooling chamber anymore and the fluorescence in the main chamber decays to zero. The lower the peak velocity in the jet the slower the decay is. The position of this “plug” beam is shown in figure 2.6.

More quantitatively, the fraction of atoms crossing the sheet of light in a time  $dt$  is given by

$$dN = \int d^2S d^2v_{\perp} dv_{\parallel} f(\mathbf{r}, \mathbf{v}) v_{\parallel} dt = \int dv_{\parallel} n_1(v_{\parallel}) v_{\parallel} = dt \int dv_{\parallel} \rho_{\parallel}(v),$$

where  $f(\mathbf{r}, \mathbf{v})$  is the distribution function and  $\rho_{\parallel}(v)$  is the flux density which we want to measure. If the atomic beam is interrupted at  $t = 0$  the atoms which contribute to the fluorescence signal at time  $t$  are those having a parallel velocity between 0 and  $L/t$ , namely

$$N(t) = \int_0^{L/t} dv_{\parallel} n_1(v_{\parallel}) = - \int_0^t du n_1(L/u) L/u^2 du = - \int_0^t du \rho_{\parallel}(L/u) 1/u du.$$

From the above expression we have that the flux density  $\rho_{\parallel}(v)$  is given by:

$$\rho_{\parallel}(v = L/t) = -\frac{t}{\eta} \frac{d}{dt} S(t), \quad (2.1)$$

where  $\eta$  is a calibration factor taking into account the atomic scattering rate ( $\Gamma/2$ ), the quantum efficiency of the photodiode and the numerical aperture of the collection lens.

A typical experimental acquisition of  $S(t)$  is shown in figure 2.7 together with the flux density inferred using Eq. (2.1). Applying the proper calibration factor we obtain that the total flux for bosonic K corresponds to

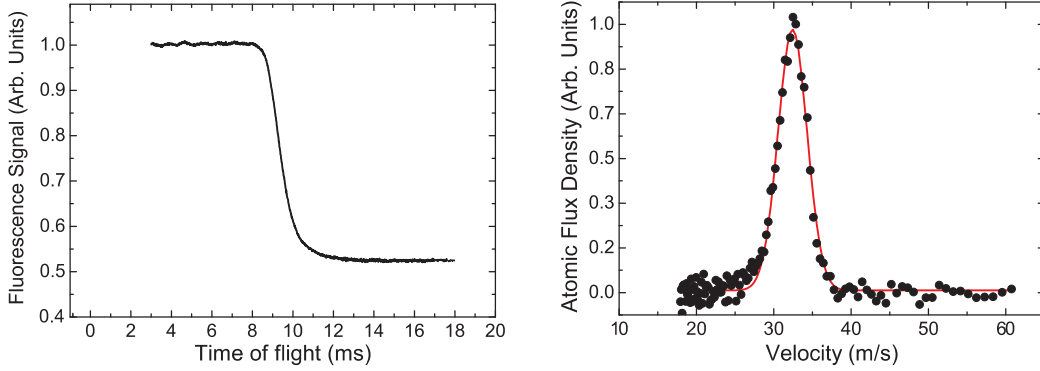


**Figure 2.7.** (Left) Typical experimental acquisition of the fluorescence signal  $S(t)$ . At  $t = 0$  ms the plug beam is turned on and after a delay the fluorescence starts decaying to zero. (Right) Measured velocity distribution of atomic beam obtained by applying Eq. (2.1) (dots) and Gaussian fit (solid line). The resulting peak velocity is 32 m/s with a FWHM of 4.5 m/s.

$6.2 \times 10^{10}$  and  $5.2 \times 10^9$  atoms/s for  $^{39}\text{K}$  and  $^{41}\text{K}$  respectively at a nominal pressure of  $7 \times 10^{-8}$  mbar. The difference among the two isotopes can be almost entirely attributed to their respective natural abundance. The most probable longitudinal velocity for  $^{41}\text{K}$  ( $^{39}\text{K}$ ) is found to be 35 m/s (33 m/s).

In the case of  $^{87}\text{Rb}$ , the performances of our system are similar to those of references [53, 55], namely a total flux of about  $5.2 \times 10^9$  atoms/s and a most probable velocity of about 30 m/s.

Another important parameter is the divergence of the atomic jet and it is measured in the following way: the fluorescence is recorded on a CCD camera with long exposure time ( $\sim 100$  ms) from the horizontal radial direction. The acquired image can be integrated along the two directions and fitted with two Gaussian functions: on the horizontal axis of the image, which corresponds to the axis of the jet, the shape is given by that of the detection beam while on the vertical direction the intensity of the detection beam can be considered constant and the shape of the fluorescence is determined by the profile of the atomic jet. By independently measuring the size of the detection beam it is possible to calibrate the magnification of the system and obtain the measure of the vertical size of the atomic jet. From this measurement, knowing the distance  $L$  it is possible to determine the atomic K jet divergence as  $34(6)$  mrad.

## 2.2.4 Loading of the mixed 3D-MOT

In view of transferring the two atomic species to a magnetic trap it is necessary to have them overlapped in space. In our experiment this is achieved

	Cooler		Repumper	
	Detuning [ $\Gamma$ ]	Power [mW]	Detuning [ $\Gamma$ ]	Power [mW]
$^{87}\text{Rb}$	-2.8	40	-0.5	6.0
$^{39}\text{K}$	-3.0	45	-7.5	23
$^{41}\text{K}$	-4.0	22	-4.0	22

**Table 2.3.** Parameters of the 3D-MOT for the atomic species used in this work. The total power for the six beams is indicated.

superimposing the four colors needed for the 3D-MOT at the input of an optical fiber. As I have explained in § 2.1.1, at the output of the fibers the four colors do not have however the same polarization which is instead required for the operation of a MOT. This problem is overcome by making a first split with a  $\lambda/2$  waveplate and a polarizing beam splitter cube: when the power is divided in a 1 : 1 ratio the two orthogonal polarizations at the input are present at the output ports with the same intensity in both arms. A following two stage polarized splitting, first with the ratio 1 : 2 and then again with a ratio 1 : 1 allows the generation of six independent beams with the same intensity and the same ratio of cooler and repumper as the one present at the output of the fiber. These six independent, linearly polarized beams are delivered to the main chamber and their polarization is changed by a  $\lambda/4$  waveplate. The power and detuning of the MOT beams is summarized in table 2.3.

Since all the species used in this work have the same magnetic moment, the only difference in the position of the two MOT's is due to differences in the intensity balance or in the position of the laser beams: the latter is suppressed by the use of a single optical fiber for the two 3D-MOT, while the former effect can be only introduced by a different behavior of the waveplates between 780 nm and 766 nm. Indeed such an effect is observed and the optimized position of the  $\lambda/4$  waveplates for  $^{87}\text{Rb}$  is slightly different from the one of K. We therefore use the  $\lambda/4$  waveplates to optimize the superposition of the two clouds without observing a particular degradation of the loading of the two traps.

The magnetic field of our 3D-MOT is generated by two circular coils which provide the required gradient of about 15 G/cm at 4 A of current. A further set of three pairs of coils provides the compensation of stray fields: this compensation is carried over looking at the isotropy of the explosion of the  $^{87}\text{Rb}$  MOT after switching off the magnetic field.

During the normal running of the experiment we run the experiment at a lower pressure to be conservative on both the dispensers and the vacuum and therefore the loading of the 3D-MOT is reduced with respect to the maximum flux indicated in the previous section. The daily alignment procedure involves mainly adjustments on the alignment of the fibers and on the direction of the push beam of the 2D-MOT: the compact splitting design limits the misalignments of the 3D-MOT which is very robust. The loading of the MOT is monitored from the fluorescence collected with a high gain photodiode. Typical number of atoms in the MOT at the end of the loading phase are  $2 \times 10^9$  for  $^{87}\text{Rb}$ ,  $1 \times 10^7$  for  $^{39}\text{K}$  and  $3 \times 10^6$  for  $^{41}\text{K}$ .

### 2.2.5 Preparation of the atoms for magnetic trapping

As we will see in § 2.3, to obtain a good transfer into the magnetic trap it is desirable to achieve the highest possible density. This second task is realized introducing a short phase ( $\sim 100$  ms) of compressed MOT at the end of the loading of the 3D-MOT. This is done increasing the magnetic gradient by a factor two and reducing the  $^{87}\text{Rb}$  repumper intensity to almost zero while shifting the  $^{87}\text{Rb}$  cooler away from resonance. This suppresses photon re-scattering and reduces the size of the cloud. For K the procedure is slightly different in that the repumper power is held constant while the frequency is shifted almost  $9\Gamma$  away from resonance while cooler light is brought closer to the resonance: this optimizes the transfer to the magnetic trap. To compensate for the heating introduced during the compression an optical molasses is applied for a few ms<sup>2</sup>. As not all the hyperfine states can be magnetically trapped, one has also to prepare the atoms in the right hyperfine level which, for all the experiments reported in this work is the  $|2, 2\rangle$ . This hyperfine transfer is done by optical means: first atoms are pumped into the  $F = 2$  manifold leaving the repumper on for one extra millisecond at the end of the optical molasses. Then a uniform magnetic field of about 2 G is turned on to define a quantization axis and light with  $\sigma^+$  polarization is shone along this axis. Opposite to all the other functions of the experiments the light for optical pumping is tuned slightly below the  $|S, 2, 2\rangle \rightarrow |P, 2, 2\rangle$  as this gave the best efficiency to the process. The optical pumping phase lasts  $300 \mu\text{s}$  and at the end all the lights are turned off in the proper order to leave the atoms polarized at 80% into the  $|2, 2\rangle$  state.

<sup>2</sup>This is to avoid a decrease in the density of the K sample for which –as we have seen– the laser cooling is not as efficient as for  $^{87}\text{Rb}$ .

At this stage atoms can be loaded into the magnetic trap: before describing the details of this process, I will introduce the novel kind of magnetic trap which is used in our apparatus.

## 2.3 The magnetic millimetric trap

### 2.3.1 General principle

The interaction between an atom with a permanent magnetic dipole moment and an inhomogeneous magnetic field can be written as

$$V(\mathbf{r}) = -\boldsymbol{\mu} \cdot \mathbf{B}(\mathbf{r}). \quad (2.2)$$

If the time variation of  $\mathbf{B}$  seen by the atom are on a timescale  $\tau$  such that

$$\tau \gg \frac{\hbar}{\mu B},$$

the direction of the atomic magnetic moment is always parallel or antiparallel to the local magnetic field and the interaction simplifies to:

$$V(\mathbf{r}) = m_F g_F \mu_B B(\mathbf{r}) \quad (2.3)$$

where  $m_F$  is the magnetic quantum number of the atomic state,  $g_F$  is the Landé  $g$ -factor and  $\mu_B$  is the Bohr magneton.

Depending on the sign of  $m_F g_F$  an atomic  $|F, m_F\rangle$  state can be classified as either *low-field* seeker ( $m_F g_F > 0$ ) or *high-field* seeker ( $m_F g_F < 0$ ). Since it is impossible to have an isolated magnetic field maximum in free space [59], only low-field seeker states can be magnetically trapped by a current configuration which realizes a minimum of the field. For  $^{87}\text{Rb}$ ,  $^{39}\text{K}$  and  $^{41}\text{K}$  which have the same magnetic quantum numbers, these trappable states and their magnetic moments are summarized in table 2.4.

State	$m_F g_F \mu_B / \hbar$
$ 2, +2\rangle$	1.4 MHz/G
$ 2, +1\rangle$	0.7 MHz/G
$ 1, -1\rangle$	0.7 MHz/G

**Table 2.4.** Magnetically trappable states of the atomic species used in this work and relative magnetic moment.

The simplest current configuration that realizes a trapping potential is given by two parallel coaxial coils with opposite currents. These coils realize

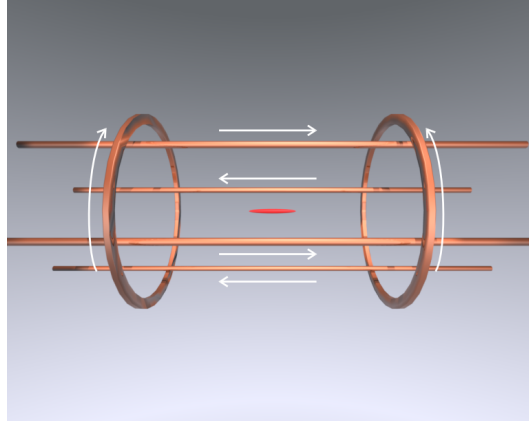


**Figure 2.8.** Layout of the conductors creating a Ioffe-Pritchard trap. The white arrows indicate the sense of the current and the red region marks a surface of constant field near the minimum.

a magnetic quadrupole trap whose field profile is given by

$$B(\mathbf{r}) = B'(\rho^2 + z^2)^{1/2}, \quad (2.4)$$

where we have introduced cylindrical coordinates taking  $z$  as the axis of the system and the origin in the center of symmetry of the two coils, where the magnetic field is zero.

The most important drawback of this configuration is related to this zero in the field: an atom which stays a long time in the region of weak magnetic field around the minimum will have a finite probability to undergo a spin flip and therefore being repelled by the magnetic field gradient. Such a process is called *Majorana spin-flip* and it is the limiting factor for the lifetime of a quadrupole trap at low temperatures [60, 61].

Several schemes exist to realize a magnetic field configuration which has a local minimum at a non-zero value. We will take a closer look to one of the most successful of these: the so-called Ioffe-Pritchard (IP) configuration [62]. The layout of the conductors of a IP trap is shown in figure 2.8: two cylindrical coils with the same current create a Helmholtz field whose minimum is not zero and four current wires carrying alternate current create a gradient in the plane orthogonal to the trap axis. The total field is given by the sum of these two contributions:

$$\mathbf{B}(\mathbf{r}) = B' \begin{pmatrix} x \\ -y \\ 0 \end{pmatrix} + \frac{B''}{4} \begin{pmatrix} -2xz \\ -2yz \\ 2z^2 - x^2 - y^2 \end{pmatrix} + B_0 \begin{pmatrix} 0 \\ 0 \\ 1 \end{pmatrix}. \quad (2.5)$$

The modulus of the field can be expanded around the minimum as:

$$B(\mathbf{r}) \simeq B_0 + \left( \frac{B'^2}{2B_0} - \frac{B''}{4} \right) \rho^2 + \frac{B''}{2} z^2 \quad (2.6)$$

thus, if the condition  $2B'^2 > B_0 B''$  is fulfilled, not only the potential has an isolated minimum which is different from zero, but also the shape of the trapping potential is harmonic.

Combining Eq. (2.3) and Eq. (2.6) it is easy to see that the trap frequencies are

$$\begin{aligned} \omega_z^2 &= \frac{m_F g_F \mu_B}{m} B'' \\ \omega_\perp^2 &= \frac{m_F g_F \mu_B}{m} \left( \frac{B'^2}{B_0} - \frac{B''}{2} \right) \end{aligned} \quad (2.7)$$

and the aspect ratio is

$$\mathcal{A}_R = \sqrt{\frac{B'^2}{B_0 B''} - \frac{1}{2}}. \quad (2.8)$$

In practice traps are build with a high aspect ratio ( $\mathcal{A}_R \sim 10$ ) so that

$$\frac{B'^2}{B_0} \gg \frac{B''}{2} :$$

this means that the curvature given by the two pinch coils mainly affects the axial frequency while the radial frequency is almost entirely controlled by the radial gradient and by the bias field  $B_0$ . In particular one sees that  $\omega_\perp \propto B_0^{-1/2}$  and therefore it is easy to change the trap geometry by tuning the bias field. One important consequence of Eq. (2.7) is that, as we already anticipated, the trap shape is the same for all the species considered in this work. The only effect of the different masses is therefore to introduce a rescaling of the trapping frequencies.

We will now see how a Ioffe-Pritchard trap is implemented in our system.

### 2.3.2 Mechanical structure

The conductors layout which realizes our magnetic trap is shown in figure 2.9. The main structure is machined out of a pure, oxygen-free copper tube in which four cut are open: the resulting shape is that of four bars connected by two pairs of arcs. The current flows in the bar and in the arcs in the right path to reproduce the Ioffe-Pritchard configuration of figure 2.8. This structure is vacuum brazed on a chip on which copper is deposited. The

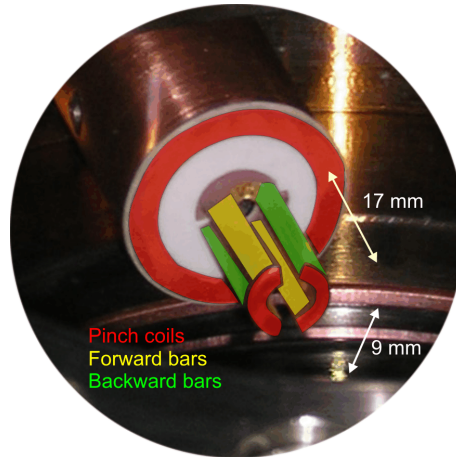


**Figure 2.9.** Picture of the millimetric magnetic trap taken inside the vacuum chamber. Characteristic dimensions are indicated.

chip has two functions: on the back side it provides the interface for the current feed-through while on the front side it hosts the connections with the trap itself and another circular trace (visible in figure 2.9) which refines the axial confinement. A similar structure was reported in [63].

At the typical operating current of 70 A the radial gradient is calculated to be  $B' \simeq 370 \text{ G/cm}$ , the axial curvature is  $B'' \simeq 130 \text{ G/cm}^2$  and the bias field is around 23 G. This is a rather high value and it is compensated by two coaxial coils placed outside the vacuum apparatus: one of these coil is in series with the magnetic trap and reduces the bias field to about  $B_0 \simeq 6 \text{ G}$ , the other coil is powered by an independent power supply and allows us to dynamically change the bias field. According to Eq. (2.7) this gives the following trapping frequencies for  $^{87}\text{Rb}$  in the  $|2, 2\rangle$  state:  $\omega_{\perp} = 2\pi \times 193 \text{ Hz}$ ,  $\omega_z = 2\pi \times 14.6 \text{ Hz}$  which must be compared to the measured value of  $2\pi \times 208 \text{ Hz}$  and  $2\pi \times 16.8 \text{ Hz}$  respectively. The small discrepancy is certainly related to the size of the conductors which plays a non negligible role. The calculated trap depth at 70 A is about 3.5 mK.

This kind of millimetric structure has several advantages over both the traditional magnetic trap and the so-called microtraps or traps on microchips. A quick comparison between the different traps is shown in table 2.5. All the key advantages, are related to the small structure. First the ohmic resistance of our trap is about  $5 \text{ m}\Omega$  and therefore the power dissipation is limited to a few watts. This is in sharp contrast with traditional traps which usually require several kilowatts of electric power and correspondingly demand an efficient cooling mechanism. Strictly related to this

	Standard	m-trap	$\mu$ -trap
Vacuum	Out	In	In
Current	$\sim 100$ A	$\sim 100$ A	$\sim 1$ A
Power	$\sim 1.5$ kW	$\sim 50$ W	$\sim 10$ W
$\nu_r$	100 Hz	500 Hz	1 kHz
Inductance	$\sim 10$ mH	Negligible	Negligible
Pressure	UHV	UHV	HV
$N_0$	$\gtrsim 10^6$	$\lesssim 10^6$	$\lesssim 10^5$
Opt. access	Custom	Limited	Restricted

**Table 2.5.** Comparison between the different approach to magnetic trapping.

is the much higher inductance value of the usual traps: this translates in longer timescale for the switch-off of the trap which is an important issue for time-of-flight techniques. Furthermore, although the trapping frequencies and hence the condensate production rate are lower than those of a  $\mu$ -trap, it is easier to transfer the atoms into the trap and therefore our trap might operate far from the MOT in a UHV environment: I will come back to this point in § 2.3.3. Another important difference is that optical access, although limited by the Ioffe bars, is available in three direction, while in a  $\mu$ -trap one of the directions is blocked by the chip. A drawback related to the size of the trap is the reduced depth: also this point will be discussed in next section.

An important issue which I discuss now is instead that of the powering of this device. The current feed-through that supplies our trap has to satisfy four different tasks: provide the current for the magnetic trap with the minimum power dissipation, remove the generated heat, be vacuum tight at the UHV level and allow the optical access along the axis of the magnetic trap. To comply with all these requirements the current leads of the feed-through are two coaxial cylindrical copper shells split into two segments which are displayed in figure 2.10.

The first segment is brazed on the back side of the chip: the outer diameter of the outer conductor is 23 mm while the inner diameter of the inner conductor is 12 mm the gap between the two conductors is only 1 mm, the total length of this section is 70 mm. The two shells are held in place by the connection to the outer segment. This is the most complicated structure and it is shown with a section in figure 2.11. The outer segment is composed by three pieces: two copper shells which are attached to the inner

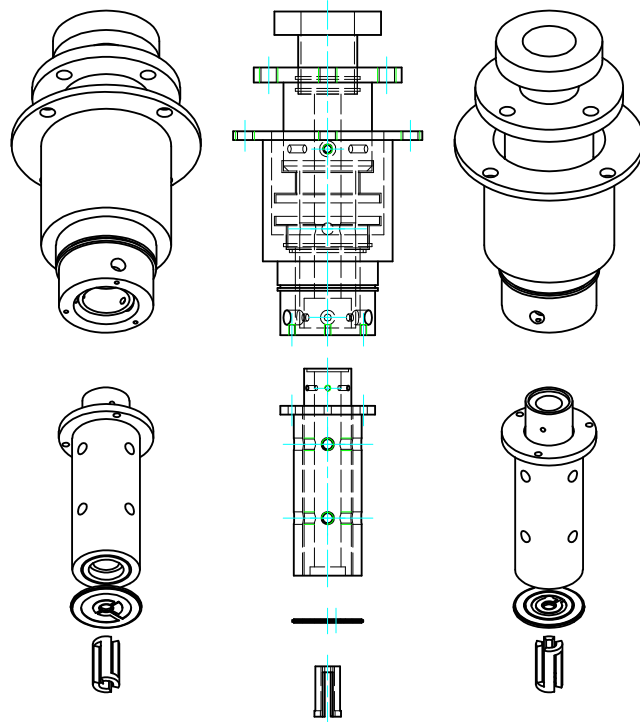


**Figure 2.10.** Current feed-through for the magnetic trap (shown on the bottom). The feed-through is formed by two segments: the bottom one is attached to the chip (also shown), while the upper segment provides vacuum isolation and is used to make the electrical connection to the power supply.

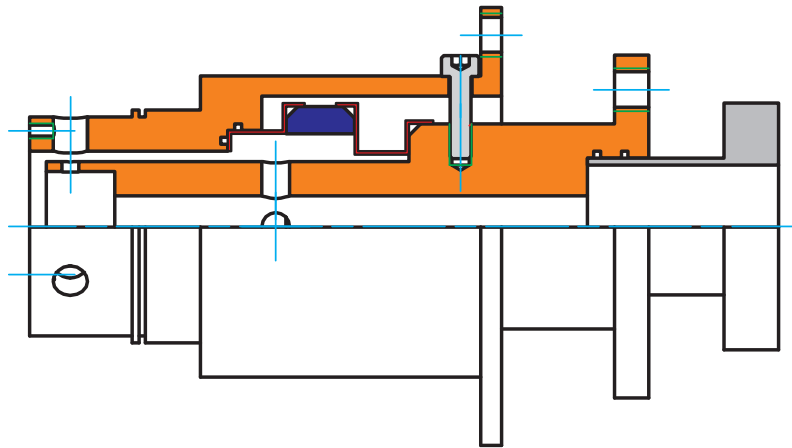


**Figure 2.11.** Detail of the outer segment of the current feed-through for the magnetic trap: the copper shells are marked in orange, the ceramic ring in blue and the steel gaskets are marked in red. The outer gray element is a CF16 nipple.

conductors and which complete the electrical circuit and a structure which provides the electrical isolation between the two conductors and makes the whole structure vacuum tight. This structure is built with two 0.5 mm-thick steel structures which contain a ceramic ring. The special steel used is Kovar which can be brazed both on copper and on ceramics and thus provides the connection between the two shells of the outer segment. Beside mechanical tolerances, the main difficulty in the production of this part is related to the stresses imposed on the ceramic ring during the brazing process: thermal stress induced by the very different expansion coefficients can cause cracks in the ceramic ring which make the feed-through leaking. The hollow part of the cylinder is closed by a small BK7 window mounted on a CF16 nipple (shown in gray in figure 2.11) brazed to the inner conductor of the outer segment while the whole feed through is attached to the vacuum apparatus with a CF35 flange (not shown).

The vacuum brazing process used to build the feed through is the best possible test for the thermomechanical stability of the device: during the brazing the temperature is about 700 °C, something which is far from being reached under normal duty. Nevertheless, in a bench test carried out in air we measured that the temperature of the trap can reach more than 100 °C after four minutes of continuous operation at 100 A. At this temperature it is critical that heat is dissipated through the feed-through and not through the walls of the main chamber: this could lead to an increased outgassing which can easily affect the UHV condition.

Based on rather conservative calculations we expect that the thermal resistance of the feed-through is around  $3^\circ\text{C}/\text{W}$  which means that, if the dissipated power at the trap position is around  $10\text{W}$ , the trap temperature will be only  $30^\circ\text{C}$  higher than the temperature of the outside part of the feed-through. Although air convection is not an efficient cooling mechanism the outside temperature is always below  $50^\circ\text{C}$  which means that the temperature of the trap is about  $80^\circ\text{C}$ . We measured that in these conditions the heating of the chamber is limited and vacuum is not affected. More problematic is the temperature stability of the system: due to the low thermal resistance the trap heats up during operation and cools down during the loading of the MOT. Indeed we observe that operating the trap at a different temperature each time compromise the stability of the evaporation and therefore we optimized the trap duty cycle to limit the thermal cycle. Particular attention is given to operate the trap continuously so to keep an equilibrium temperature: in this way the trap can operate with a good stability and without need for external cooling.

### 2.3.3 Transfer from the 3D-MOT

The loading of the atoms into the millimetric magnetic trap is not an easy task and a good effort was needed to have it operate properly. The size of our 3D-MOT is typically a few millimeters at a temperature slightly lower than  $200\mu\text{K}$ . At this temperature the size of the magnetic trap is much smaller, meaning that the atoms have to be compressed before being transferred in this potential. Adiabatic compression rises the temperature and one must pay attention not to bring the atom too close to the trap depth. Furthermore, as one can see in figure 2.2, the trap is  $27\text{mm}$  apart from the center of the 3D-MOT, a separation that is required since the trap structure is not compatible with the size of our MOT beams.

These two problems are almost always present to different extent in all the experiments on ultracold atoms and they are usually dealt with by trapping the atoms in a mobile magnetic quadrupole trap. This trap captures the atoms from the MOT and releases them in the magnetic trap. The mobile trap is usually realized either with several quadrupole traps powered in sequence [64] or by physically displacing the magnetic coils [65]: we adopted this second strategy.

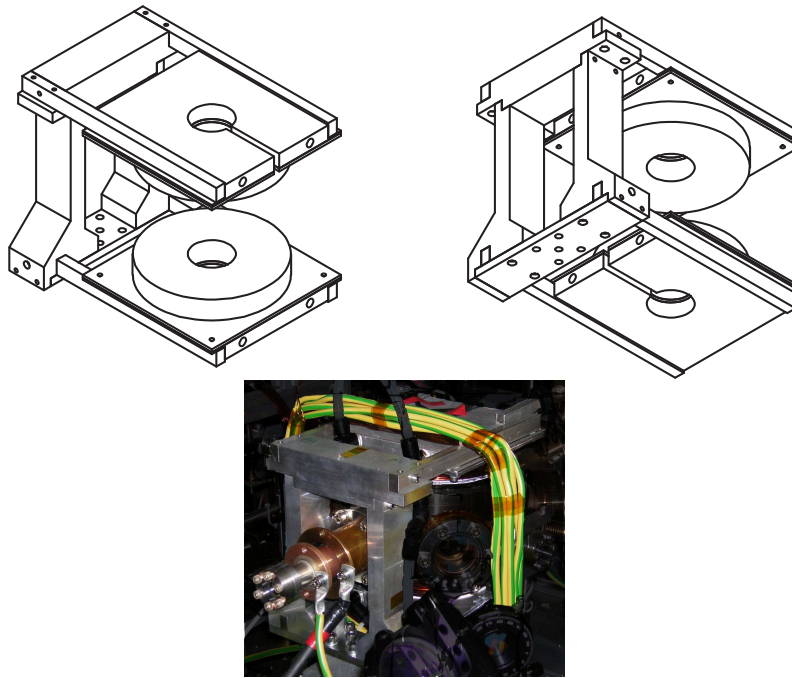


**Figure 2.12.** Scheme and realization of the coil translation stage: the two holes in the heat sink allow the passage of the cooling water, the heat sink is cut to suppress eddy currents. The heat sink is machined out of normal commercial aluminum alloy while the frame is build in Ergal. The four bars are made out of stainless steel.

### **Magnetic translation stage**

The coils are glued onto an aluminum heat sink which is connected to a pair of stainless steel bars. The bars are in turn fastened to a frame which is moved by a mechanical actuator (THK KR series) driven by a brushless motor (Parker SMH82). The whole structure is shown in figure 2.12.

The choice of stainless steel is dictated by the requirements of reducing the size of the device and withstand the magnetic force exerted by one coil on the other. This force is the same but for a sign when the same coils, after switching to the Helmholtz configuration, are used to generate the field to exploit Feshbach resonances (see chapter 7). The total weight of each of the two coils is about 16 N and the magnetic force at 100 A is almost double around 30 N: this means that when the two coils attract each other the lower bar feels an upward force of about 14 N and the upper one a downward force of 46 N while the situation is reversed if the coils repel. This force will bend the two bars and move the center of the magnetic field: the bars must be able to limit this displacement to a reasonable value. With

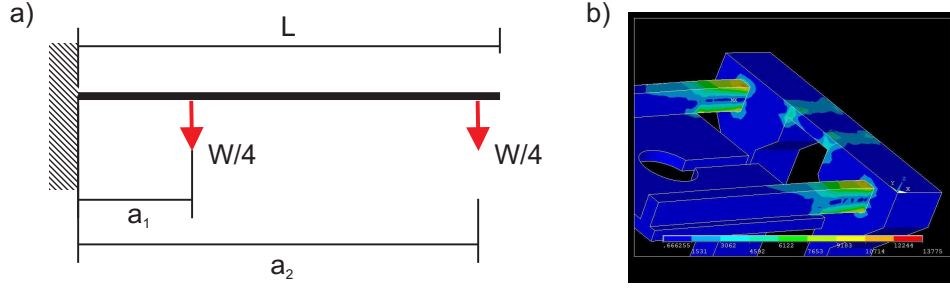


**Figure 2.13.** Geometry of the beam bending problem (a) and snapshot of the results of the finite element simulation of the frame structure under load (b).

the geometry indicated in figure 2.13, for a beam of length  $L$  with constant cross section, the bending induced by a load  $F$  applied at a distance  $a$  from a fixed end is given by

$$\Delta z = \frac{F a^2}{6EI} (3L - a), \quad (2.9)$$

where  $E$  is the Young's modulus of the material and  $I$  is the moment of inertia of the cross section. For a rectangular cross section with dimension  $h$  in the direction of the load and  $b$  in the other direction we have:  $I = h^3 b / 12$ . If we now consider the load equally distributed between the two screws of each bar every screw will have a load  $F = W/4$ . Assuming a linear response, we can sum up the two contributions:

$$\Delta z = \frac{W}{24EI} (a_1^2 (3L - a_1) + a_2^2 (3L - a_2)).$$

Taking  $W$  the one indicated above,  $E = 195$  GPa for stainless steel<sup>3</sup>,  $L = 190$  mm,  $a_1 = 40$  mm,  $a_2 = 180$  mm,  $h = 15$  mm and  $b = 10$  mm we obtain that, when the two coils repel each other the upper coil is bent upward by  $14 \mu\text{m}$  and the lower is bent down by  $47 \mu\text{m}$ . As a result the center of the magnetic field moves by less than  $15 \mu\text{m}$  which is acceptable.

The results of this simple model were validated by a finite element simulation of the whole structure: this allowed us not only to confirm the above calculation (within 10%), but also to calculate the stress that the bar will transmit to the Ergal frame. For twice the expected load the maximum stress, which occurs near the edge of the bars in the bottom part of the frame (see figure 2.13(b)), is about 14 MPa, way below the tensile yield strength of this material which is around 500 MPa. Furthermore we calculated that the lowest lying vibrational mode of the bars is around 300 Hz

<sup>3</sup>We used non magnetic AISI304 steel.

and other extra modes are absent between 500 Hz and roughly 1 kHz: this is highly desirable to avoid parametric heating of the atoms during the transfer. The total weight of the frame with the coils and the water cooling is below 80 N which is largely in the operating range of the selected actuator.

The target speed of the motion is less than 0.2 m/s and it can be accepted to reach it in more than 3 ms: this allows us to calculate the maximum torque required for the acceleration as 2.8 Nm [66]. This is again safely below the maximum torque of our motor which is 5 Nm.

### **Typical transfer sequence**

During a typical experimental run the current in the quadrupole is ramped in 500 ms up to 65 A corresponding to a gradient in the horizontal plane of about 130 G/cm. This compression raises the temperature of the atoms slightly below 1.1 mK which is not much smaller than the initial trap depth. This value of the final current is however necessary to have the atomic cloud pass into the small aperture of our millimetric trap. Once the compression is almost finished the translation stage moves the atoms to the center of the magnetic trap in 500 ms: the motion is obtained with a positive constant acceleration and a final constant deceleration. As we pointed out above the acceleration could take no more than a few ms but in practice the abrupt profile of the applied jerk<sup>4</sup> limits this acceleration to a few tens of ms in order to preserve the locking of the servo which controls the motion. Limited losses and heating were observed in the atomic sample during the transport: the number of atoms after a round trip is about 80%. Once the translation stage is turned off the magnetic trap is turned on in about 150 ms to a peak current of 105 A and, when the current is stabilized ( $\sim 300$  ms after turn on), the quadrupole is turned off in about 300 ms leaving the atoms in the harmonic trap. The overall efficiency of the transfer process from the MOT to the magnetic trap is about 20% corresponding to  $3 \times 10^8$  <sup>87</sup>Rb atoms loaded at the beginning of the evaporation.

## **2.4 Evaporation and hyperfine transfer**

The key technique which allows to reach the degenerate regime in our sample is evaporative cooling [61]. This technique amounts to selectively re-

---

<sup>4</sup>For the reader unfamiliar with engineering slang this is the name for the derivative of the acceleration.

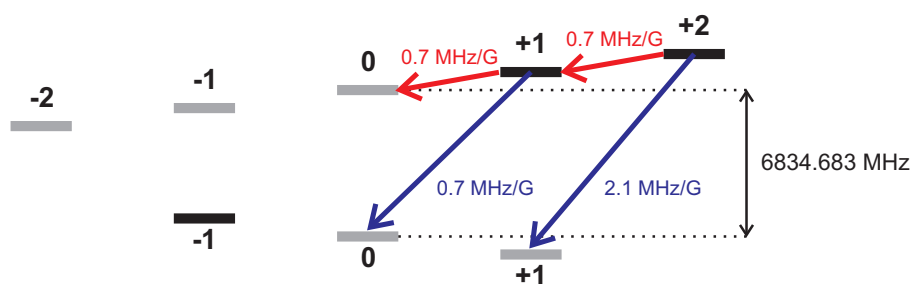


**Figure 2.14.** Simplified scheme of the hyperfine structure in a magnetic field of  $^{87}\text{Rb}$ . The number beside the lines is the Zeeman shift of the corresponding transition. Black lines are low-field seeking levels, gray lines are high-field seeking.

move the hottest atoms from the trap thereby removing energy from the system and let the remaining atoms thermalize at a lower temperature through elastic collisions. Repeating this process at a progressively lower energy, the temperature can be significantly reduced. Eventually if the initial number of atoms is high enough one can reach the so called *run-away evaporation* regime in which the phase space is greatly increased in a short amount of time because the gain due to the lower temperature leads also to an increase in the elastic collision rate in spite of the reduction in the number of atoms. I shall not review the theoretical foundation of this technique: the interested reader can find them in the above mentioned reference.

In practice, the way to selectively address the high energy atoms follows from a simple classical consideration: the higher the energy of a particle the farther its turning point from the trap center. Therefore the higher energy atoms, due to the inhomogeneous magnetic field of the trap, spend most of their time where the Zeeman shift of the transition is bigger than those of the low energy ones. The removal of these atoms from the magnetic trap is then easily obtained exciting a transition from the trapped state to a high-field seeking state. In many experiments the transition of choice is the simple radio-frequency cascade illustrated by the red arrows in figure 2.14: in this case the separation between the levels depends only on the bias of the magnetic trap and it is therefore in the range of a few MHz.

In our experiment however, this approach is not useful because  $^{87}\text{Rb}$  has the same quantum numbers as  $^{39}\text{K}$  and  $^{41}\text{K}$  and therefore the evaporation would act also on potassium: this is not convenient since, as we will see in chapter 3, the elastic cross section for these atoms is rather small and elastic collisions do not allow thermalization in a time compat-

ible with the lifetime of the sample in the magnetic trap which is about 60 s. As we will see in § 4.1 and § 6.1, the simplest way to cool both potassium isotopes is to cool  $^{87}\text{Rb}$  and let interspecies elastic collision have the potassium sample equilibrate with it. This requires an evaporation process which acts only on the  $^{87}\text{Rb}$  atoms. The solution is to drive the microwave transition  $|2, 2\rangle \rightarrow |1, 1\rangle$  which, owing to the big difference in the hyperfine splitting (see figures 1.1 and 1.2), has a very different frequency for the three species.

A typical ramp for the evaporation is shown in figure 2.15: the ramp is piecewise linear and the overall shape is roughly exponential. The first part of the ramp is optimized maximizing the peak density of the cloud which is the experimental signature of the run-away regime, while the last part, which is shown in detail in the inset of figure 2.15, is optimized maximizing the number of atoms in the  $^{87}\text{Rb}$  condensate. A frequency step is made every 40 ms and the total ramp duration is around 20 s. The frequency span is about 100 MHz which means that evaporation begins outcoupling from the traps atoms with an energy of 5 mK. By pursuing the evaporation up to the point in which no more atoms are present in the trap one can measure the bias field of the magnetic trap since the resonance frequency at which the atoms at the center of the trap are outcoupled is given by<sup>5</sup>

$$\nu_B \simeq \nu_0 + 2.10 \text{ (MHz/G)} B_0,$$

where  $\nu_0$  is the hyperfine separation of  $^{87}\text{Rb}$ . The frequency for the evaporation is synthesized by a HP E8257D and amplified to a 40 dBm level (10 W) with a narrowband amplifier. The output of the amplifier is fed into a horn antenna in order to maximize the irradiated power.

A figure of merit of the evaporation process can be obtained by measuring the phase space density of the sample as the evaporation proceeds. The phase space density of a harmonic trap is given by [67]

$$n_{PS} = N \left( \frac{\hbar}{k_B T} \right)^3 \omega_{\perp}^2 \omega_z : \quad (2.10)$$

by comparing this expression with the definition of the critical temperature Eq. (1.23) we see that when  $T = T_C$ ,  $n_{PS} = \zeta(3)$ : Bose-Einstein condensation therefore occurs when the phase space density approach one. As we see if one trades off one order of magnitude in the number of atoms for a gain of one order of magnitude in the temperature the overall gain in the

---

<sup>5</sup>See Eq. (7.2) for a more accurate estimation.

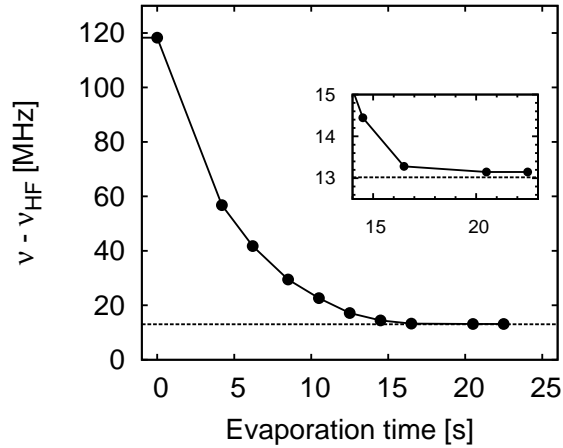


**Figure 2.15.** Plot of the evaporation ramp:  $\nu_{HF}$  is the ground state hyperfine separation of  $^{87}\text{Rb}$  and the dashed line corresponds to  $B_0 = 6.2\text{ G}$ . Note that the ramp is exponential at the beginning and becomes linear in the final part.

phase space density is two order of magnitude: we will call this parameter efficiency of the evaporation

$$G_e = -\frac{\Delta \log(n_{PS})}{\Delta \log N}.$$

In the condition outlined above, which corresponds to the onset of the run-away regime,  $G_e = 2$ .

One of our measurements of the phase density during the final part of the  $^{87}\text{Rb}$  evaporation ramp is reported in figure 2.16: from the slope of the dashed line we obtain  $G_e \sim 2.6$ . This value therefore shows that our evaporation is better than the simple run-away condition. As one can see the upper point has a phase space density already above 1: a Bose-Einstein condensate was formed<sup>6</sup>. With only a  $^{87}\text{Rb}$  sample the critical temperature is crossed at about 250 nK with around  $1.5 \times 10^4$  atoms in the condensate.

## 2.5 Detection procedure

Once the desired atomic species are prepared into the magnetic trap, evaporated to the desired temperature and further experiment are done, the density distribution is measured with an absorption image technique. In this technique the samples are illuminated with a beam of resonant light and the absorption profile is recorded onto a CCD.

<sup>6</sup>In this case  $n_{PS}$  is measured from the non-condensed fraction (see 2.5)

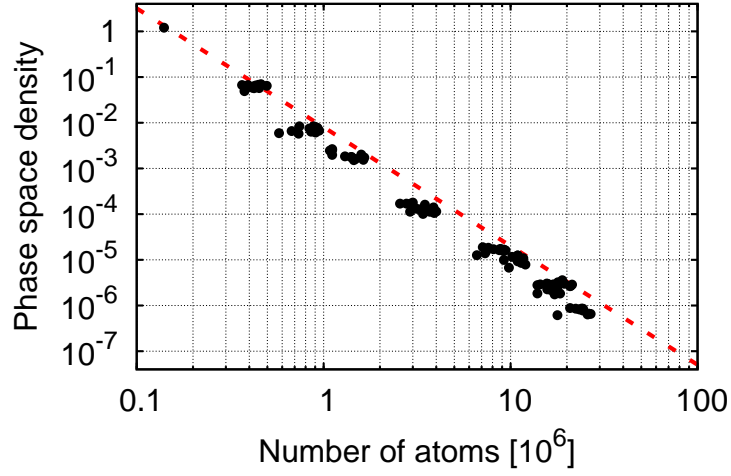


**Figure 2.16.** Plot of the measured phase density as a function of the number of atoms during the evaporation. Only  $^{87}\text{Rb}$  is present in the magnetic trap for these measurement. Each group of points corresponds to different ramp segment and each point corresponds to different parameters: the optimal trajectory in phase space is given by the rightmost point of each group.

The cross section for the absorption of resonant photons by an atom is  $\sigma_a = 3\lambda_0^2/(2\pi)$  and on resonance the transmitted intensity follows the Beer law [68]:

$$I_T(x, y) = I_0(x, y) \exp\left(-\sigma_a \int dz n(\mathbf{r})\right),$$

where  $I_0(x, y)$  is the intensity profile of the beam in the absence of atoms and  $n$  is simply the atomic density distribution. From the above expression it follows immediately that the density of the cloud integrated along the imaging direction can be measured as<sup>7</sup>

$$n(x, y) = -\frac{1}{\sigma_a} \ln\left(\frac{I_T(x, y)}{I_0(x, y)}\right). \quad (2.11)$$

This technique has a very good signal to noise ratio and can detect up to a few hundred atoms, however it is destructive in character: after taking a picture a new sample has to be prepared.

<sup>7</sup>To keep the notation simple I do not distinguish between the density distribution and its integral along the imaging direction (column density): the distinction will be clear from the arguments of the function.

### 2.5.1 Hardware setup

In our experiment two separate probe beams exist: these two beams come respectively along the vertical direction and on the axial direction and arrive on different regions of the CCD array. This double imaging is crucial if one wants to access the density distribution along all the three directions.

The optical scheme is the following: the output of a dedicated fiber is split and the two beams are directed on the center of the magnetic trap: the shadow cast by the atoms is then collected by an acromat lens which sets the numerical aperture of the system and fixes the diffraction limit in  $15\ \mu\text{m}$  along the axial direction and  $8\ \mu\text{m}$  along the vertical direction. The light is almost collimated and sent onto another lens which focuses the shadow image onto the CCD: the resulting magnification, which is calibrated by imaging the edges of the magnetic trap, is 2 in the axial direction and 2.5 in the vertical one. Typical exposures time are  $50\ \mu\text{s}$  for each of the two species.

The CCD camera is a Theta System SIS1-s285 equipped with the sensor Sony ICX285AL. The size of the sensor is  $1040 \times 1392$  pixels, and pixels are square of  $6.45\ \mu\text{m}$  of side. The acquisition software can operate the array in the so-called frame transfer mode: the first picture is stored in a dark region so that the array can be exposed again within less than  $1\ \mu\text{s}$ . After the exposure of this second frame the two frames are transferred and processed by the ADC in 600 ms. After this time another pair of frames can be acquired. This is used in our experiment to take two almost simultaneous images of the two species: the first frame has the absorption profile of K and the second that of  $^{87}\text{Rb}$ . Although, as indicated in Eq. (2.11) only two pictures are needed to reconstruct the integrated density profile, we acquire normally three pictures: the first records  $I_T(x, y)$ , the second  $I_0(x, y)$  and in the third the CCD is exposed only to background light. The third image is subtracted from each of the other two before processing them according to Eq. (2.11). To suppress the effect of ambient light and to protect the detector from the lattice light (see § 6.2.1) a bandpass filter and a mechanical shutter are placed in front of the CCD.

### 2.5.2 Data analysis

The best example of the kind of images that one obtains from the experiment is shown in figure 2.17 where we show three pictures taken respectively well above, close to and below the critical temperature. Quantitative

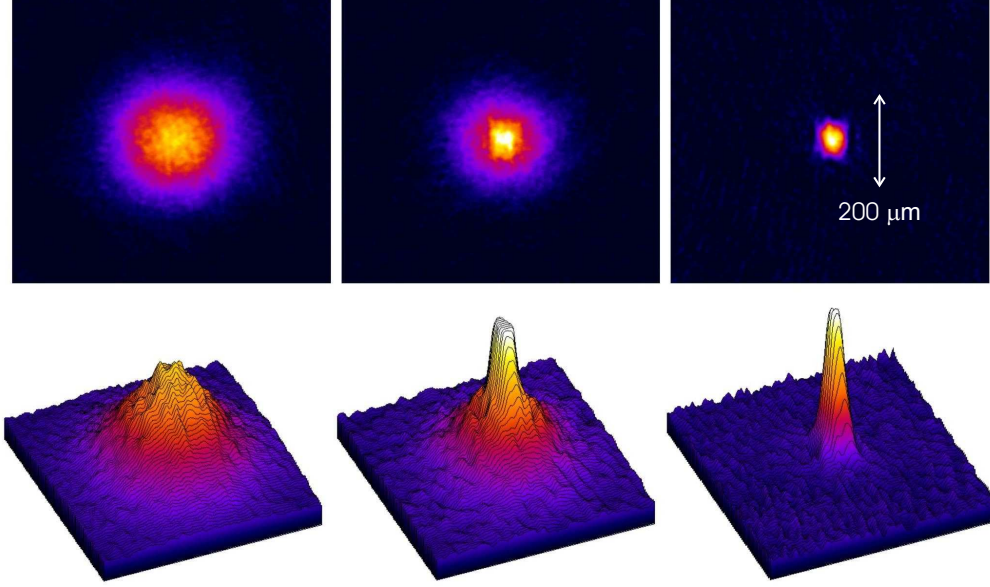


**Figure 2.17.** Absorption image showing the transition from a thermal cloud ( $T > T_c$ ) with its characteristic Gaussian shape (left), a mixed cloud ( $T \lesssim T_c$ ) (center) and an almost pure Bose-Einstein condensate ( $T \ll T_c$ ) (right). All images are taken after 15 ms of expansion; the typical number of atoms in the condensate is  $10^5$  which sets a critical temperature of about 200 nK.

information from these pictures can be extracted with a two-dimensional fit. Above the critical temperature the density profile of the harmonically trapped cloud is Gaussian and the corresponding fit function is

$$n_G(x, y) = A \exp\left(-\frac{(x - x_0)^2}{2\sigma_x^2} - \frac{(y - y_0)^2}{2\sigma_y^2}\right) + B. \quad (2.12)$$

The width of the cloud is simply related to the temperature by the equipartition theorem

$$T = \frac{m}{k_B} \omega_i^2 \sigma_i^2, \quad (2.13)$$

while from the normalization of the density one obtains that

$$N = \frac{1}{2\pi} A \sigma_x \sigma_y. \quad (2.14)$$

If the sample is instead well below the critical temperature we know from 1.30 that the density profile in the Thomas-Fermi regime is an inverted parabola: integrating it along one direction one obtains that the proper fit function has the form

$$n_{TF}(x, y) = A \left(1 - \frac{(x - x_0)^2}{2R_x^2} - \frac{(y - y_0)^2}{2R_y^2}\right)^{3/2} + B. \quad (2.15)$$

Similar to the Gaussian case we have that the number of atoms is given by

$$N = \frac{16}{3}\pi A R_x R_y \quad (2.16)$$

and from the radius we can readily obtain the chemical potential as

$$\mu = \frac{1}{2}m\omega_i^2 R_i^2. \quad (2.17)$$

Finally, when the temperature is only slightly sub-critical, the density is well reproduced by a bimodal distribution given by the sum of Eq. (2.12) and Eq. (2.15).

Operatively the initial guesses for the fitting procedure are determined by two unidimensional fits on the distributions obtained by averaging each direction: in both cases the width ( $\sigma$  or  $R$ ) is not changed by the integration while in general the amplitude is. A simple calculation yields that, setting  $a_x$ ,  $a_y$ ,  $w_x$ ,  $w_y$ ,  $b_x$  and  $b_y$  the results of the two unidimensional fit the correct estimation of the amplitude for the two-dimensional fit is given by:

$$A_{\text{guess}} = \alpha \sqrt{M \frac{a_x a_y}{w_x w_y}} \quad (2.18)$$

where  $M$  is the total number of point in the image and the constant  $\alpha$  for a Gaussian (Thomas-Fermi) distribution is given by  $1/\sqrt{2\pi} (8/(3\pi))$ . Similar one has that

$$B_{\text{guess}} = \frac{1}{2} \left( \frac{b_x}{W} + \frac{b_y}{H} \right) \quad (2.19)$$

where  $H$  ( $W$ ) is the height (width) of the image. The initial guesses for the two unidimensional fits are obtained by taking for the center and width respectively the first and second moment of the distribution and for the amplitude and background the maximum and minimum.

We conclude this section by mentioning that, especially for a Bose-Einstein condensate, the observation of the system in the magnetic trap is simply impossible due to insufficient spatial resolution and high density of the sample. For this reason the most used technique is to image the clouds after some ms of ballistic expansion. It can be shown that for a Gaussian the only effect is to slightly modify the relation between the observed width and the temperature:

$$T = \frac{m}{k_B} \frac{\omega_i^2}{1 + \omega_i^2 t_e^2} \sigma_{e,i}^2 \simeq \frac{m}{k_B} \frac{\sigma_{e,i}^2}{t_e^2}, \quad (2.20)$$

where  $t_e$  is the expansion time,  $\sigma_{e,i}$  is the width measured after expansion and the last approximation requires  $\omega_i^2 t_e^2 \gg 1$ . This approximation can be useful when the exact frequency is known with poor precision.

More surprisingly, a similar scaling behavior is valid also for a Bose-Einstein condensate in an elongated cylindrical trap in the Thomas-Fermi regime [42]. One finds that the correct fit function is still Eq. (2.15) and the expanded radii are related to the one in trap by the following relations [69]

$$R_{\perp}(t) = R_{\perp}(0) \sqrt{1 + \tau^2} \quad (2.21)$$

$$R_{\parallel}(t) = R_{\parallel}(0) (1 + \mathcal{A}_R^{-2}) (\tau \arctan(\tau) - \ln \sqrt{1 + \tau^2}), \quad (2.22)$$

where we have set  $\tau = \omega_{\perp} t$ . One important well known consequence of Eq. (2.21) is that, opposite to what happens for a thermal gas, there is a moment in which the aspect ratio of an expanding condensate inverts: a prolate condensate becomes oblate after a sufficiently long expansion and vice-versa.

## **Part II**

# **Experiment with $^{39}\text{K}$**



# Introduction

Beside being the most abundant isotope of potassium,  $^{39}\text{K}$  is a very interesting atom. As it was early recognized its intraspecies interaction is attractive and therefore cannot support a large and stable Bose-Einstein condensate. For this reason this isotope was never trapped in a magnetic trap and sympathetic cooling was only applied to  $^{41}\text{K}$ : beside this, due to the small elastic cross section of the  $^{87}\text{Rb}$ - $^{39}\text{K}$  mixture, it was not even sure that sympathetic cooling between these two species could work at all.

During the initial part of my thesis we were very interested by the perspective of using this isotope purposely for exploring the field of attractive condensates. For this reason we first demonstrated that sympathetic cooling with  $^{87}\text{Rb}$  is possible also for this isotope and then we made the first direct collisional measurement on this isotope. Both these results are described in detail in chapter 4. However at the same time a theoretical work aimed at establishing the possibility to use the repulsion between  $^{87}\text{Rb}$  and  $^{39}\text{K}$  to stabilize the latter showed that, although the effect indeed exists it is too small and stable attractive condensates cannot be formed only with less than  $2 \times 10^3$  atoms, a quantity that is barely detectable by our imaging system [70]. Once this fact was established, the only viable alternative to operate with this isotope was to exploit the Feshbach resonances that were recently predicted by our group [71, 72]. However, as I outlined in the Introduction, the main goal of our experimental apparatus is in loading two different Bose-Einstein condensates into a 3D optical lattice. For this reason it seemed much more sensible to shift to  $^{41}\text{K}$ , for which a Bose-Einstein condensate was already realized [16]. These results are presented in part III.

I must say that indeed our experimental work sparked a renewed interest for  $^{39}\text{K}$ . This interest was made more concrete by another experiment of our group which is devoted to Feshbach spectroscopy and atom interferometry. Motivated by our work and taking advantage of the accumulated

know-how, they could create a Bose-Einstein condensate of  $^{39}\text{K}$  by exploiting both inter- and intraspecies Feshbach resonances [73]. With this work all the stable isotopes were brought to quantum degeneracy.

This part consists of two chapters. In the first chapter I will introduce the issue of cold collisions between atoms introducing the tools that I will use to analyze the data obtained in the experiments presented in chapter 4.

## Chapter 3

# Cold collisions

When you are solving a problem, don't worry. Now, after you have solved the problem, then that's the time to worry.

(R. Feynman)

This chapter treats two very important topics in the current panorama of the physics of ultracold atoms. The first is that of  $s$ -wave scattering in atoms: in § 3.1, I will very briefly review the fundamental elements of scattering theory needed to make use of the scattering length concept. Then I will introduce the so-called effective range approximation which is suitable to treat ultracold collisions beyond the zero temperature limit. The second topic is that of Feshbach resonances: I will show how, due to the short-range, spin-dependent interactions between the outer electrons of two colliding atoms, under suitable conditions, the scattering length becomes strongly dependent on an external uniform magnetic field. The existence of these resonances plays a crucial role in several actual experiment, as I pointed out in the Introduction.

### 3.1 $s$ -wave scattering in atoms

The aim of this section is to justify the expression used to take into account atomic interactions in § 1.2. I will not review the details of the calculation which can be found for instance in [74], but I will recall the important results which will be extensively used in the following sections.

Neglecting for the moment relativistic effects, the problem of scattering of two particles can be brought back to that of a single particle with the reduced mass  $m_R$  in a central potential  $U(r)$ . Taking as  $z$  the direction of

the relative motion and  $\hbar k$  the relative momentum, it is possible to expand the particle wave function into a sum of an incoming plane wave and a modulated outgoing spherical wave centered in the center of mass of the system:

$$\psi \simeq e^{ikz} + f(k, \theta) \frac{e^{ikr}}{r}. \quad (3.1)$$

Here  $\theta$  is the angle between  $e_z$  and  $e_r$  and the function  $f(k, \theta)$  is called *scattering amplitude*.

Given the symmetry of the problem it is customary to carry out an expansion of the scattering amplitude in eigenfunctions of the angular momentum:

$$\psi = \sum_l A_l P_l(\cos \theta) R_{kl}(r). \quad (3.2)$$

The radial functions obey the following 1D Schrödinger equation:

$$u_{kl}''(r) + \left( k^2 - \frac{l(l+1)}{r^2} - \frac{2m_R}{\hbar^2} U(r) \right) u_{kl} = 0, \quad (3.3)$$

where we have defined  $u_{kl} = r R(r)$ .

From Eq. (3.2) one obtains the following partial wave expansion for  $f$

$$f(k, \theta) = \frac{1}{2ik} \sum_l (2l+1) (e^{2i\delta_l} - 1) P_l(\cos \theta) = \sum_l (2l+1) f_l P_l(\cos \theta), \quad (3.4)$$

where  $\delta_l$  are the phase shift of  $R_{kl}$  with respect to a simple spherical wave. The value of these phase shifts depends on the actual shape of the potential.

However, in the limit of low energy<sup>1</sup>, the scattering for  $l \neq 0$  will be dominated by the centrifugal barrier and in this case one can show that [74, § 131]

$$f_l \sim k^{2l},$$

this means that in the limit  $k \rightarrow 0$  only the  $s$ -wave contributes to the scattering<sup>2</sup>.

In this limit 3.4 becomes

$$f(k, \theta) = \frac{1}{2ik} (e^{2i\delta_0} - 1) \simeq \frac{1}{k (\cot \delta_0 - i)}, \quad (3.5)$$

<sup>1</sup> $k\ell \ll 1$ , where  $\ell$  is the characteristic length scale of the potential.

<sup>2</sup>For a potential of the form  $r^{-n}$ , the argument remains valid, but the given asymptotic behavior holds only for  $2l+3 < n$  [75].

and, although the phase shift  $\delta_0$  still depends on the detail of the potential, the cross section can be simply written as

$$\lim_{k \rightarrow 0} \sigma_0(k) = 4p\pi a^2 \quad (3.6)$$

where  $a$  is the so called *scattering length* formally defined as

$$a = - \lim_{k \rightarrow 0} \frac{\tan \delta_0(k)}{k} \quad (3.7)$$

and  $p$  is equal 1 if the particles are distinguishable and 2 if they are identical bosons<sup>3</sup>.

The cross section Eq. (3.6) is equivalent to that given by a pseudopotential such that [76, 75]

$$V(r)\psi(r) = g\delta(r)\frac{\partial}{\partial r}(r\psi(r)), \quad (3.8)$$

where  $g$  is given by

$$g = \frac{2p\pi\hbar^2}{2m_R} a. \quad (3.9)$$

Note that for a function  $\psi$  regular in  $r = 0$  as the one describing the solution of a Gross-Pitaevskii equation the pseudopotential can be written as

$$V(r - r') = g\delta(r - r')$$

which is the form used in § 1.2.

As we pointed out in the beginning, considering the interaction potential as a central one is valid if we neglect relativistic effects which arises because of the atomic spin. We postpone considerations about these effects to § 3.2, here we shall only remind that, even neglecting relativistic effects, the actual interaction potential between the two atoms depends on the total electronic spin of the atomic pair,  $S = 1/2 \oplus 1/2$ . One should therefore distinguish between two different scattering lengths: one belonging to the triplet potential ( $S = 1$ ) and one belonging to the singlet one ( $S = 0$ ). The difference between the two is seen only at short distance and we will analyze this point in § 3.2: for the present analysis it is worth noting that, all the experiments reported in this work, but those presented in chapter 7, are performed with atoms in the  $|F = 2, m_F = +2\rangle$  state. For this state one has  $S = 1$  and the two atoms interact only through the triplet potential so that the formalism developed so far is still meaningful.

---

<sup>3</sup>In the case of identical spinless fermions the *s*-wave scattering is suppressed on symmetry ground.

### 3.1.1 Zero energy scattering

The interaction between two neutral atoms at large separation is of the van der Waals type:  $U(r \rightarrow \infty) = -C_6 r^{-6}$ , while at very short distances the Coulomb repulsion will dominate. Following [77, 75, 78] we will use a truncated van der Waals potential

$$U(r) = \begin{cases} -C_6 r^{-6} & \text{if } r > r_c \\ \infty & \text{if } r \leq r_c \end{cases} . \quad (3.10)$$

This potential depends on two parameters: the  $C_6$  coefficient and the cutoff of the hard core  $r_c$  which corresponds to the position of the minimum of the potential that we expect to be on the order of the atom size. The  $C_6$  coefficient can be calculated *ab initio* for the alkali atoms with very high accuracy and the calculations can be tested against data from molecular spectroscopy. From this coefficient it is possible to build a length scale

$$a_6 = \left( \frac{2m_R C_6}{\hbar^2} \right)^{1/4} \quad (3.11)$$

which, owing to the easy polarizability of the alkali atoms, is much bigger than  $r_c$ . It can be shown that this condition allows for the application of a semiclassical approximation which simplifies the solution of the radial Schrödinger equation [77]. Once Eq. (3.3) is solved, the scattering length can be extracted from the asymptotic behavior  $u \sim (f_0 - r)$ . Remembering that, within our approximation,  $f_0 = a$ , one finds that [77]

$$a = \bar{a} (1 - \tan(\Phi)) , \quad (3.12)$$

where  $\bar{a}$  is proportional to  $a_6$

$$\bar{a} = 0.478 a_6 \quad (3.13)$$

and the phase  $\Phi$  depends on the minimum position  $r_c$

$$\Phi = \frac{a_6^2}{2r_c^2} - \frac{3\pi}{8} . \quad (3.14)$$

The scattering length given by equation Eq. (3.12) is plot in figure 3.1. As we can see, the scattering length has a divergence for  $\Phi = n\pi$  and each divergence corresponds to the appearance of a new bound state. The semiclassical approximation used to solve the Schrödinger problem can be restated as the requirement that the potential supports a high number of bound state.

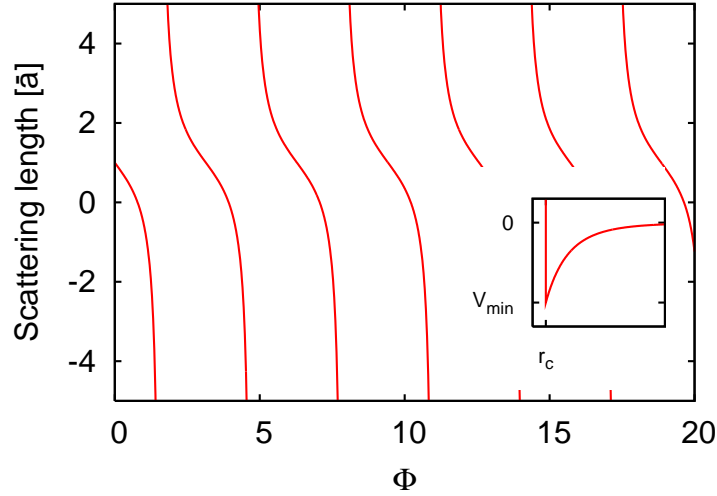


**Figure 3.1.** Scattering length of the truncated  $C_6$  potential as a function of the parameter  $\Phi$ .

The prediction of Eq. (3.12) has two important consequences. The first is that, assuming no knowledge on the short range cutoff, and therefore taking  $\Phi$  uniformly distributed in  $[0, \pi]$ , one obtains that the cross section of atom-atom scattering in alkali elements should be positive in 75% of cases [77, 78]. The second is that, if a bound state is far from threshold,  $\Phi \sim 0$  and therefore the scattering length is on the order of  $\bar{a}$ . The actual value for the triplet scattering lengths, the  $C_6$  coefficients and the value of  $\bar{a}$  for all the alkali atom combinations relevant to this work are reported in table 3.1. As we can see four out of five scattering lengths are positive and indeed  $\bar{a}$  provides the good order of magnitude for the scattering length with the remarkable agreement in the case of  $^{41}\text{K}$ - $^{41}\text{K}$ . However, we see also that in the case of  $^{39}\text{K}$ - $^{39}\text{K}$  the model fails to predict the sign of the scattering length and in the case of both  $^{87}\text{Rb}$ - $^{39}\text{K}$  and  $^{87}\text{Rb}$ - $^{41}\text{K}$  the results are wrong by a factor two. This means that for these mixtures a bound state (a virtual one in the case of  $^{39}\text{K}$ - $^{39}\text{K}$ ) lays near the  $k = 0$  energy threshold. We will see that Feshbach spectroscopy is the ideal tool to probe the position of this level and therefore establish the details of the interaction potential.

It is worth remarking that the  $C_6$  coefficient represents only the long range part of the actual potential: this means that not only it is not sensitive to the isotopic shift (see table 3.1), but it cannot distinguish between triplet and singlet scattering. Also these distinctions can be made measuring the position of Feshbach resonances as we will see in § 3.2.

	$C_6$	$\bar{a}$	$a$ (exp.)	Ref.
$^{87}\text{Rb}-^{87}\text{Rb}$	4691(23)	79	99	[79]
$^{41}\text{K}-^{41}\text{K}$	3897(15)	63	65	[80]
$^{39}\text{K}-^{39}\text{K}$	3927	62	-33	[81, 80, 82, 83]
$^{87}\text{Rb}-^{41}\text{K}$	4274(13)	69	164	[71, 72]
$^{87}\text{Rb}-^{39}\text{K}$	4274(13)	68	36	[71, 72]

**Table 3.1.** Table of the  $C_6$  coefficient and triplet scattering length for all the alkali atoms mixture relevant to this work. All data are in atomic units. All  $C_6$  values are taken from [84], but the one for K-K which is taken from [85]. Reference is given for the experimental values, note that one of the measurement of the scattering length of  $^{39}\text{K}$  is reported in this work (see following chapter).

### 3.1.2 Effective range approximation

The above considerations about the scattering length were carried out in the strict limit  $k = 0$ . If this can be considered a satisfactory result for the physics of Bose-Einstein condensate as described by the Gross-Pitaevskii equation, it is an oversimplification in the case of finite temperature gases.

The finite temperature  $T$  introduces a distribution of relative wavevector  $k$  centered around zero but with a second moment given by

$$k_T = \frac{1}{\hbar} (2m_R k_B T)^{1/2} : \quad (3.15)$$

this means that the dependence of the cross section on the relative wavevector must be taken into account.

A good starting point is to evaluate the energy dependence of the scattering amplitude given by the pseudopotential (3.8). It can be easily shown that the scattering amplitude is given by [75, 74]

$$f_0 = -\frac{1}{1/a + ik}, \quad (3.16)$$

and the corresponding cross section is then

$$\sigma(k) = \frac{4p\pi a^2}{1 + a^2 k^2}. \quad (3.17)$$

The cross section  $\sigma(k_T)$  is plotted in figure 3.2 as a function of temperature. It has the right behavior both in the zero energy and in the so called unitary ( $k \rightarrow \infty$ ) limits, but one cannot expect it to be accurate in the intermediate regime: as the energy is increased, the two colliding atoms experience more

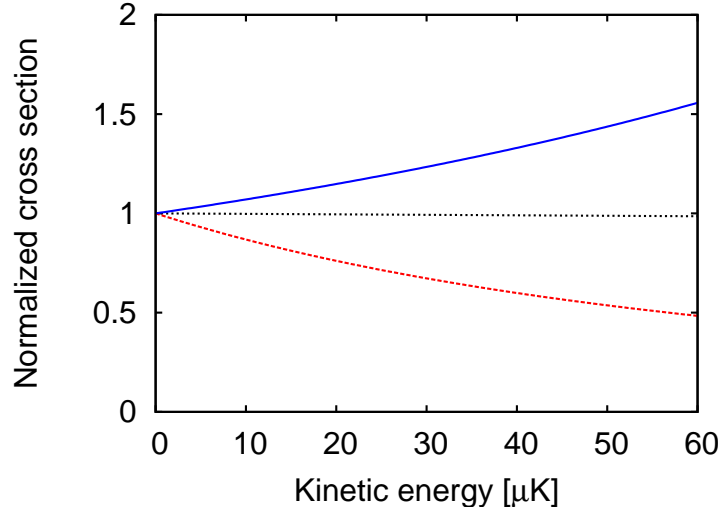


**Figure 3.2.** Plot of the cross section as a function of the kinetic energy of two colliding atoms ( $E = \hbar^2 k_T^2 / (2m_R)$ ). The  $C6$  coefficient is that of  $^{39}\text{K}$  (see table 3.1), while the scattering length is  $-33 a_0$  (red, dashed) or  $+33 a_0$  (blue, solid). The dotted line represents Eq. (3.17) which is insensitive to the sign of  $a$ .

and more the short range part of the potential which is neglected by the pseudopotential approximation.

It can be shown that Eq. (3.17) can be viewed as a zero order approximation of the expansion of the cross section in the limit of small  $k$ . The next order of the expansion is given by the *effective range* approximation in which the scattering amplitude is written as [74]

$$f = -\frac{a}{1 - \frac{1}{2} ar_e k^2 + iak} \quad (3.18)$$

where the coefficient  $r_e$  is the effective range. The corresponding cross section is then given by

$$\sigma(k) = \frac{4\pi a^2}{\left(1 - \frac{1}{2} ar_e k^2\right)^2 + a^2 k^2}. \quad (3.19)$$

For the truncated van der Waals potential the effective range can be calculated explicitly [86]

$$r_e = a_6 \left( 1.39473 - \frac{4}{3} \frac{a_6}{a} + 0.63732 \frac{a_6^2}{a^2} \right), \quad (3.20)$$

where  $a$  is given by 3.12. Taking instead the scattering length as an experimental input, Eq. (3.20) gives explicitly the effective range: this way

one can infer the behavior of the cross section as a function of  $k$  from the zero temperature parameters. The expansion underlying the effective range approximation is legitimate as long as the contribution of the term  $ar_e k^2/2$  is small with respect to 1: this limits the range of validity of this approximation for  $^{39}\text{K}$  to  $T \sim 100 \mu\text{K}$ .

This cross section is also plot in figure 3.2: as one can see, the  $k$  dependence is much bigger if one includes the effective range and furthermore this term introduces a difference between positive and negative scattering length which is not contained in Eq. (3.17). However, as we will see in § 4.2, this difference is much less pronounced if we include the complete temperature dependence of the collision rate.

### 3.2 Feshbach-resonances

As we pointed out at the end of § 3.1, the interaction between the two atoms depends on the total spin of the atomic pair which, for the alkali atoms can be 0 or 1. The low-lying electronic potentials are therefore characterized by the molecular Born-Oppenheimer potentials  $^1\Sigma_g^+$  and  $^3\Sigma_u^+$  corresponding to the singlet and triplet total spin<sup>4</sup>: the difference between the two is determined by the overlap of two electronic wavefunctions. The scale of this interaction is set by the size of the electronic wavefunction which is typically a few atomic units. This means that the big difference between the two potentials lies below the cut-off  $r_c$  that we used to write Eq. (3.10): a typical plot highlighting the relevant energy and length scales is shown in figure 3.3. From the inset of the figure, which reports the typical shape of a  $C_6$  potential, it should be clear that the electronic interaction has a huge effect albeit at short range. Yet one has to mention that the typical temperature energy scale for cold collisions is much less than 3 MHz which is  $10^{-4}$  on the scale of figure 3.3: this again is at the root of the semiclassical approximation used to obtain Eq. (3.12) and, more generally, it allows us to consider only zero-energy scattering.

At long distance, where the interatomic potential has a negligible effect, the atomic pair is well described by the set of quantum numbers  $\alpha = \{F_1 m_1, F_2 m_2, \ell m_\ell\}$ , where the quantization axis is defined by the external magnetic field, the first two pairs are the atomic state, the last pair

<sup>4</sup>It is worth remembering that the g/u symmetry is meaningless if the two atoms are of different species.

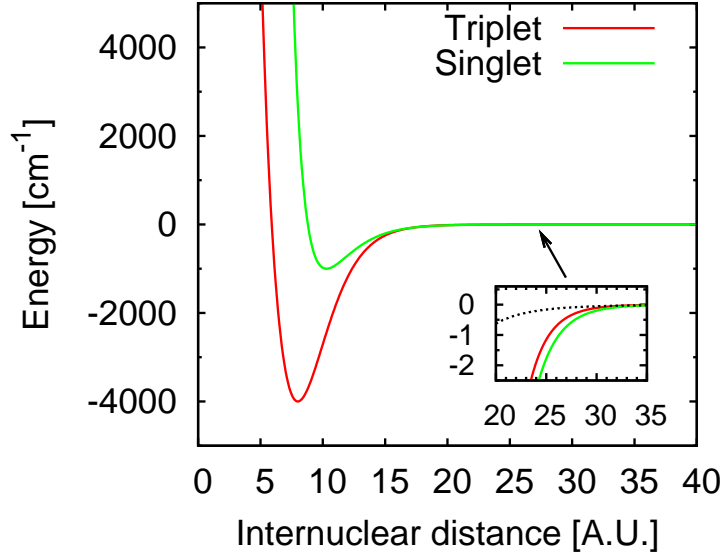


**Figure 3.3.** Plot of the internuclear potential

is the angular momentum of the relative motion and braces are understood to imply symmetrization with respect of identical boson exchange<sup>5</sup>. We refer to the set  $\alpha$  as a scattering channel and we distinguish between open and closed channel based on their asymptotic energy  $E_\alpha$ . The latter is simply the sum of the two atomic energies given by the hyperfine separation plus the Zeemann shift.

Unless, as we assumed in the rest of this chapter, the total spin of the atomic pair is fixed as for the  $\{22, 22, \ell m_\ell\}$  channels, the interatomic potential couples different channels. This coupling is invariant under rotation with respect to the quantization axis and therefore  $m_1 + m_2 + m_\ell$  is conserved; beside this selection rule, the channels are coupled by a tensor potential of the form [87]:

$$V(r) = V_3(r)\hat{P}_3 + V_1(r)\hat{P}_1 + V_{SS}(r) \quad (3.21)$$

where  $V_i(r)$  and  $\hat{P}_i$  indicate respectively the potential and the spin projector operator and  $i = 2S + 1$ . The term  $V_{SS}(r)$  includes relativistic corrections which are dominated by the spin-spin interaction. It is a weak term since it is next order in QED but it is non diagonal also with respect to  $\ell$  and it therefore introduces coupling between different partial waves: it can be shown that it is second order and therefore couples channels with  $\Delta\ell = \pm 2$ .

<sup>5</sup>The notation used in this chapter closely follows that of [87].

$F_K$	$F_{Rb}$	$m_K$	$m_{Rb}$	$E_\alpha/h$ [MHz]	
				$B = 0$	$B = 60G$
1	1	+1	+1	0.0	(-98.97)
2	1	+1	+1	254.01	367.963
2	1	+2	0	254.01	436.949
1	2	+1	+1	6834.68	6918.66
1	2	0	+2	6834.68	6992.37
2	2	+2	0	7088.69	7271.63
2	2	+1	+1	7088.69	7286.62
2	2	0	+2	7088.69	7296.89

**Table 3.2.** Channels coupled to the absolute ground state of the  $^{41}\text{K}$ - $^{87}\text{Rb}$  mixture, neglecting relativistic effects. Magnetic field lifts the degeneracy with respect to  $m$ . The Zeemann shift of the ground state has been subtracted from the energy of the other states.

The most important coupling is therefore between  $s$  and  $d$  waves: this term opens several channels for dipolar relaxation [87]. However, if one considers the absolute ground state of the atomic pair that channel is by definition the only one to be open. A scheme of all the channel coupled to the absolute ground state  $\alpha_0 = \{1\,1, 1\,1, s\,0\}$  for the mixture  $^{41}\text{K}$ - $^{87}\text{Rb}$  neglecting  $V_{SS}(r)$  is shown in table 3.2.

Neglecting relativistic effects, Feshbach resonances arise because, due to a difference in the magnetic moment of two coupled channels, changing the magnetic field changes the relative position of the bound and scattering states between the two channels. When the entrance channel is the absolute ground state (and therefore the second channel is closed) the underlying physics can be understood in terms of figure 3.1: a new bound state is pulled in and out of the effective potential seen by the atomic pair and as a consequence the scattering length varies dramatically with the applied magnetic field.

Given the huge number of bound states and of coupled closed channels shown for example in table 3.2, one sees that predicting the number and the position of Feshbach resonances is not an easy task. Around a broad Feshbach resonance the problem can be mapped onto an effective two channels model in which one identifies the open channel as the one populated at infinite atomic separation and a single closed channel to which the bound resonant state belongs [88, 89, 90]. The two channels are then coupled by the appropriate element of Eq. (3.21). Within this ap-

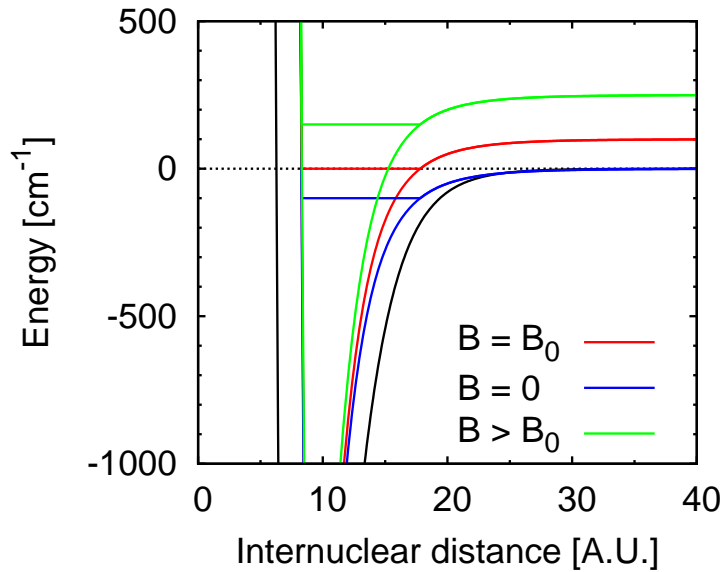


**Figure 3.4.** Schematic representation of a two-channel Feshbach resonance. The dashed line is the threshold energy and the black line is the open channel: the threshold energy is taken as zero for all the magnetic fields. The blue curve is the closed channel potential at zero magnetic field and the horizontal line is the relevant bound state: when the bound state is at the energy threshold (red curve) the field is on resonance, when the state is above threshold (green curve) the scattering length changes sign.

proach one finds that the scattering length depends on the magnetic field as:

$$a(B) = a_{bg} \left( 1 - \frac{\Delta}{B - B_0} \right) \quad (3.22)$$

where  $a_{bg}$  is the background scattering length at  $|B - B_0| \gg \Delta$ ,  $B_0$  is the center of the resonance and  $\Delta$  is the distance between the center and the value of the magnetic field where the scattering length vanishes: this quantity is also called width of the resonance. A schematic representation of the two channel model is done in figure 3.4 where we plot molecular potentials at different values of the magnetic field. For the sake of clarity the energy of the open channel (solid black line) is taken as zero so that it does not change with the magnetic field: the continuous line in the closed channel marks the relevant bound state which can be displaced with respect to the threshold energy by changing the magnetic field.

The two channel model gives an analytic expression for the center and the width of the resonance and, more important, it allows to make simple calculation close to the resonance center: this is of great importance because, as the scattering length diverges, an universal behavior is expected

independent on the resonance details. In particular one finds that in the two-channel approximation the binding energy of the molecular level involved in the resonance is given by [87]:

$$E_b = -\frac{\hbar^2}{m \left( a_{bg} \frac{\Delta}{B-B_0} \right)^2}. \quad (3.23)$$

This expression, in the universal limit  $B \rightarrow B_0$  recovers a fundamental results of scattering for which the size of the bound state is given by the scattering length.

As we will see in chapter 7, the experimental signature of a Feshbach resonance is associated to a drastic increase of three body losses which occur when three atoms collide leading to the formation of a molecule. The molecule then escapes magnetic trapping and the atom, which acquires the molecular binding energy, evaporates from the trap. For this reason one expects a sudden loss of atoms when the magnetic field is tuned close to  $B_0$ .

## Chapter 4

# Collisional properties of $^{39}\text{K}$

A journey of a thousand miles begins with a single step.  
(Lao-tzu)

In this chapter I will present the results obtained during my thesis on the  $^{87}\text{Rb}$ - $^{39}\text{K}$  mixture. As it is shown in table 3.1,  $^{39}\text{K}$  has a negative intraspecies scattering length: this represents a major problem not only for the realization of a Bose-Einstein condensate because of mean field collapse (see § 1.2.2), but also poses a major challenge to the cooling to ultralow temperatures. This is due to the Ramsauer effect which predicts the presence of a zero in the elastic cross section for negative scattering length [74]. This means that, at a certain temperature, the elastic collisions needed for evaporative cooling will be suppressed. In order to overcome this problem the technique widely employed is that of sympathetic cooling [10]: two species are mixed into a trap and evaporation is applied to only one of them; the two species then thermalize owing to interspecies elastic collisions. This technique has indeed allowed the production of a Bose-Einstein condensate of  $^{41}\text{K}$  [16] and the first degenerate Bose-Fermi mixture  $^6\text{Li}$ - $^{23}\text{Na}$  [13], but the scattering length in the case of  $^{39}\text{K}$  is smaller and therefore the process is less efficient.

We will see in § 4.1 that we indeed succeeded in obtaining for the first time the sympathetic cooling of  $^{39}\text{K}$  with  $^{87}\text{Rb}$ . This gave us access to the first ultracold sample of  $^{39}\text{K}$  on which we performed the first direct measurement of the triplet scattering length, which had been previously determined from molecular spectroscopy [80] or through a scaling from data of Feshbach spectroscopy of  $^{40}\text{K}$  [81]. Our results are published in Phys. Rev. A [82] and will be detailed in § 4.2.

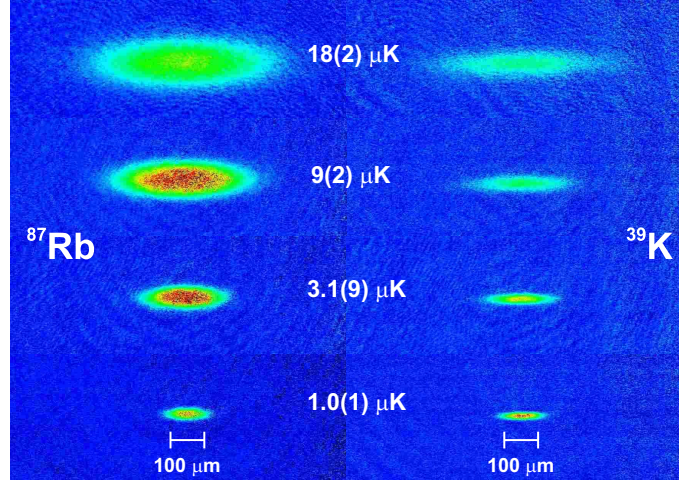


**Figure 4.1.** Experimental sequence showing sympathetic cooling between  $^{87}\text{Rb}$  (left) and  $^{39}\text{K}$  (right). All the images are taken after 1 ms expansion. The phase space density at  $1\ \mu\text{K}$  for  $N_{\text{Rb}} = 3 \times 10^4$  and  $N_{\text{K}} = 2 \times 10^4$  is 0.02 and 0.01 respectively. Images are taken along the vertical radial direction.

#### 4.1 Sympathetic cooling of $^{39}\text{K}$ with $^{87}\text{Rb}$

The striking experimental signal of sympathetic cooling between  $^{87}\text{Rb}$  and  $^{39}\text{K}$  is shown in figure 4.1, where I show a series of pictures taken at different stage of the evaporation of  $^{87}\text{Rb}$ : as we can see the size of the two cloud is the same signaling that they are in thermal equilibrium. This can be deduced from Eq. (2.20) observing that the 1 ms expansion time is here negligible and that  $m_{\text{K}}\omega_{\text{K}}^2 = m_{\text{Rb}}\omega_{\text{Rb}}^2$ , since the two species have the same magnetic moment. If one pushes the cooling process forward it is expected that, as soon as the cloud of  $^{39}\text{K}$  approaches the degeneracy, the system becomes dynamically unstable toward the mean field collapse of the  $^{39}\text{K}$  condensate owing to its negative scattering length. However, our results show that, in spite of the low interspecies cross section of 35.9(7) atomic units [71, 72], the sympathetic cooling can take place. Thermal equilibrium between the two species is established by interspecies collision: the rate of these collisions depends on the density of the two species and on their temperature. In our case the reduced collision cross section is compensated by the high trap frequencies (for  $^{39}\text{K}$ :  $\omega_{\perp} = 2\pi \times 447\ \text{Hz}$ ,  $\omega_z = 2\pi \times 29.4\ \text{Hz}$ ) which increase the density. A careful study of the thermalization dynamics of the two clouds can be done starting from the two coupled Boltzmann equation [91] but is beyond the scope of this thesis.

More qualitatively, one can expect that the two species can reach ther-

mal equilibrium if the heat capacity of the coolant ( $^{87}\text{Rb}$  in our case) is greater than that of the species to cool ( $^{39}\text{K}$ ). For an ideal classical gas  $C = 3N k_B T$  and therefore the necessary condition can be formulated simply as

$$N_{Rb} > N_K.$$

In figure 4.2 we report the measured temperature difference between the two species as a function of the relative atom number: as we can see the temperature difference becomes negligible when  $N_{Rb}/N_K \gtrsim 2.7$ . The qualitative behavior of the data can be understood with a very simple model: energy is removed from the  $^{87}\text{Rb}$  cloud by means of forced evaporation while energy is transferred to it from the hotter  $^{39}\text{K}$  cloud due to interspecies collision. Assuming a dynamical equilibrium between these two processes and indicating with  $W$  the power transfer between the two clouds, from a simple model based on two independent Maxwell-Boltzmann distributions, one finds that [92]

$$W = k_B(T_K - T_{Rb})\Gamma_{12}, \quad (4.1)$$

where  $\Gamma_{12}$  is the interspecies collision rate i.e. the number of interspecies collisions per unit of time. Remembering that  $m_K \bar{\omega}_K^2 = m_{Rb} \bar{\omega}_{Rb}^2 = \kappa$  one has that [92, 91]

$$\Gamma_{12} = \frac{\sigma_{12} N_K N_{Rb}}{\sqrt{8} \pi^2 k_B} \left( \frac{\kappa}{T_{Rb}} \right)^{3/2} \left( \frac{T_{Rb}}{m_{Rb}} + \frac{T_K}{m_K} \right)^{1/2}, \quad (4.2)$$

where we made the rather crude approximations of neglecting the reduced density of the hotter  $^{39}\text{K}$  cloud and also the dependence on temperature of the cross section. Introducing explicitly the temperature difference  $\Delta = T_2 - T_1$  and the ratio in the number of atoms  $x = N_{Rb}/N_K$ , Eq. (4.1) becomes

$$\widetilde{W} = \sqrt{8} \pi^2 \frac{W}{N_1^2} = \sigma_{12} \left( \frac{\kappa}{T_{Rb}} \right)^{3/2} \Delta \left( \frac{T_{Rb}}{m_R} + \frac{\Delta}{m_K} \right)^{1/2} x. \quad (4.3)$$

Although in principle Eq. (4.3) can be explicitly solved to give  $\Delta(x)$  the model is implicitly fit to the data by numerically solving Eq. (4.3) taking  $\widetilde{W}$  as a free parameter and  $T_{Rb} = 20 \mu\text{K}$  as found in the measurements: the result of this procedure is the red curve in figure 4.2. The minimum reduced  $\chi^2$  is about 12, but the agreement is very nice, considering the several approximation present in the model.

No attempt has been made to infer a cross section from the data, given the precision of [71], but instead the known value was used to evaluate  $\Gamma_{12}$  and to guide the optimization of the evaporation. The optimized ramp

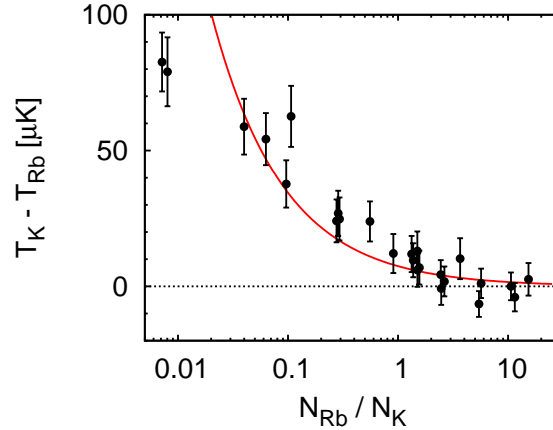


**Figure 4.2.** Temperature difference versus ratio of the atom number of the two species. The ramp length is fixed to 19 s, and the final temperature of  $^{87}\text{Rb}$  is constant around  $20\ \mu\text{K}$ . The solid red line is a fit to a simple model implicitly defined in Eq. (4.3).

shows two changes with respect to the one of  $^{87}\text{Rb}$  alone: the ramp is consistently slowed down in the mid part of the evaporation from  $T \sim 200\ \mu\text{K}$  up to  $T \sim 3\ \mu\text{K}$ . At this point we observed that, in order to maximize the final number of potassium atoms, in the very last part of the evaporation it is better to cool the  $^{87}\text{Rb}$  sample to the desired temperature, keep this temperature by maintaining on the evaporation and let interspecies thermalization follow. As it is shown in figure 4.3, with this technique the temperature of the two samples is always the same within the experimental uncertainty and the number of atoms behave as expected:  $^{87}\text{Rb}$  is lost to the evaporation while the number of  $^{39}\text{K}$  atoms decays slowly only because of collisions with the background gas.

## 4.2 Measurement of the scattering length

As a benchmark of the new apparatus we performed a measurement of the triplet scattering length of  $^{39}\text{K}$ . This determination, although not in a very nice agreement with the successive precise measurement obtained from Feshbach spectroscopy [83], allowed our research team to optimize the apparatus and to obtain several insight on its potential pitfalls. This optimization work had a big impact on the work presented in chapter 6.

We measured the scattering length by analyzing the decay to equilibrium of a non-thermal atomic distribution. This non-thermal distribution

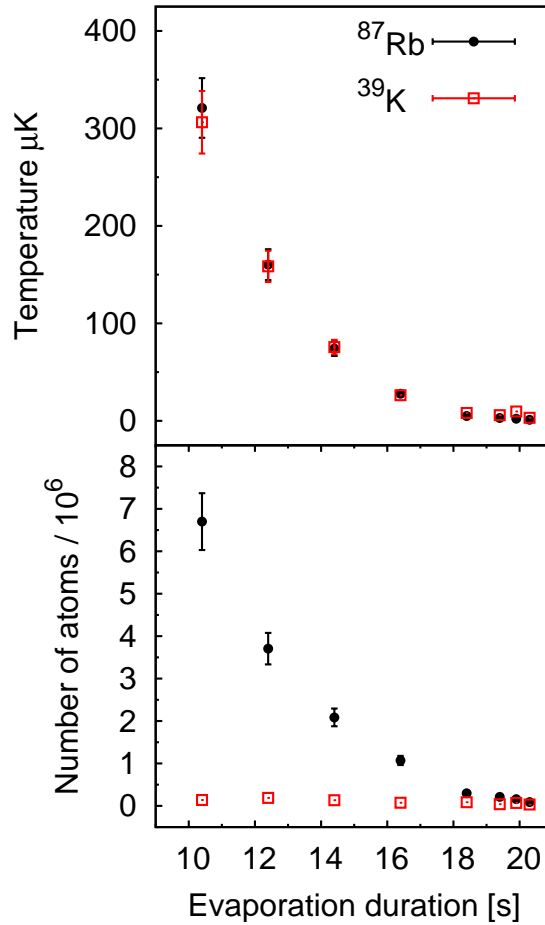


**Figure 4.3.** Number of atoms (top) and temperature (bottom) as a function of the optimized evaporation time for the two species. Where not shown error bars are smaller than point size.

was prepared by exciting selectively only the radial degrees of freedom: the radial size of the cloud increases while the axial size remains constant. The gas then relaxes toward an equilibrium state with a higher temperature and the correct aspect ratio.

In the next section I will give more quantitative details about this technique and then I will show our experimental results. I will then conclude this chapter by making some consideration on the numerical simulation required to obtain the result on the scattering length.

#### 4.2.1 Cross-dimensional thermalization

As pointed out above and from a very general point of view, the decay toward thermal equilibrium, which is driven by collision, carries informa-

tion about the elastic cross section. To practically implement this kind of measurement one needs a reliable way to always prepare the same non-equilibrium state and to monitor its relaxation.

In a harmonic trap, in absence of collisions, the atomic dynamics along different degree of freedom is completely decoupled: the Hamiltonian of the system is in fact separable as we saw in § 1.2.1. If a sample is prepared in this trap with different energy distributions along different directions this difference will not vary with time. On the other hand, due to interactions, the collisions drive the system toward thermal equilibrium, namely, a state in which the total energy is conserved and the effective temperatures of the different degrees of freedom are equal. The energy distribution along the different direction is readily measured as the width<sup>1</sup>  $w$ , of the atomic cloud in the trap since

$$E_i = \frac{1}{2} k_B T_i = \frac{1}{2} m \omega_i^2 w^2, \quad (4.4)$$

where  $\omega$  indicates the trapping frequency.

A reliable way to prepare a non-equilibrium system is again indicated by the presence of a harmonic confining potential. If we modulate the trapping potential with a time dependent profile such that

$$V(\mathbf{r}, t) = (1 + \epsilon(t)) V(\mathbf{r})$$

this will induce transition from the state  $|i\rangle$  to  $|f\rangle \neq |i\rangle$  with a rate which can be easily evaluated with the Fermi's golden rule:

$$R_{i \rightarrow f} = \frac{\pi}{\hbar^2} \left| \langle f | \frac{\partial V}{\partial \epsilon} | i \rangle \right|^2 S_\epsilon(\omega_{fi}), \quad (4.5)$$

where  $S_\epsilon$  is the single sided power spectral density of the modulation  $\epsilon$  and  $\hbar\omega_{fi} = E_f - E_i$ . For a harmonic potential in one dimension one obtains the perturbation connects the initial state  $|n\rangle$  only with the two states  $|n \pm 2\rangle$ . The rate can be easily calculated as:

$$R_{n \rightarrow n \pm 2} = \frac{\pi \omega^2}{16} S_\epsilon(2\omega) (n + 1 \pm 1) (n \pm 1).$$

Starting from the above result it is possible to calculate the heating rate due to this parametric excitation and one finds that is proportional to the average energy. This means that the energy rises exponentially [93]:

$$\langle \dot{E} \rangle = \pi^2 \nu^2 S_\epsilon(2\nu) \langle E \rangle. \quad (4.6)$$

---

<sup>1</sup>We indicate the second moment of the atomic density as  $w$  instead of the more customary  $\sigma$ , to avoid confusion with the cross section.

From Eq. (4.6) one can clearly see that if the modulation is sharply tuned around one of the trapping frequency energy is introduced in the system selectively on that degree of freedom. If the excitation is applied for short times thermalization will not occur and the decay toward thermal equilibrium following the excitation can be measured. Furthermore, since the excitation depends deterministically on the modulation parameters, this gives to the method the required reproducibility.

The ratio of the energy along the excited direction to the others, which is proportional to the square of the aspect ratio  $A_R^2 = w_z^2/w_\perp^2$  (we will assume cylindrical symmetry as in our magnetic trap), exponentially decays to one with a time constant  $\tau_c$  which is proportional to the collision rate  $\gamma_{el}$

$$\tau_c^{-1} = \gamma_c = \frac{\gamma_{el}}{\alpha} = \frac{\bar{n}\langle\sigma v\rangle}{\alpha}, \quad (4.7)$$

where we have expressed the collision rate as a function of the cross section  $\sigma$ , the relative velocity  $v$  and the average density  $\bar{n}$  and  $\langle\cdot\rangle$  indicates averaging over the Boltzmann distribution. The constant  $\alpha$  indicates the average number of collision an atom needs to reach thermal equilibrium: it is on the order of 3, but cannot be easily calculated and in our experiment it was estimated with a numerical simulation that is fully documented in the following § 4.2.3. Therefore, by measuring the time  $\tau_c$ , it is possible to obtain a measurement of the cross section  $\sigma$  and if measurements are available at different temperature, within the effective range approximation (§ 3.1.2), it becomes possible to measure the sign of the scattering length  $a$ .

This *cross dimensional thermalization* process has been used so far to obtain a measurement of the scattering length for Cs [94, 95], Rb [96], Na [97],  $^{40}\text{K}$  [98], Cr [99] and the mixture  $^{87}\text{Rb}$ - $^{40}\text{K}$  [100].

### 4.2.2 Determination of the triplet scattering length

The experimental procedure used to determine the triplet scattering length of  $^{39}\text{K}$  is the following: after the sample has been prepared by means of sympathetic cooling at the desired temperature,  $^{87}\text{Rb}$  is blown away from the trap with a pulse of resonant light, leaving a pure sample of  $^{39}\text{K}$  in the magnetic trap. Then the radial degrees of freedom are excited by modulating the value of the trap bias field at twice the frequency of radial confinement for a time  $t_{mod} = 100$  ms. This time is much longer than the radial period

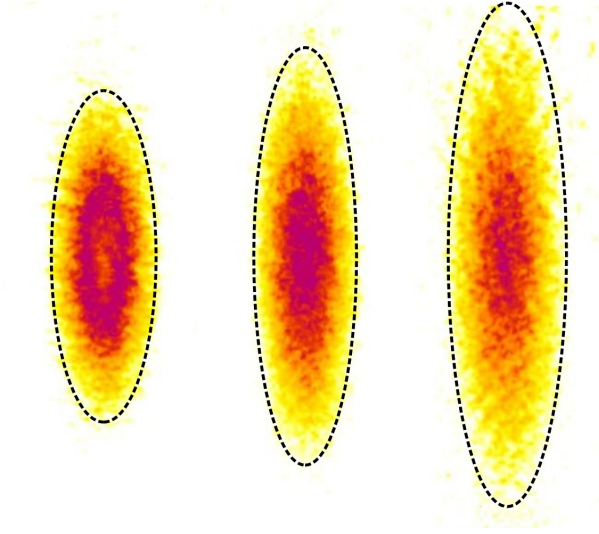


**Figure 4.4.** Absorption images of the cloud of  $^{39}\text{K}$  atoms for different evolution times of 1 s (left), 7 s (center) and 15 s (right). To guide the eye the shape of the clouds is outlined with a dashed line: it relaxes toward a more elongated shape owing to interatomic collisions. Images are taken after a 2 ms expansion.

but shorter than the relaxation time  $\tau_c$ : this means that, when the modulation is switched off, the radial size of the cloud is bigger than at thermal equilibrium and relaxation ensues. We allow a time  $t_w$  for relaxation to occur and then we image the cloud along the vertical radial direction by means of absorption imaging taken *in situ* or after a 2 ms expansion. The relaxation of the cloud can be appreciated from the images shown in figure 4.4 where the cloud evolves toward a more elongated shape. From the measured widths  $w$  of the Gaussian density profile we can calculate the average potential energy along the radial  $r$  and axial  $z$  profile according to Eq. (4.4). We repeated this procedure for different values of the atom number  $N_K$  and for two different values of temperature, 16 and 29  $\mu\text{K}$ . In order to avoid any systematic effect associated to *in situ* imaging such as magnetic field inhomogeneities or to the elongated geometry, the dataset at 16  $\mu\text{K}$  is taken with a slightly different procedure. First, we adiabatically decompress the trap to  $\omega_r = 2\pi \times 290(1)$  Hz and  $\omega_z = 2\pi \times 21.24(1)$  Hz, by reducing the current in the magnetic trap and adjusting the bias field and then blow away  $^{87}\text{Rb}$ , apply parametric excitation at  $\omega_r$ , wait for a variable time and image the cloud after a 2 ms expansion. The ratio  $E_r/E_z$  as a function of  $t_w$  is plotted in figure 4.5 for a typical experimental sequence.

The dependence of the relaxation rate  $\gamma_c$  on the number of atoms which

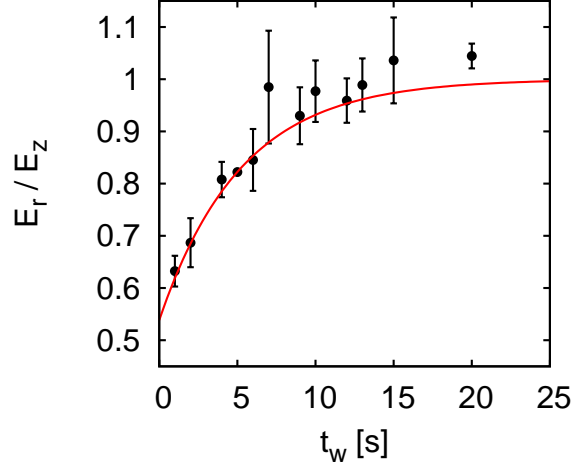


**Figure 4.5.** Plot of the decay of the ratio  $E_r/E_z$  after parametric heating in the radial direction as a function of  $t_w$ . Data are taken after 2 ms expansion. Each point is an average of several experimental realization and the line is an exponential decay fit with equilibrium value fixed to 1. Average initial number of atoms is  $379(10) \times 10^3$  and initial average temperature is  $16.2(7) \mu\text{K}$ . From the fit we obtain  $\gamma_c = 0.20(4) \text{ s}^{-1}$ .

is clearly seen in figure 4.5 can be seen explicitly from Eq. (4.7) remembering that the mean density in a harmonic trap is given by

$$\bar{n} = \left( \frac{m}{4\pi k_B \bar{T}} \right)^{3/2} N_K \omega_r^2 \omega_z, \quad (4.8)$$

where  $\bar{T} = (T_r^2 T_z)^{1/3}$  indicates the geometric average of the temperature along the different directions.

Furthermore a measurement of the relaxation rate at different atomic densities allows to check for the anharmonicity of the trapping potential. In fact, in a Ioffe-Pritchard trap, a sufficiently big atomic cloud can experience a potential that is not strictly separable so that different degrees of freedom are coupled and relaxation can occur even in the absence of collisions. We refer to this process as *ergodic mixing*. *A priori*, for equal harmonic frequencies, ergodic mixing could play a more prominent role in our magnetic trap than in the usual traps due to its small size. For this reason we take ergodic mixing into account by separating the component of the relaxation rate, which is linear in  $N_K$ , from the extrapolation in the limit of zero density where relaxation can occur only through ergodic mixing. If we plot the rate  $\gamma_c$  as a function of  $N_K$  we expect the data to stay on

$\bar{T}$ [ $\mu\text{K}$ ]	$a, r_e = 0$	$a$ pos.	$a$ neg.
16(1)	$\pm 57$	+55	-67(11)
29.8(1.3)	$\pm 35$	+25	-48(5)

**Table 4.1.** Experimental results. Scattering lengths are in atomic units.

a line

$$\gamma_c = \alpha^{-1} \frac{d\gamma_{el}}{dN_K} N_K + \gamma_{mix} = AN_K + \gamma_{mix}, \quad (4.9)$$

where  $\gamma_{mix}$  is the time constant of the ergodic mixing process and  $\gamma_{el}$  is then given by Eq. (4.7). The plot of the experimental data are shown in figure 4.6 together with a linear fit. In both cases the value of  $\gamma_{mix}$  is very well consistent with zero and therefore we can conclude that at these temperature ergodic mixing can be neglected in our magnetic trap.

The slope  $A$  extracted from the fit can be related to the scattering length within the effective range approximation with a few simple steps. First since we deal with identical particles, the cross section is given by Eq. (3.19) with  $p = 2$  and  $m_R = m/2$  and the average over the Boltzmann distribution can be therefore written as

$$\langle \sigma v \rangle = 32\sqrt{\pi} \sqrt{\frac{k_B T}{m}} a^2 I(a, k_T), \quad (4.10)$$

where  $k_T$  is that of Eq. (3.15) and  $I(a, k_0)$  is the following integral

$$I(a, k_T) = \int_0^\infty \frac{\xi e^{-\xi} d\xi}{(1 - \frac{1}{2} r_e a k_T^2 \xi)^2 + k_T^2 a^2 \xi}, \quad (4.11)$$

which must be evaluated numerically. Taking the definition of  $A$  from Eq. (4.9) and inserting Eq. (4.10) and Eq. (4.8) into Eq. (4.7) one obtains that

$$A = \alpha^{-1} \frac{4}{\pi} \frac{m}{k_B T} \omega_r^2 \omega_z a^2 I(a, k_T). \quad (4.12)$$

By numerically inverting Eq. (4.12) and taking  $\alpha = 2.7$  from the numerical simulation described in § 4.2.3, it is possible to find a value for the scattering length for each of the two datasets. Clearly the two values should be consistent within the experimental errors.

Our results are summarized in table 4.1: as we can see the experimental uncertainty is fairly high and does not allow to determine the sign of the scattering length nor to assess the importance of the effective range approximation: we can only notice that the agreement between the two determinations is slightly better in the case of negative  $a$ . The quoted error is

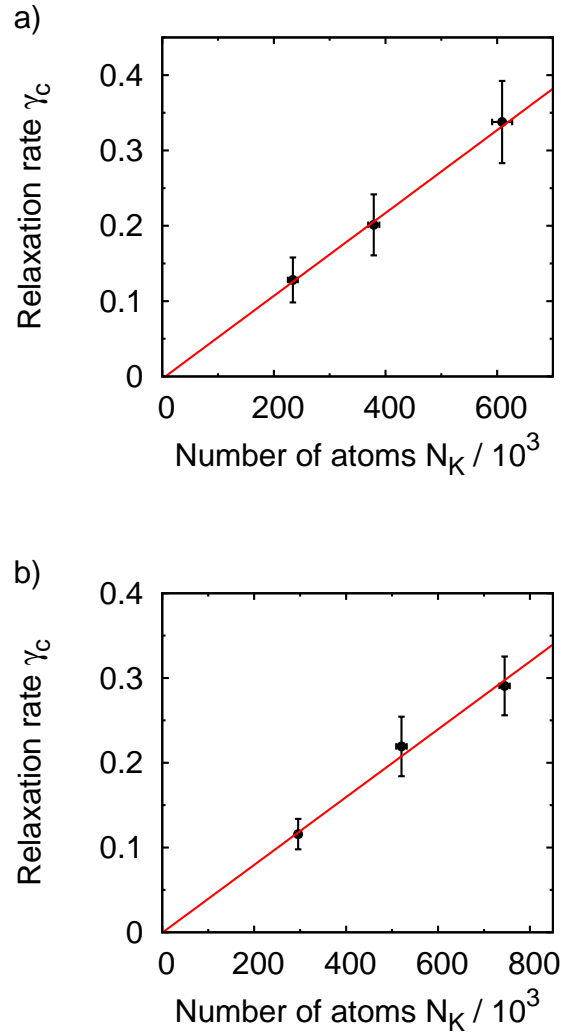


**Figure 4.6.** Plot of the measured relaxation rate as a function of the number of atoms in the sample after expansion (a) and in situ (b).  $\bar{T}$  is  $16(1) \mu\text{K}$  and  $28.9(1.3) \mu\text{K}$  respectively. The line is a fit with Eq. (4.9); fit results are:  $\gamma_{mix} = -0.003(0.065) \text{ s}^{-1}$  and  $A = 5.5(1.6) \times 10^{-7} \text{ s}^{-1}$  for figure (a) and  $\gamma_{mix} = -0.0005(0.034) \text{ s}^{-1}$  and  $A = 4.0(1.0) \times 10^{-7} \text{ s}^{-1}$  for figure (b). Error bars on the vertical direction are statistical error on the exponential decay fit, while on the horizontal direction they are the statistical fluctuation of the initial number of atoms not including the calibration uncertainty.

the sum of the statistical contribution obtained from the linear fit shown in figure 4.6 and the uncertainty associated to the atom number calibration. This is done independently for each of the two trap configurations owing to the different optical density: the obtained calibration error is around 20%.

However, according to the previous measurement of  $a$  [80, 81], we assumed a negative scattering length and obtained the combined results of

$$a = -51(7)$$

which agrees with the previous measurements within 1.7 standard deviations. Here the error is obtained taking a weighted average of the two scattering length values and multiplying the associated uncertainty by a factor  $\chi^2 = 1.65$ , to set the confidence level to 68% [101].

After the publication of our work, high precision Feshbach spectroscopy of this isotope was performed by our colleagues at LENS [83]: their results is  $-33.3(3)$  which confirms the slight overestimation of our measurement. This is likely due to an underestimate of the number of atoms especially for the low temperature measurement for which in fact the agreement is poor. Nevertheless, the test of the machine was positive and allowed us to familiarize to the experimental operation of the magnetic millitrap: in particular on how to change the trap geometry and manage the thermal stability. These insights were exploited for the realization of the experiments with two Bose-Einstein condensate in a 3D optical lattice which are reported in chapter 6.

### 4.2.3 Numerical simulation

The value of  $\alpha$  used in the last section was obtained by means of a numerical simulation that I will now describe. Following [94, 95, 102] we take advantage of the low density and small atom number of the sample to make a direct simulation of the gas in which we consider 3D position and velocity of every single atom.

#### General principle

Choosing a time interval  $\delta t$  much smaller than both the average collision time  $\tau_c$  and the faster timescale of single particle dynamics, namely  $\omega_{\perp}^{-1}$ , one may assume that during this time interactions between atoms are weak enough that they decouple with the center of mass motion and that the

force experienced by the atoms varies little. This approximation is at the root of one of the most powerful method of dilute classical gas simulation: direct Monte Carlo simulation (DMCS) [103]. The code used to simulate our experiment is however not purely DMCS in that, although it still involves an aleatory element in deciding the outcome of a collision event, all collisions are taken into account. Furthermore, although in principle interaction can be simulated with the full two-body potential, to simplify the code we take interactions into account as short range, hard-sphere collisions.

The simulation procedure is quite simple:

0. Setup an initial state taking  $N$  atoms from an anisotropic Maxwell-Boltzmann distribution.
1. Update position and velocity of all the atoms according to external forces.
2. Discretize the positions of the atoms on a lattice of spacing  $\delta x$  and, if two atoms are located at the same site, make a collision test.
3. If the collision test is positive, resolve the collision.

Repeating steps 1-3 of this procedure for a sufficiently long time and keeping into account the total number of collisions allows to obtain the value of  $\alpha$ . First  $\gamma_c$  is evaluated with the same fitting procedure used for experimental data, then one finds the number of collisions per particle that occurred in time  $\tau_c$ : by definition that is the value of  $\alpha$ .

### **Numerical details and results**

I will now give some detail of the C++ code used to implement the algorithm outlined above. Each atom is modeled with a data structure containing three integer numbers representing the position on a fine grid of size  $\delta x = 50$  nm and three floating point number representing the velocity, typically  $N = 2 \times 10^4$ . The initial state is prepared with a simple accept/reject method starting from randomly generated phase space configuration. The position update is made with a Verlet integrator:

$$x'_i = x_i + v_i \delta t + \frac{\delta t^2}{2m} F_i(\mathbf{x}) \quad (4.13)$$

$$v'_i = v_i + \frac{\delta t}{2m} (F_i(\mathbf{x}') + F_i(\mathbf{x})) \quad (4.14)$$

where  $F$  indicates the external forces. Formally this is a second order Runge-Kutta method but it can be shown that it is exactly symplectic, that is satisfies Liouville theorem [104]. Unfortunately it is not energy conserving and therefore particular attention has to be made on the choice of  $\delta t$  not to introduce numerical “heating” or “cooling” in the simulation: we checked that after 30 s of simulated time the total energy of the system is still the same within  $5 \times 10^{-3}$ .

In order to save computation time the frequency at which collision test is made should be such that the probability for a collision to happen is significant but it should not be too big not to artificially inflate the number of collisions: typically 5% is a reasonable value. The collision test consists in comparing a random real number  $y$ , uniformly distributed in  $[0, 1)$ , with the collision probability calculated according to kinetic theory:

$$\wp = \sigma |v_r| M \delta t L^{-3} \delta x^{-3}, \quad (4.15)$$

where  $v_r$  is the relative velocity between the two colliding partners and  $M$  and  $L$  are two integers that represents respectively the number of time steps between two collision tests and the size of the grid in which tests are made. These two parameters are not independent: in practice one chooses  $L$  so that collisions are binary (i.e. the maximum occupation number of a cell of size  $L \delta x$  is two) and then one should choose  $M$  so that in a time  $M \delta t$  the atoms travel on average a distance  $r \simeq L \delta x$ . If  $r \gg L \delta x$  the effective volume of the collision test is bigger than the one explored by the atom and it is nonphysically likely that the same pair will collide again at the next test, if opposite  $r \ll L \delta x$  collisions will be underestimated as many trajectory crossing are missed. We avoided these effect by checking that the collision rate obtained from the simulation is independent on both  $L$  and  $M$ .

The collision is processed if  $y < \wp$ : in this case one assumes that the collision is hard-sphere and  $s$ -wave. As a consequence position are unchanged and velocities are updated according to

$$\begin{cases} \mathbf{v}'_1 = \mathbf{v}_{CM} + \frac{|v_r|}{2} \hat{\mathbf{e}}_R \\ \mathbf{v}'_2 = \mathbf{v}_{CM} - \frac{|v_r|}{2} \hat{\mathbf{e}}_R \end{cases}$$

where  $\mathbf{v}'_i$  indicates the velocity of particle  $i$  after the collision,  $\mathbf{v}_{CM}$  is the center of mass velocity before the collision, and  $\hat{\mathbf{e}}_R$  is a random direction on the unit sphere. At this point the system is ready for another iteration.

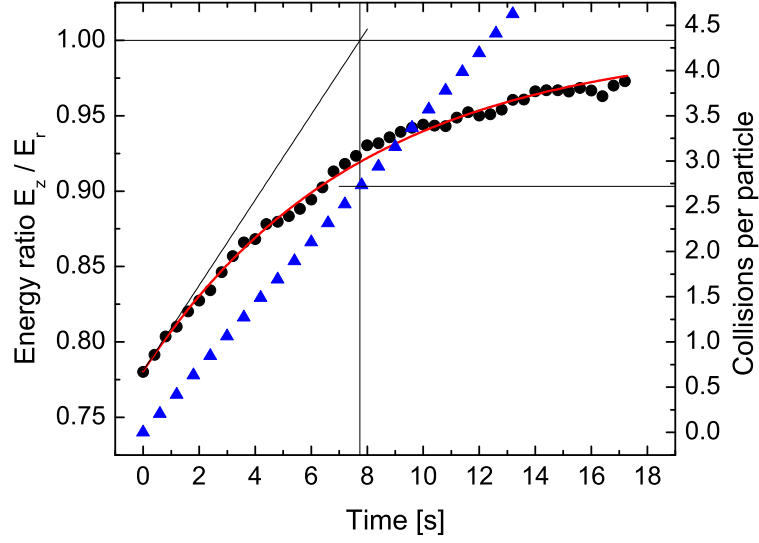


**Figure 4.7.** Plot of the energy ratio for the results of the simulation (black dots, left scale) and the number of collisions per particle (blue triangles, right scale) and the number of collisions. The red line is an exponential fit: the value  $\alpha = 2.72$  can be read on the plot from the fitted time constant of 7.74 s.

A typical results of our simulations for  $N = 2 \times 10^4$  is shown in figure 4.7, where we plot the radial to axial energy ratio and the number of collisions as a function of time. The confining potential is that of our magnetic trap with  $\omega_{\perp} = 2\pi \times 440$  Hz and  $\omega_z = 2\pi \times 29.4$  Hz. The initial effective temperature is  $15(19.5) \mu\text{K}$  along the axial (radial) direction. The cross section used in this simulation is  $8.6 \times 10^{-16} \text{ m}^2$  in order to have a collision rate comparable to that of the experiment in spite of the reduced density. From the fit we obtain  $\tau = 7.74$  s which gives  $\alpha = 2.72$ .



## **Part III**

# **Experiments with $^{41}\text{K}$ - $^{87}\text{Rb}$ mixture**



# Introduction

As we have seen in the previous chapter, the creation of a stable degenerate mixture of  $^{39}\text{K}$  and  $^{87}\text{Rb}$  is not possible at low magnetic field since the interaction of  $^{39}\text{K}$  is attractive. Furthermore, as it is clearly demonstrated in [73], the efficient realization of a degenerate mixture of  $^{39}\text{K}$  and  $^{87}\text{Rb}$  requires to extensively tune both the inter- and intra-species scattering lengths. In view of producing a mixture of two superfluids it is much more straightforward to work with the other stable bosonic isotope of K, namely  $^{41}\text{K}$ . As already pointed out, the first realization of a mixture of two degenerate gases was indeed reported on this mixture in [22].

We were able to repeat this result and obtain the degenerate mixture, as shown in figure 6.2. This crucial step allowed us to obtain all the results presented in chapter 6. The structure of this part is the following: in chapter 5 I will introduce optical lattices and the most important issues that will allow the reader to understand the results presented in chapter 6. Finally in chapter 7 I will present the first results about the Feshbach resonances of the mixture  $^{41}\text{K}$ - $^{87}\text{Rb}$ .



## Chapter 5

# BEC in periodic potentials

Science may be described as the art of systematic oversimplification.  
(Karl Popper)

The way laser beams can be used to generate a periodic potential for the atoms has been described in § 1.1.3. In this chapter we will see that the physics of Bose-Einstein condensates in optical lattices is very rich and can allow unprecedented experiments on particles in periodic potential enabling the experimental verification of effects originally predicted for electrons in an ion lattice.

I will follow the scheme of § 1.2 in that I will begin looking at the problem of non interacting atoms and then I will consider the case in which interactions are present: in particular we will see that, for a high enough periodic potential, cold atoms in an optical lattice represent a realization of the Bose-Hubbard model. I will then show how to compute the phase diagram of this model which exhibits a quantum phase transition from the superfluid state to an insulating state called Mott insulator.

I will then review the available theoretical results about two Bose-Einstein condensates in an optical lattice addressing the different regimes. I will conclude discussing the impact on the theoretical analysis of the trapping potential present in the experiments.

### 5.1 Non-interacting BEC

In analogy to what we've seen in § 1.2.1, we can expect that in an ideal Bose gas at zero temperature all the particle will occupy the ground state of the single particle problem. The single particle Schrödinger equation is

given by

$$\left(-\frac{\hbar^2}{2m}\nabla^2 + sE_{\text{rec}}\sum_i \cos^2(\pi r_i/\lambda)\right)\psi = E\psi, \quad (5.1)$$

and several consequences stem from the structure of this equation.

### 5.1.1 Bloch bands

Neglecting the finite size of the system the previous equation is invariant under translation by any linear combination of the direct lattice vectors  $\mathbf{d} = (\lambda/2)\hat{e}_i$ . This enables one to apply the Bloch theorem and write the eigenvector of the Schrödinger equation (5.1) as

$$\psi(\mathbf{r}) = u(\mathbf{r}, \mathbf{Q}) \exp\left(-\frac{i}{\hbar}\mathbf{Q} \cdot \mathbf{r}\right)$$

where  $u$  has the periodicity of the direct lattice and the corresponding eigenvalues have the form

$$E = E(n, \mathbf{Q})$$

where  $n$  is an integer number and  $\mathbf{Q}$  a real quantity. This spectrum has the characteristic band structure that is found also in solid state physics:  $n$  is called *band index* and  $\mathbf{Q}$  is the *quasimomentum*. The periodicity in the direct lattice generates the periodicity of the quasimomentum in the reciprocal lattice: the base vector of the reciprocal space is  $2\pi/d = 2k_L$  where  $k_L = 2\pi/\lambda$ . From the spacing and directions of vectors in the reciprocal space one can construct the Bragg planes and divide the reciprocal space into different Brillouin zones. In 1D these Bragg “planes” are actually points and Brillouin zones are segments, while in 2D and 3D the situation is more complicated as it is shown for 2D in figure 5.1. Since however the Schrödinger problem (5.1) is separable, we will now restrict to the 1D problem which retains all the interesting point of the discussion. A solution of this problem can be traced back to that of the Mathieu equation [105], but we will show here an alternative, more practical approach.

Taking advantage of the Bloch theorem we can Fourier transform Eq. (5.1) taking

$$\begin{aligned} \psi(x) &= e^{iqk_L x} \sum_{m \in Z} c_m(n, q) e^{i2mk_L x} \\ V(x) &= E_{\text{rec}}(s/2 + s/4e^{i2k_L x} + s/4e^{-i2k_L x}) \end{aligned} \quad (5.2)$$

where  $q = Q/(\hbar k_L)$ . What we obtain is then an infinite system of linear equation for the  $c_m$  coefficients [106, 107]:

$$A_m c_m + B(c_{m+1} + c_{m-1}) = \epsilon c_m \quad (5.3)$$

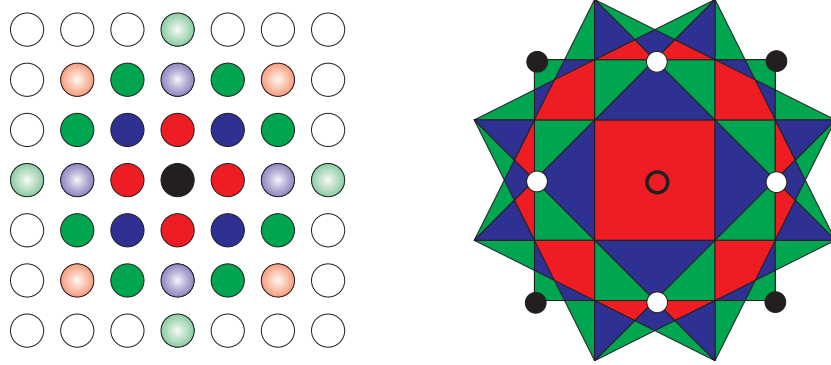


**Figure 5.1.** Direct and reciprocal lattice in 2D. In the left picture sites are marked to show up to the sixth to nearest neighbors: from these positions the so-called Bragg planes can be designed which allow to reconstruct the shape of the Brillouin zones. In the right part of the figure, dots mark the position of reciprocal lattice vector:  $|Q| = 0$  (open circle),  $|Q| = 2k_L$  (white dots) and  $|Q| = 2\sqrt{2}k_L$  (black dots).

where

$$A_m = (q + 2m)^2, \quad B = s/4, \quad \epsilon = E(n, q)/E_{\text{rec}} - s/2. \quad (5.4)$$

The eigenvalue equation 5.3 can be numerically solved introducing a cutoff  $M$  on the maximum number of plane waves<sup>1</sup> and putting Eq. (5.3) in matrix form:

$$H_q c = \epsilon c,$$

where  $H_q$  is a tridiagonal matrix with dimension  $2M + 1$ ,  $A_m$  on the principal diagonal and  $B$  on the upper and lower diagonals. From the eigenvalues  $\epsilon_{n,q}$  it is straightforward to obtain the spectrum  $E_{n,q}$  and the corresponding eigenfunctions  $\psi$  from the plain waves expansion, Eq. (5.2). The result of this procedure is shown in figure 5.2 where we compare the spectrum in the lattice for two different lattice heights with the one of the free particle. As we expected bandgaps open in the spectrum and energy bands are flatter with increasing lattice height: it is possible to connect the curvature of the energy bands to the *effective mass* of the particle in the lattice and indeed the dynamics of the condensate in the regime of low density (where interaction effects play a minor role) can be described in terms of Bloch waves [106].

<sup>1</sup>This corresponds to consider a finite lattice with  $2M + 1$  sites and periodic boundary conditions.

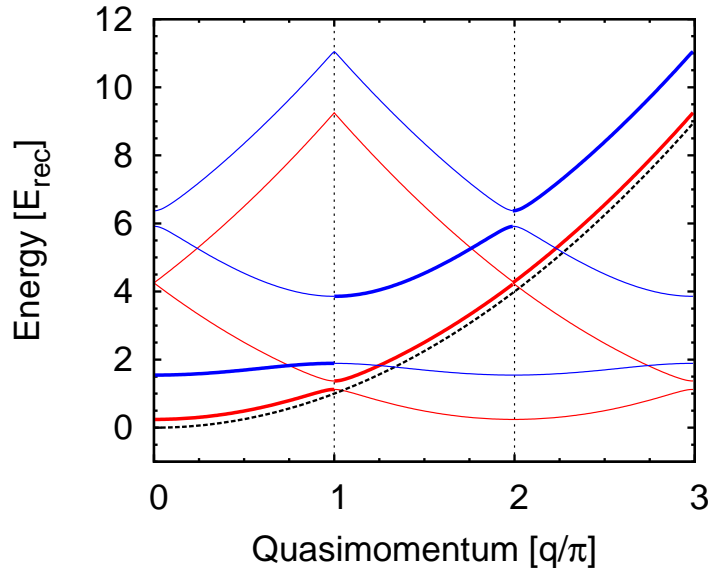


**Figure 5.2.** Bloch bands in the repeated and extended scheme for  $s = 0.5$  (red) and  $s = 4.0$  (blue).

### 5.1.2 Wannier picture

A complementary approach to that of Bloch waves is that of the so-called Wannier functions which are localized states of each lattice well. Within this framework, Bloch waves, regarded as a function of quasimomentum, are periodic in the reciprocal lattice. This means that they can be expanded as plane waves in the direct lattice. It is easy to show that this leads to the following expansion [108]:

$$\psi(x; n, q) = \sum_m \phi_n(x - md)e^{iqk_L x} \quad (5.5)$$

where the functions  $\phi_n$  are called *Wannier functions* and can be expressed in terms of Bloch waves as [108]

$$\phi_n(x - md) = \frac{1}{2\pi} \int_{BZ} \psi(x; n, q)e^{i\pi m q} dq. \quad (5.6)$$

It can be shown that the Wannier functions are an orthonormal basis.

In practice if the lattice is sufficiently high, the low lying Bloch states explore only the bottom part of the periodic potential where it can be approximated by a harmonic potential. In this case Wannier functions are Gaussian centered in each lattice site and this approximation is frequently used in practice. Furthermore, in view of studying the problem of interacting atoms in periodic potential, the Wannier picture is more useful because

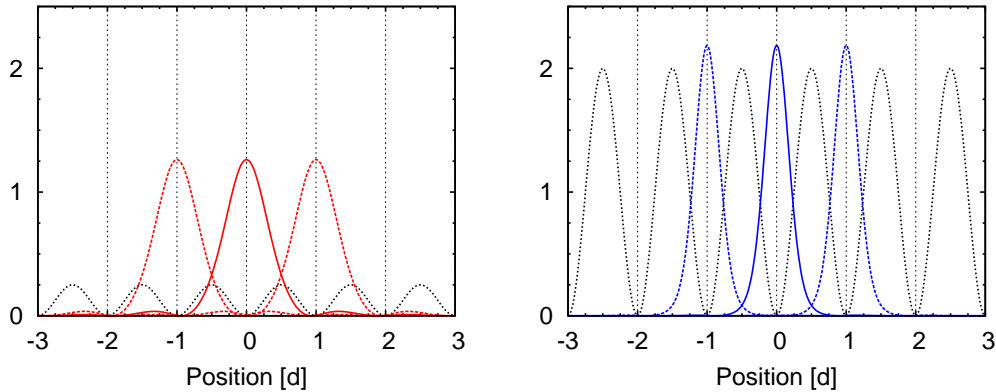


**Figure 5.3.** Wannier function of the lowest band for  $s = 0.5$  (left) and  $s = 4.0$  (right). Note the reduced width and the disappearance of secondary maxima in the right picture. The dotted curve in the background is the lattice potential

local interaction are easily included in the localized Wannier states as we will see in the next section. A plot of the lowest band Wannier function for two different heights of the optical lattice is shown in figure 5.3.

## 5.2 The Bose-Hubbard model

The key aspect that makes ultracold atoms in optical lattices so interesting is that within a few approximations that can be fulfilled in the experiments, they are a perfect realization of the Bose-Hubbard model [109]. We will now briefly review this point and then we will introduce the key features of the Bose-Hubbard physics.

### 5.2.1 From Gross-Pitaevskii to Bose-Hubbard

The starting point for the zero temperature analysis of the Bose-Einstein condensate in an optical lattice is the Gross-Pitaevskii equation (1.28) for a periodic potential. Solutions to this equation in the limit of weak lattice can be formulated in form of non-linear Bloch states which exhibits a plethora of phenomena typical of non-linear wave equations such as solitons [110], dynamical instability [111] and many others which are nicely reviewed in [5, 106]. However, when the lattice height is such that the density in each well increases, the correlations among the particles become more and more important and the mean field approximation becomes impractical. In this regime one has to go back to the full Hamiltonian of the system Eq. (1.26)

and use another approach. We will detail this approach in the following.

If the temperature of the system is much lower than the width of the first noninteracting energy band we can expand the field operator in Eq. (1.26) on the basis of the first band of Wannier functions:

$$\hat{\Psi}(\mathbf{r}) = \sum_j w_j(\mathbf{r}) \hat{a}_j \quad (5.7)$$

where to simplify the notation we set  $w_j(\mathbf{r}) = \phi_0(\mathbf{r} - \mathbf{R}_j)$  and we have introduced the Fock operators  $\hat{a}_j$  ( $\hat{a}_j^\dagger$ ) which destroy (create) a particle on site  $j$ . The resulting expression can be further simplified by the so called Hubbard approximation which amounts to neglect the spatial overlap between the Wannier functions beyond the nearest-neighbors. Within this approximation Hamiltonian has the following form [109]

$$\mathcal{H} = -J \sum_{\langle i,j \rangle} (\hat{a}_i^\dagger \hat{a}_j + \hat{a}_j^\dagger \hat{a}_i) + \frac{U}{2} \sum_i \hat{n}_i (\hat{n}_i - 1), \quad (5.8)$$

where  $\langle i, j \rangle$  indicate that the sum is only over neighbors sites and we introduced the number operators  $\hat{n}_i = \hat{a}_i^\dagger \hat{a}_i$  and the two energy scales  $J$  and  $U$  for tunneling and on-site interactions respectively. In the following we will work in the grand canonical ensemble and we will add a term  $-\mu \sum_i n_i$ , where  $\mu$  is the chemical potential.

The two parameters  $U$  and  $J$  can be calculated knowing the non-interacting Wannier functions [109] as

$$J = \int d^3r w_i(\mathbf{r}) \left( -\frac{\hbar^2}{2m} \nabla^2 + V_{\text{lat}}(\mathbf{r}) \right) w_j(\mathbf{r}), \quad (5.9)$$

where  $V_{\text{lat}}(\mathbf{r})$  indicates the periodic potential, and

$$U = g \int d^3r |w(\mathbf{r})|^4. \quad (5.10)$$

Note that, using the definition of the Wannier function, the tunneling amplitude can be traced back to the Bloch spectrum. In particular one has that [78]

$$J = \frac{1}{v_{BZ}} \int_{BZ} d^3q E_0(\mathbf{q}) \exp(-i\mathbf{q} \cdot \mathbf{d}) \quad (5.11)$$

where  $\mathbf{d}$  is a direct lattice vector and  $v_{BZ}$  the volume of the first Brillouin zone.

An analytical expression for  $U$  and  $J$  can be given in the limit of  $s \gg 1$ , but we will use an empirical expression based on a fit to the numerically

computed coefficients in the range  $8 < s < 30$  given by [112]:

$$\begin{aligned} U/E_{\text{rec}} &= 5.97 (a/\lambda) s^{0.88} \\ J/E_{\text{rec}} &= 1.43 s^{0.98} \exp(-2.07\sqrt{s}). \end{aligned} \quad (5.12)$$

By changing the height of the periodic potential it is therefore possible to explore the two regimes dominated either by the tunneling at low  $s$  values or by the on-site interactions for  $s \gg 1$ . We will now see that the ground state of the system in these two regimes is very different.

### 5.2.2 Phase diagram of the homogeneous system

Consider first the case where the number of atoms  $N$  is an integer multiple of the number of sites  $M$ :  $N = \bar{n} M$ . For a vanishing tunneling amplitude, the Hamiltonian is a sum of single site contributions and it is trivial to see that the ground state is given by

$$\Psi_{MI}(\bar{n}) = \prod_m (\hat{a}_m^\dagger)^{\bar{n}} |0\rangle. \quad (5.13)$$

This state, being a product state, has no site to site correlations and it is easy to see that any elementary excitation will cost at least an amount  $U$  of energy: this means that the excitation spectrum is gapped. We call this state a *Mott insulator*.

On the other hand, if the on-site interactions are vanishing, we recover the ideal gas that we analyzed above (§ 5.1): we know that the ground state is a Bose-Einstein condensate where all the particles are in the lowest Bloch wave ( $q = 0$ ). This state is therefore *superfluid* and without any constraint on  $N$  and  $M$  the many body state can be written as [113, 78]

$$\Psi_{SF}(N) = \frac{1}{\sqrt{N!}} \left( \frac{1}{\sqrt{M}} \sum_m \hat{a}_m^\dagger \right)^N |0\rangle. \quad (5.14)$$

In the limit  $N, M \rightarrow \infty$ ,  $\Psi_{SF}(N)$  is a coherent state [78] in which the site-to-site coherence is maximal. Beside this, as shown in figure 5.2, there is no gap in the energy spectrum close to  $q = 0$ .

Another striking difference between the two states can be seen in their momentum distribution. For a cubic lattice this quantity can be expressed as [114, 115, 116, 113, 117]

$$n(\mathbf{k}) = |\tilde{w}(k)|^2 \sum_{i,j} \exp(i\mathbf{k}(\mathbf{r}_i - \mathbf{r}_j)) \langle \hat{a}_i \hat{a}_j \rangle, \quad (5.15)$$

where  $k = p/\hbar$ , the summation is extended to all occupied lattice sites and  $\tilde{w}$  indicates the Fourier transform of the lowest band Wannier function. In the above expression the term  $\langle \hat{a}_i \hat{a}_j \rangle$  is the one body density matrix<sup>2</sup>, which has a totally different behavior for the superfluid and the Mott insulator states. In the superfluid regime, assuming for simplicity a uniform system, the density matrix is constant for any pair  $(i, j)$  and equal to the superfluid density: the density profile in momentum space is therefore given by peaks located at the reciprocal lattice vectors. On the other hand, when the system is in a Mott-insulator state such as that defined by Eq. (5.13), the one body density matrix is exponentially decaying around  $k = 0$ . As we will see in chapter 6 it is possible to experimentally probe the one-body density matrix and thus distinguish between the two states. We emphasize here that, if the number of particle is not commensurate with the number of lattice sites, an exact Mott insulator cannot be formed: even if there is only one extra particle the system will lower its energy by delocalizing it over all the lattice sites. The delocalized particles will always establish a site-to-site correlation and will spoil the energy gap effectively making the system look superfluid for any  $J \neq 0$ ; we will see that this is different for an inhomogeneous system in § 5.2.3.

Once the nature of the ground states in the two limits  $U/J \rightarrow 0$  (superfluid) and  $U/J \rightarrow \infty$  (Mott insulator) is established, the next step is to characterize the behavior of the system in the intermediate regime that is to find the phase diagram as a function, for instance, of the  $U/J$  ratio and of the chemical potential. One could naively expect that a standard treatment based on the Bogoliubov approximation (see § 1.2.2) will be able to capture at least the existence of a phase boundary. Actually it turns out that this is not the case and the Bogoliubov theory fails in predicting the depletion of the condensate associated to the transition toward a Mott phase [118]. We will now see that a more clever formulation of a mean field theory can reproduce the feature of the model with great accuracy.

### Site decoupling mean-field

One of the problem in the approach of the Bose-Hubbard Hamiltonian is given by the tunneling term which couples the different site. Near the transition to the Mott phase, we expect that the tunneling energy is smaller than the on-site interaction and for this reason it seems sensible to treat

---

<sup>2</sup> $\langle \hat{a}_i \hat{a}_j \rangle$  can be called as well first order correlation function or phase coherence.

exactly the interaction term and to find a good approximation for the tunneling. In this line one can use a mean-field approximation in which the tunneling term is written as [119, 118]

$$\hat{a}_i^\dagger a_j = \langle \hat{a}_i^\dagger \rangle \hat{a}_j + \langle \hat{a}_j \rangle \hat{a}_i^\dagger - \langle \hat{a}_i^\dagger \rangle \langle \hat{a}_j \rangle = \psi_i^* \hat{a}_j + \psi_j \hat{a}_i^\dagger - \psi_i^* \psi_j, \quad (5.16)$$

where  $\psi = \langle \hat{a}_i \rangle$  is the superfluid order parameter which in the following will be considered a real quantity. With this approximation Eq. (5.8) becomes

$$H = \sum_i H_i = \sum_i \left[ \frac{U}{2} \hat{n}_i (\hat{n}_i - 1) - \mu \hat{n}_i - zJ \psi (\hat{a}_i + \hat{a}_i^\dagger) + zJ \psi^2 \right], \quad (5.17)$$

where  $z$  is the number of nearest neighbors (twice the dimensionality of the lattice). Dropping the site index and rescaling all the energies by  $zJ$ , this Hamiltonian can be written in matrix form on the single-site Fock basis  $\{|n\rangle\}$ :

$$H_{n,m} = \langle n | H | m \rangle = [(\bar{U}/2)(n-1) - \bar{\mu} + \psi^2] n \delta_{n,m} - \sqrt{n} \psi \delta_{n-1,m} - \sqrt{n+1} \psi \delta_{n+1,m} \quad (5.18)$$

From this matrix formulation it is easy to obtain the ground state on the Fock basis and the relative superfluid density with the following numerical procedure [119]. The matrix (5.18) is diagonalized imposing a cut-off on the maximum occupation number  $M$  for different values of  $\psi$ . The value of  $\psi$  is chosen which minimizes the lowest eigenvalue: the corresponding eigenvector is then the ground state of the system.

With this procedure it is possible to reconstruct the phase diagram as a function of the chemical potential and the lattice height: whenever the solution is found for  $\psi = 0$  the system is in the Mott phase and when  $\psi \neq 0$  the system is superfluid. This phase diagram for  $^{87}\text{Rb}$  is reported in figure 5.4: the different lobes correspond to higher filling of the Mott phase. As we can see, the Mott phase can be approached by increasing the lattice height at constant chemical potential and it is worth noting that there is no direct phase transition from e.g. a Mott phase with one atom per site to the one with two atoms. This will be very important for the case of the inhomogeneous system as we will see in § 5.2.3.

### **The phase transition**

The mean field approach of Eq. (5.16) can be used also to construct an effective action for the system treating the term  $\psi(\hat{a}^\dagger + \hat{a})$  as a perturbation. Calculations to the order in  $\bar{U}^{-4}$  show a nice agreement with the numerical

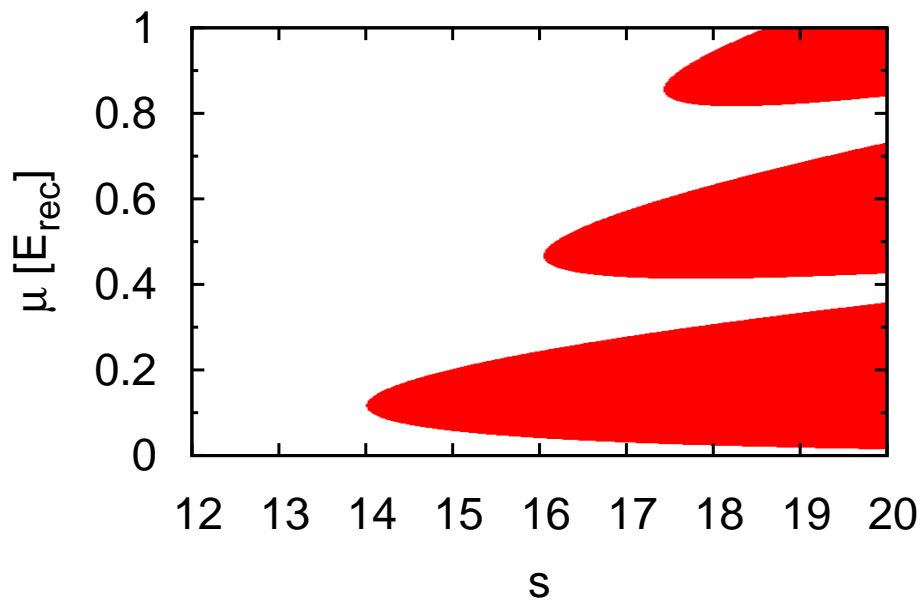


**Figure 5.4.** Phase diagram of the Bose-Hubbard Hamiltonian as a function of the chemical potential and the height of the optical lattice. Shaded regions correspond to the Mott insulator lobes.

solution [118]. In particular it is possible to derive an analytic expression for the critical value  $(U/zJ)_c$  which gives the tip of each Mott lobe in the phase diagram. Up to order  $\bar{U}^{-2}$ , this is given by [118]

$$\left(\frac{U}{zJ}\right)_c = \bar{U}_c = 2n_0 + 1 + \sqrt{(2n_0 + 1)^2 - 1}, \quad (5.19)$$

which gives the following values for the first three lobes: 5.8, 9.9, 13.9. These values are confirmed by Monte Carlo studies both at zero and finite temperature [120, 121]. However, a thorough study of this phase transition was already contained in the pioneering work [122], where the phase diagram was constructed for the first time and the characteristic of the phase transition were qualitatively understood. In particular one has that a second order phase transition is possible only for a commensurate chemical potential (i.e.  $\mu = U(n_0 - 1/2)$ ). In this case the transition is in the class of a  $(d + 1)$ -dimensional XY model [122, 123]. In the other cases one finds a generic mean-field transition which is first-order like in the sense that the density of the system changes and the free energy shows strong finite-size effect [123]. In sharp contrast, the phase diagram at constant density (i.e. constant number of particles) shows that the qualitative result pointed out above is confirmed: the increase in the on-site interaction leads to a change in the chemical potential such that the systems “avoids” the Mott lobes and stays superfluid for all the value of the lattice height. This is in no longer the case in the inhomogeneous system which I now discuss.

### 5.2.3 Inhomogeneous systems

In presence of an external trapping potential  $V_T$ , Eq. (5.8) can be written as

$$H = -J \sum_{\langle i,j \rangle} (\hat{a}_i^\dagger \hat{a}_j + \hat{a}_j^\dagger \hat{a}_i) + \frac{U}{2} \sum_i \hat{n}_i (\hat{n}_i - 1) - \sum_i (\mu - V_{T i}) \hat{n}_i, \quad (5.20)$$

which can be brought back to the usual form introducing a local chemical potential

$$\mu_i = \mu - V_{T i}. \quad (5.21)$$

This was first put out in the context of cold atoms by [109] where the system was analyzed by means of a Gutzwiller ansatz:  $|\Psi\rangle = \prod_i |\phi_i\rangle$  where the on site wave function is a superposition of Fock states, namely  $|\phi_i\rangle = \sum_n f_{n i} |n\rangle$ . The key finding is that in a trapped system with peak chemical potential  $\mu$ , all the phases with  $\mu_i < \mu$  are present simultaneously

[109, 124, 78]. This is illustrated in figure 5.5 where I plot the solution obtained in the site decoupling approximation applying to each site its own local chemical potential [112], for three different values of the chemical potential. As we can see the structure resembles that of a “wedding cake” in which Mott and superfluid domains are alternated. With this respect the grand canonical approach is correct because every Mott region is in contact with a superfluid shell which acts as a particle reservoir. In the case of inhomogeneous trapping we don’t have any requisite on commensurate filling: the typical fluctuation in the number of atoms present in the experiment will simply change the number of atoms in the outer superfluid shell, while the filling of the Mott regions will remain the same.

The absence of a direct transition between different Mott lobes increasing the chemical potential reflects here on the fact that there is always a gap between the two Mott shells. However, depending on the trapping frequency, this gap can be reduced to two sites or less as it is shown in the top and central part of figure 5.5. In this situation one can expect that the superfluid fraction plays only a minor role [124].

### 5.3 Two BEC’s in an optical lattice

I will now introduce the physics of two Bose-Einstein condensates in an optical lattice: I will show how the presence of interspecies interaction enriches by far the phase diagram. Furthermore I will show that this kind of systems has several analogues in the domain of magnetic ordering. Maybe this analogy is the ultimate cause to the huge theoretical literature that flourished on this subject in the last years. Quite surprisingly this theoretical interest has not yet found a comparable experimental effort: this again is one of the main motivation that sparked our interest toward the mixture of two bosons in an optical lattice.

For sufficiently low temperature, the Hamiltonian that describes the system of two bosons in a (cubic) optical lattice is a two-species Bose-Hubbard Hamiltonian [125, 126, 127, 128]:

$$H = - \sum_{\sigma \langle i,j \rangle} J_{\sigma} \left( \hat{a}_{i\sigma}^{\dagger} \hat{a}_{j\sigma} + \hat{a}_{j\sigma}^{\dagger} \hat{a}_{i\sigma} \right) + \frac{1}{2} \sum_{\sigma i} U_{\sigma} \hat{n}_{i\sigma} (\hat{n}_{i\sigma} - 1) + V \sum_i \hat{n}_{iA} \hat{n}_{iB}, \quad (5.22)$$

where  $a_{\sigma}$  destroys a boson of species  $\sigma = A, B$ ,  $J_{\sigma}$  and  $U_{\sigma}$  are the single species tunneling and interaction energies (we assume repulsive interaction,  $U_{\sigma} > 0$ ) and  $V$  is the interspecies interaction term defined analogously

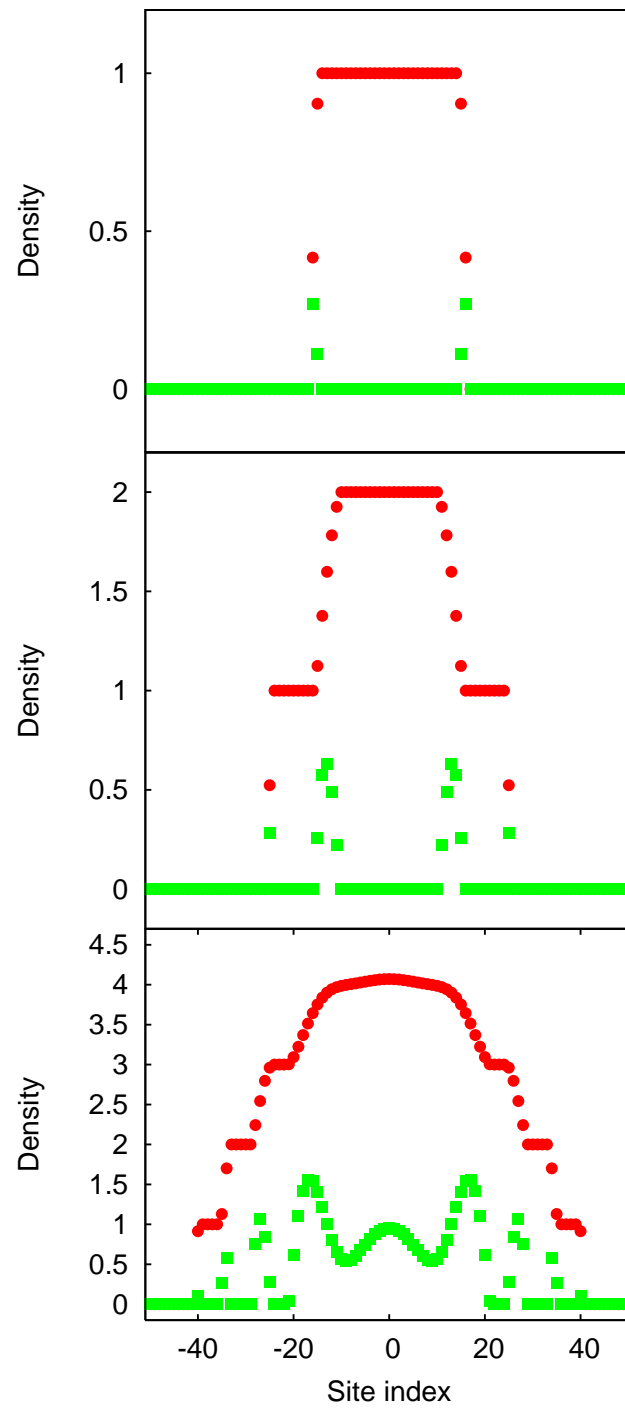


**Figure 5.5.** Mott domains for an inhomogeneous system for  $\mu = 0.2 E_{\text{rec}}$  (top),  $\mu = 0.5 E_{\text{rec}}$  (center) and  $\mu = 1.5 E_{\text{rec}}$  (bottom). Dots are the total density while squares indicates the superfluid density. For all the figures the lattice height is  $s = 18$  and the trap parameters are  $\omega_z = 2\pi 36.6 \text{ Hz}$  and  $\omega_{\perp} = 2\pi 208.2 \text{ Hz}$ .

to Eq. (5.10). The Hamiltonian (5.22) is a sum of two Hamiltonians like Eq. (5.8) and an interaction term given by

$$H_{\text{int}} = V \sum_i \hat{n}_{iA} \hat{n}_{iB}. \quad (5.23)$$

Similar to the case of only one species, in the limit of  $U_\sigma, V \gg t_\sigma$ , the Eq. (5.22) simplifies to a sum of single site Hamiltonians. We will now examine the different regimes: first the case in which the dominant term in Eq. (5.22) is the interspecies interaction and then those in which interspecies interaction is a perturbation and the total filling is commensurate with the number of lattice sites. Finally I will conclude commenting how the analysis for a homogeneous system can be extended to the inhomogeneous case which is the one relevant in the experiment due to the presence of the trapping potential.

### 5.3.1 Dominant interspecies interaction

Here I will consider the general case  $|V| \geq U_\sigma$  which attracted a limited theoretical attention but however is the pertinent case for the mixture  $^{41}\text{K}$ - $^{87}\text{Rb}$  at zero magnetic field. As we will see there is a conspicuous difference whether the interspecies interaction is attractive or repulsive.

#### Dominant attractive interspecies interaction

This case corresponds to  $|V| > U_\sigma$ ,  $V < 0$ . In this case we see that, similar to the case of the attractive Gross-Pitaevskii equation (see § 1.2.2), the spectrum of Eq. (5.22) becomes unbounded and the system collapses bringing all the particles in one site. This situation has not been explored in the literature and in particular there are no predictions for the case in which the attractive interspecies interaction is compensated by the repulsion of only one species, namely  $U_A < |V| < U_B$ .

#### Dominant repulsive interspecies interaction

This case was considered only recently for a 1D lattice in [129] and corresponds to  $V > U_\sigma$ . In this case, for incommensurate total filling, the system is found to be always superfluid, but there is a transition from a mixed double superfluid (2SF) to a phase separated superfluid (PSSF) for  $U_\sigma/J_\sigma > (U/J)_c$ . This phase separated superfluid is analogous to the weakly

separated uniform system that we considered in § 1.3: the two species arrange inside the lattice so to minimize the overlap and keep the total density constant. For the particular case  $n_A = 1$ ,  $n_B = 1/2$ ,  $U_A = U_B = U$ ,  $V = 1.05U$ , the critical value is found to be  $(U/J)_c \simeq 4$ .

On the other hand, for commensurate total filling, a phase transition toward a Mott state becomes possible. This phase separated Mott state (PSMI) has a gapped excitation spectrum and zero order parameter for each of the two species ( $\langle a_A \rangle = \langle a_B \rangle = 0$ ), but the density difference is correlated so that  $\langle (|n_A - n_B|) \rangle \neq 0$ . In [129] it is found a difference if the total filling is odd (through the particular case  $n_A = n_B = 1/2$ ,  $U_A = U_B = U$ ,  $V = 1.05U$ ) or even ( $n_A = n_B = 1$ ): in the first case there is a PSSF phase between the 2SF phase and the PSMI, while in the case of even total filling the transition to the PSMI phase occurs directly from the 2SF. In both case the transition toward the PSMI phase occurs at the critical value for a single species:  $(U/J)_c \simeq 5.7$ .

Particularly interesting from the theoretical point of view, is the case where  $V = U_A = U_B$ : in this case the complete  $SU(2)$  symmetry of the theory is restored and the system is expected to behave like a single species one since there is no distinction between inter- and intra-species interactions.

### 5.3.2 Commensurate total filling

I will now consider the case of a commensurate *total* filling in which the low-energy Hilbert space contains states with integer filling. Furthermore, having already discussed the case  $|V| > U_\sigma$ , from now on I will take  $|V| < U$ . This case is the most interesting since, in a homogeneous system, is the only one where a transition to a Mott insulating state is possible [129].

In this regime one can further distinguish the case of an even total filling  $2n_0$  (i.e.  $|n_A, n_B\rangle = |n_0, n_0\rangle$ ) and odd total filling  $2n_0 - 1$  (i.e.  $|n_0, n_0 - 1\rangle$  and  $|n_0 - 1, n_0\rangle$ ). Due to the symmetry of the interaction term Eq. (5.23), if  $U_A = U_B$  the odd-filled states are doubly degenerate and therefore the ground state of a  $M$ -sites lattice is  $2^M$ -fold degenerate. For  $n_0 > 0$ , this degeneracy is lifted by a non zero difference  $U_A - U_B$  which is likely to be present in an experiment with two species (and definitely is for the  $^{41}\text{K}$ - $^{87}\text{Rb}$  mixture), but in the case  $n_0 = 1$  the degeneracy is only lifted by the finite hopping  $J_\sigma$  which introduces fluctuations in the number of particle per site: it is worth noting that these fluctuations are important at the second order in  $J/U$  which means that simple mean field approaches are

bound to failure as in the single species case.

In principle one should also consider states in which  $|n_A - n_B| > 1$  like  $|0, 2\rangle$  or  $|1, 4\rangle$ , however, it is not difficult to show that, unless the difference  $|U_A - U_B|$  is huge, these state are higher in energy than those with  $|n_A - n_B| \leq 1$  [127].

### Even total filling

As we pointed out above, fluctuations induced by residual tunneling must be taken into account if one wants to isolate the phases of the system. This is clearly demonstrated in the analysis of [130, 131] which, due to the limit of mean field treatment, fails to predict the existence of phases that cannot be reduced to single-component states. To put it in another way, the mean field treatment is limited to phases in which either the two species are superfluid (2SF), one is superfluid and the other is Mott insulator (SF<sub>AB</sub> + MI<sub>BA</sub>) or the two species are Mott insulator (2MI). Beside these three different phases there are also two more phases in which the two order parameters  $\langle a_\sigma \rangle$  are zero but there is either a condensate of atom pairs (PSF, paired superfluid [126]) or a so called super-counter-fluid (SCF). The first one is analogue of a molecular condensate or a BCS superfluid and in the second one the currents of the two species are always in opposite directions and behave as superfluids [125, 126]. Formally the transition to PSF is characterized by the order parameter  $\langle a_A a_B \rangle$  and that to SCF phase by  $\langle a_A^\dagger a_B \rangle$ . I will sketch now the argument which establishes the existence of these two phases.

Let us consider the even-filling case with  $V < 0$  and exchange symmetry ( $U_A = U_B = U$  and  $J_A = J_B = J$ ). In this situation, if  $n_0 > 1$ , the natural point of view is that of atomic pairs: breaking a pair of atoms of different species involves creating an extra pair of atom of the same species at a cost of energy  $U > 0$ . Therefore the single particle tunneling is suppressed and the dominant term is the second order tunneling. If we take into account this second order process, the system is again described by an effective Bose-Hubbard model [126]

$$H_P = -\tilde{t} \sum_{\langle i,j \rangle} [(O_i^+ O_j^- + O_i^- O_j^+) + 2m_i m_j] + \gamma \sum_i m_i^2, \quad (5.24)$$

where  $O_i^+$  ( $O_i^-$ ) creates (destroys) a pair of atoms at site  $i$ ,  $m_i$  is the number of pairs at site  $i$  and  $\tilde{t}$  is the second order tunneling energy defined as  $2J^2/U$ . In the limit  $\gamma \gg \tilde{t}$  we know that the ground state of Eq. (5.24)

is a Mott insulator; we also know from previous section that as soon as  $\gamma < 0$  the system collapses: what we have to prove is that the system is somewhere superfluid. This will be by construction a PSF. In the limit  $n_0 = m \gg 1$ , for  $\tilde{t} \ll \gamma \ll m^2 \tilde{t}$  the system is stable against collapse and the extra kinetic energy given by the  $m_i m_j$  term overcomes the potential energy contribution which means that the system must be superfluid. This argument is confirmed by Monte Carlo simulations in 2D which show that a phase with  $\langle a_A a_B \rangle \neq 0$  exist for  $n_0 = 2$  already at  $\gamma = 10\tilde{t}$  [126].

As far as the SCF phase is concerned, the existence of this phase is demonstrated taking  $v = U - V > 0$  and going in the limit  $v \ll U$ . In this limit it become useful to introduce the *isospin* operators [125, 132, 127, 128]

$$\begin{aligned} S_i^z &= (\hat{n}_{iA} - \hat{n}_{iB})/2 \\ S_i^x &= (\hat{a}_{iA}^\dagger \hat{a}_{iB} + \hat{a}_{iB}^\dagger \hat{a}_{iA})/2 \\ S_i^y &= -i(\hat{a}_{iA}^\dagger \hat{a}_{iB} - \hat{a}_{iB}^\dagger \hat{a}_{iA})/2 \end{aligned} \quad (5.25)$$

which, in the approximation stated above and up to the second order in  $J/U$ , transform Eq. (5.22) into a Heisenberg model [125]

$$H_S = -2\tilde{t} \sum_{\langle i,j \rangle} \mathbf{S}_i \mathbf{S}_j + v \sum_i (S_i^z)^2. \quad (5.26)$$

This model, for  $v \ll U$ , exhibits a ground state in which the following order parameter is non-zero:  $\langle S_i^+ \rangle = \langle S_i^x + iS_i^y \rangle$ . This, using the definition Eq. (5.25) implies  $\langle a_A^\dagger a_B \rangle \neq 0$ , which is exactly the definition of supercounterflow: the key property of this state is that superfluidity is not found in each of the two species separately but instead in the correlated fluctuations of the two species. It can be viewed also as a double Mott insulator with superfluid behavior in the isospin sector.

One can at this point ask where the boundaries between all these phases are located and which is the nature of the corresponding phase transitions. One important help in this task comes from the demonstration that the 2SF-SCF transition is equivalent to the 2SF-PSF one: this can be understood by thinking SCF in terms of a PSF with a particle of species A and a hole of species B [133]. This means that the phase diagram is symmetric for  $|V| < U$  with respect to  $V = 0$ . The charting of the phase diagram for even filling factor is addressed in [126]: the authors find that the phase diagram depends on the asymmetry  $u = U_A - U_B$ . When  $u \neq 0$ , for small values of  $|V|$ , decreasing the tunneling one first crosses the transition from a 2SF to a  $SF_A + MI_B$  and then to the two-species Mott insulator 2MI. Opposite, for  $|V|$

only slightly lower than  $U$  there is first a phase transition from 2SF to PSF (or SCF, depending on the sign of  $V$ ) and then a phase transition to 2MI when second order tunneling is also suppressed. In the case of exact exchange symmetry obviously the transition to a mixed superfluid-insulating state is absent and the authors of [126] predict a single-species-like transition from a 2SF to a 2MI.

### Odd total filling

As we pointed out in the introduction, in the case of total filling of one particle per site, there is a degeneracy which is lifted only at the second order in  $J/U$ . Introducing the isospin operator Eq. (5.25) in the expansion of Eq. (5.22) up to order  $(J/U)^2$  one finds a anisotropic Heisenberg model [125, 127, 128]

$$H_{XXZ} = - \sum_{\langle i,j \rangle} [J_{\perp} (S_i^x S_j^x + S_i^y S_j^y) - J_z S_i^z S_j^z] - h \sum_i S_i^z, \quad (5.27)$$

where the coupling constants are given by

$$\begin{aligned} J_{\perp} &= 4 \frac{J_A J_B}{V} \\ J_z &= 2 \frac{J_A^2 + J_B^2}{V} - 4 \frac{J_A^2}{U_A} - 4 \frac{J_B^2}{U_B} \\ h &= 2 \left( \frac{J_A^2}{U_A} - \frac{J_B^2}{U_B} \right). \end{aligned} \quad (5.28)$$

It is worth noting that, opposite to Eq. (5.26), no approximation are required in the derivation of Eq. (5.27), but for the constraints  $n_A + n_B = 1$  and  $J_{\sigma}/U_{\sigma} \ll 1$ . One must remember however that for  $U_A = U_B = V$  ( $SU(2)$  limit) this perturbative approaches are no longer valid.

Eq. (5.27) admits three different phases characterized by different ordering in the isospin sector [132, 128]. A ferromagnetic phase which corresponds to the 2MI which is found for high enough  $V$ , an easy-plane phase which –as it is shown above for the isotropic case– corresponds to the SCF, and finally, for small values of  $V$  and close to the exchange symmetry, an antiferromagnetic phase which corresponds to a checkerboard solid. The transition from the different isospin phases can be understood from Eq. (5.27): the transition from ferromagnetic to the easy-plane is second order, while the transition from antiferromagnetic to easy-plane is first order; no direct transition is foreseen from antiferromagnetic to ferromagnetic [132, 128].

The “charge” sector of the theory, namely the transition from isospin order to superfluidity is much more complicated. In [127] the phase diagram is studied for exact symmetric one particle filling (i.e.  $n_A = n_B = 1/2$ ) and  $|U - V| \ll U$  where the isospin order is either antiferromagnetic or easy-plane. It is found that the transition to superfluid occurs for at the same values of  $J/U$  for the two species unless a strong imbalance between the two tunneling is introduced. Furthermore, the transition from checkerboard Mott to 2SF is first order and can show a hysteretic behavior, while the transition from SCF to 2SF is second order [127].

Similar calculations, but for  $n_A, n_B < 1$  and no constraint on  $U - V$  shows that in the limit of vanishing filling the transition is crossed with a depopulation of one species and thus is reminiscent of a PSSF, for intermediate filling the system is 2SF while, as the filling of the two species approaches one, as we discussed above, there is room for a mixed SF-MI phase [128]. However there is no direct transition from 2MI to 2SF which instead is easily found in a simple  $O(J/U)$  theory: the mechanism is first a second order transition to a depopulated phase or to a SCF and then another second order transition to a 2SF. Further details and Monte Carlo calculation of the isospin phase diagram can be found in [128].

The two approaches outlined above are both considering the case of a maximum filling of one per species: one can therefore ask if there are qualitative changes considering states with higher odd total filling (i.e.  $n_0 > 1$ ). It turns out that the only difference with respect to the  $n_0 = 1$  case is that the depopulated phase is changed into a true mixed SF-MI phase while the other feature of the phase diagram both in the isospin and in the “charge” sectors remain the same [128, 127].

### **5.3.3 The trapping potential**

The available theoretical works on this subject are either taken in the canonical ensemble for a uniform system [126, 127] or in the grand canonical ensemble with a uniform chemical potential [128]. Both these approaches are unsuitable to describe the trapping potential which is always present in actual experiments.

We know from § 5.2.3 that the trapping potential creates alternated domain of superfluid and Mott insulator which can be reproduced considering a “local” chemical potential. As it is pointed out in [128], the same mechanism is not guaranteed to work also in the case of two different species. On

the other hand number conservation is properly dealt with in the canonical ensemble but it is not even conceivable to reproduce experiment with a fixed integer filling and the phase diagram at constant incommensurate density is a featureless 2SF phase pretty much similar to the single-species case [129].

Facing the limits of the available theoretical work, an experiment devoted to this subject should go in two complementary directions: on one hand effort should be put to reduce the harmonic confinement and, by the same token, to decrease the maximum filling in the lattice to one or two where the comparison with theory is easier; on the other hand one should try to reduce the interspecies interaction in order to access a situation in which the isospin picture can be used to make predictions for the system.

Closely related to this issue one should also consider the problem of the finite temperature always present in this kind of experiment: the energy scale of the isospin-order has been shown to be that of the second order tunneling, namely  $J^2/U \ll J$ . The lowest temperature that can be achieved are generally between  $J$  and  $U$ : the issue of finite temperature should be therefore seriously considered in view of observing the different isospin ordered phases. I note however that the direct experimental observation of second order tunneling for a single species was recently reported in [134] proving that this energy scale is at least accessible at the state-of-the-art.

No matter which is the ultimate goal that one seeks in the experiment, the first fundamental step is the loading of a two superfluid mixture in a 3D optical lattice, a task which was never accomplished so far. In the next chapter we will report how this was achieved by our group and which is the physics that can be observed in the limit of  $J_A/U_A \gtrsim 0.01$ ,  $J_B/U_B \gtrsim 0.2$  and  $V > U_\sigma$ , where the system is predicted to be phase separated.

## Chapter 6

# Degenerate Bose-Bose mixture in a 3D optical lattice

There is a great satisfaction in building good tools for other people to use.

(Freeman Dyson)

In this chapter I report the main result of this thesis: the breakdown of superfluidity in a Bose-Einstein condensate in an optical lattice induced by the interaction with another superfluid with a much smaller population and an incomplete overlap. The observed phenomenology was unambiguously related to the interaction between the two condensates and trivial explanations such as heating during the loading of the lattice have been excluded. Yet, the explanation of the observed phenomenology is far from being entirely elucidated. Certainly our results closely resemble those obtained for a mixture of a Bose-Einstein condensate and a Fermi gas [135, 136] suggesting the existence of a possible common cause for the observed phenomenology. I will discuss these topics in § 6.4, but before describing in detail in § 6.3 the experimental results (submitted for publication and available as preprint [137]), I shall detail the experimental effort that was necessary to obtain these results.

The exploration of the new physics of two Bose-Einstein condensates in an optical lattice requires in fact two fundamental steps that, although they have been already reached separately, required a considerable work to be reproduced. First the realization of the double condensate and then the characterization of the transition from a superfluid to a Mott insulator with the  $^{87}\text{Rb}$  condensate alone.

## 6.1 A double condensate

The simultaneous condensation of  $^{41}\text{K}$  and  $^{87}\text{Rb}$  was obtained at LENS in 2002 [22] soon after the first realization of a  $^{41}\text{K}$  Bose-Einstein condensate by means of sympathetic cooling [16]. The main difficulty involved in this achievement is related to the huge value of the cross section of the two processes  $|\text{Rb}, 2, 1\rangle + |\text{K}, 2, 2\rangle \rightarrow |\text{Rb}, 1, 1\rangle + |\text{K}, 2, 2\rangle$  and  $|\text{Rb}, 2, 1\rangle + |\text{K}, 2, 2\rangle \rightarrow |\text{Rb}, 2, 2\rangle + |\text{K}, 1, 1\rangle$  [138]. Both these processes lead to a fast depletion of the K sample: the first by direct liberation of the  $^{87}\text{Rb}$  hyperfine energy and the second by producing the antitrapped  $|\text{K}, 1, 1\rangle$  state.

The  $|2, 1\rangle$  state is magnetically trappable and therefore atoms that are left in this state by unavoidable imperfections of the optical pumping stage are still present after the loading of the magnetic trap. In almost all the experiments focused on  $^{87}\text{Rb}$  alone, these atoms do not harm to the cold gas because they are promptly expelled by the radio-frequency cascade used for the evaporation. However, as it is shown in figure 2.14, in our experiment evaporation is performed along the  $|2, 2\rangle \rightarrow |1, 1\rangle$  microwave transition: this means that atoms in  $|2, 1\rangle$  state are only evaporated up to a much higher temperature and definitely are not removed from the trap.

When  $^{41}\text{K}$  is added however,  $^{87}\text{Rb}$  atoms in the unwanted state quickly disappear from the magnetic trap at the expense of roughly the same amount of K atoms. Since sympathetic cooling demands that  $N_K < N_{\text{Rb}}$  throughout the whole evaporation process, even if the fraction of the *initial* number of  $^{87}\text{Rb}$  atoms in the unwanted state is small, it might be enough to completely deplete the  $^{41}\text{K}$  sample<sup>1</sup>. We measured a lifetime of  $^{41}\text{K}$  atoms in the magnetic trap without an active clean of the  $^{87}\text{Rb}$  atoms as low as 19.6(1.4) s. Not surprisingly, the cleaning of these atoms was indeed a major technical advance toward the realization of the first double Bose-Einstein condensate [22].

In our experiment  $^{87}\text{Rb}$  atoms in the  $|2, 1\rangle$  state are removed from the trap in the following way. First two fast sweeps are done around the frequency of the  $|2, 1\rangle \rightarrow |1, 0\rangle$  transition: this does not affect the atoms in the  $|2, 2\rangle$  state while removes a substantial amount of unwanted atoms. However, as it is observed in several experiments, the unwanted state gets populated with a non zero rate during the evaporation procedure: to eliminate also these atoms, a weaker (−10 dB) sideband is generated from the

<sup>1</sup>Working with  $^{39}\text{K}$ , the cross section for these collisions is much smaller, and atoms in the  $|2, 1\rangle$  state represent only an extra burden on sympathetic cooling.

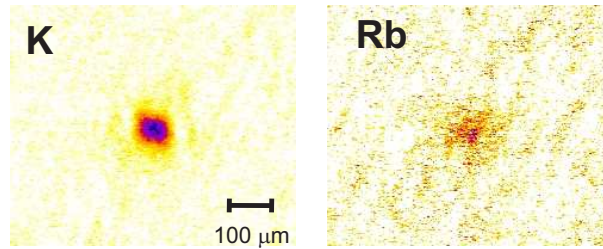


**Figure 6.1.** Absorption images of the  $^{87}\text{Rb}$  and  $^{41}\text{K}$  clouds taken from the vertical direction. A Bose-Einstein condensate of K is present and it contains around  $10 \times 10^3$  atoms, while the Rb sample was entirely evaporated and it is barely detectable.

main evaporation frequency and it is tuned across the above mentioned transition<sup>2</sup>. With this procedure the lifetime of the atomic sample is again of about 50 s and a significant amount of  $^{41}\text{K}$  survives until the end of the evaporation.

A careful balance is then required between the initial number of  $^{41}\text{K}$  and  $^{87}\text{Rb}$  present in the trap. In fact, if the number of  $^{87}\text{Rb}$  atoms is too high the cleaning procedure will not remove all the atoms in the  $|2, 2\rangle$  state before they can actually destroy the  $^{41}\text{K}$  sample. On the other hand, if the number of  $^{41}\text{K}$  atoms is too large, the thermal load on  $^{87}\text{Rb}$  will be too high and sympathetic cooling will not work until the formation of two condensates. This is illustrated in figure 6.1 in which we show two absorption images: a potassium condensate is formed while the rubidium sample is completely evaporated.

As we already pointed out in § 4.1, the precise tuning of the initial number of atoms is obtained in our experimental setup by changing the duration of the loading time of our 2D-MOT. This allows us to tune the number of atoms with the accuracy needed to reach the right balance to cool both species down to quantum degeneracy. In figure 6.2 I report two images showing that indeed the evaporation process proceeds as expected: in the first image evaporation of  $^{87}\text{Rb}$  is stopped at a temperature which is in between the critical temperature of potassium and that of rubidium. Temperature can be measured from the width of the  $^{87}\text{Rb}$  thermal component and we find  $T = 170(9)$  nK. This value is consistent with the one

<sup>2</sup>The sideband is generated in the following way. A BCO oscillator is locked to the 683<sup>th</sup> harmonic of a reference signal close to 10 MHz. By slowly modulating the reference it is possible to obtain a sweep of the output frequency: phase noise is largely amplified but the overall performance are sufficient for the cleaning task. The output of the BCO is fed into the main amplifier with a power combiner.

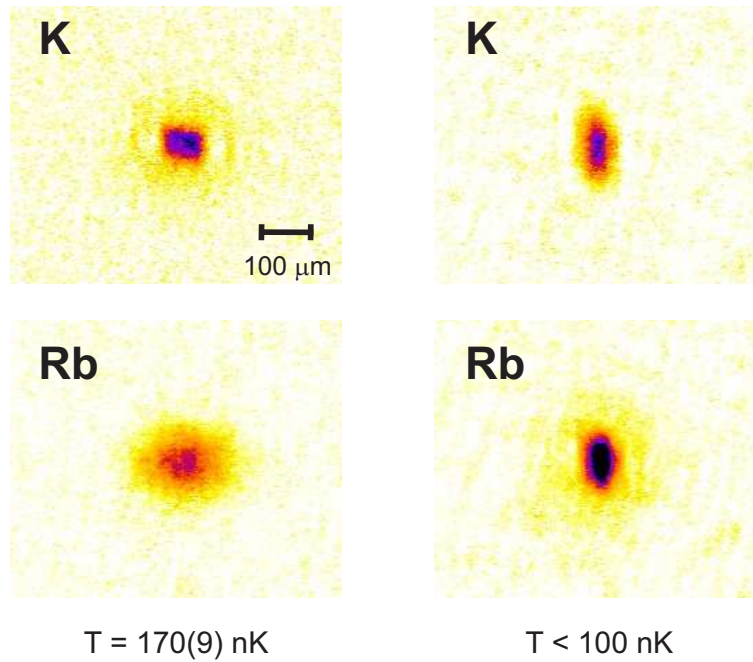


**Figure 6.2.** Absorption images of the two atomic species taken from above. Evaporation is stop respectively between the transition of K and that of Rb (left) and below both transitions (right). The number of atoms in the thermal components on the left parts are  $14.9 \times 10^3$  for  $^{41}\text{K}$  and  $25 \times 10^3$  for  $^{87}\text{Rb}$ . The  $^{41}\text{K}$  Bose-Einstein condensate on the left contains  $8.1 \times 10^3$  atoms while on the right picture the two Bose-Einstein condensates contain  $12.3 \times 10^3$  and  $17.3 \times 10^3$  atoms.

determined from the condensed fraction and the critical temperature of potassium using Eq. (1.23): we find  $T_c(\text{K}) = 190(20)$  nK and a condensed fraction of  $35(3)\%$  which gives  $T = 180(20)$  nK. At the same time it is also consistent with no discernible condensate of  $^{87}\text{Rb}$ : for the measured number of atoms the critical temperature is  $T_c(\text{Rb}) = 135(15)$  nK. In the second image reported in figure 6.2, two Bose-Einstein condensates can be seen: expansion time was increased to 20 ms to make more evident the inversion of the aspect ratio (§ 2.5). In this case temperature cannot be easily measured since no thermal fraction is detectable: we know that, for this number of atoms, this condition is reached for  $f_c \gtrsim 0.7$  and this allow us to set an upper bound for the temperature to  $T < 100$  nK.

As we have shown in § 1.3, one of the first issues when dealing of two Bose-Einstein condensates is their topology. In our system the direct observation of the topology is beyond the possibility of our imaging system, we have therefore to rely on simulation based on actual parameters. In figure 6.3 I report a section of the density distribution of the two species

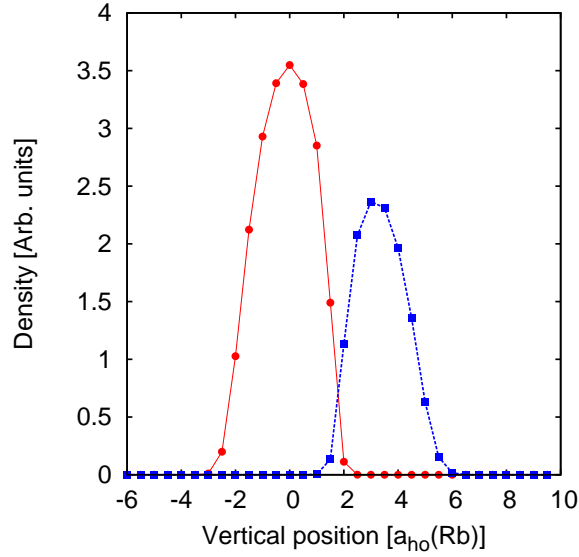


**Figure 6.3.** Density distribution of  $^{87}\text{Rb}$  (red dots) and  $^{41}\text{K}$  (blue squares) calculated with numerical integration of Eq. (1.37) for the numerical parameters of the actual experiment. The lengthscale is given by the harmonic oscillator length for  $^{87}\text{Rb}$  which is around  $1.14\ \mu\text{m}$ . The number of atoms for  $^{87}\text{Rb}$  ( $^{41}\text{K}$ ) is  $3 \times 10^4$  ( $2 \times 10^3$ )

obtained from the solution of the coupled Gross-Pitaevskii equations (1.37) with the parameters of the experiment. As we can see the overlap between the two cloud is very limited: this situation is not changed by the presence of the lattice and represents a limitation to the present experiments as we will see in 6.3.

Anyway, the control on the two transitions toward the quantum degenerate regime fulfills the first prerequisite to load the mixture in the optical lattice. I will now describe how the lattice is realized in the experiment.

## 6.2 A 3D optical lattice

### 6.2.1 The lattice laser

The optical lattice is realized in our experiment with an IPG fiber laser capable of delivering 20 W still maintaining a linewidth of about 100 kHz around a wavelength of 1064.0 nm.

At this frequency the fine structure separation between D1 and D2 lines becomes negligible with respect to the detuning from the lattice light. This separation is in fact  $\delta_{Rb} = 7.3\ \text{THz}$  and  $\delta_K = 1.3\ \text{THz}$  for Rb and K respec-

tively, while the detuning is typically on the order of 100 THz. With such a huge detuning, for linear polarization, Eq. (1.7) simplifies to the following expression<sup>3</sup>

$$U_{dip}(\mathbf{r}) = \frac{3\pi c^2}{2\omega_{12}^3} \frac{\Gamma}{\Delta} I(\mathbf{r}) \quad (6.1)$$

where the detuning  $\Delta$  is taken from the barycenter of the line at frequency  $\nu_{12} = \nu_2 + \delta/3 = \nu_1 - 2\delta/3$  and  $\omega_{12} = 2\pi\nu_{12}$ . With the values given above, the detuning with respect to our lattice laser for Rb (K) is about  $-105$  THz ( $-110$  THz) and the ratio  $\Gamma/\Delta$  is about  $57.1 \times 10^{-6}$  ( $56.4 \times 10^{-6}$ ). As we have shown in § 5, the natural unit to measure the lattice height is the recoil energy defined in Eq. (1.6): at the lattice wavelength the recoil frequency for  $^{87}\text{Rb}$  ( $^{41}\text{K}$ ) is 2.03 kHz (4.30 kHz). We can now establish one important feature that the  $^{87}\text{Rb}$ - $^{41}\text{K}$  mixture will exhibit in the optical lattice: for a given laser intensity the lattice height is weaker for  $^{41}\text{K}$  than for  $^{87}\text{Rb}$ . In particular the ratio between the  $s$  parameters, namely the height in recoil energy is given by

$$\frac{s_{Rb}}{s_K} = \left(\frac{\lambda_{Rb}}{\lambda_K}\right)^3 \frac{(\Gamma/\Delta)_{Rb}}{(\Gamma/\Delta)_K} \frac{\nu_{r,K}}{\nu_{r,Rb}} \simeq 1.05 \cdot 1.01 \cdot 2.15 \simeq 2.3 \quad (6.2)$$

and is almost entirely due to the mass difference similar to what happens to the trapping frequency of the magnetic potential. In the following we will almost exclusively make reference to the height of the optical potential for  $^{87}\text{Rb}$ : the corresponding height for  $^{41}\text{K}$  is then a factor 2.3 smaller.

## 6.2.2 Experimental setup

As it is explained in § 1.1.3, a 3D optical lattice requires three pairs of counterpropagating laser beams which must interfere only pairwise. This requirement cannot be fully satisfied with polarization for simple geometrical reasons and therefore a suitable frequency difference has to be introduced externally. In practice, a common solution that we adopted in our experiment is to apply a frequency shift to all the three pairs by means of three different AOM's. This gives us an independent control over the power of the different beams at the expense of a slightly distorted wavefront: in practice the aberration introduced by this distortion is negligible for the beam waists used in the experiment.

---

<sup>3</sup>Exact up to correction order  $(\delta/\Delta)^2$ .

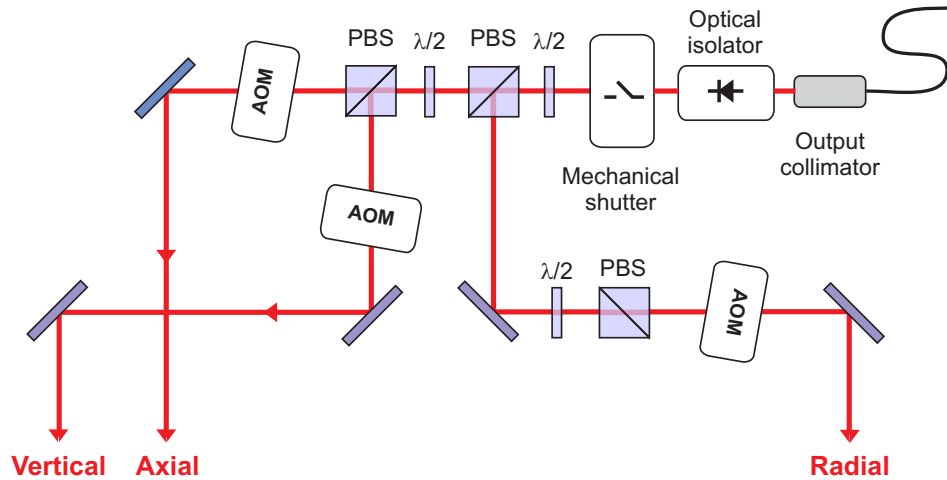


**Figure 6.4.** Scheme of the optics used for the optical lattice.

The layout of the three AOM's is shown in figure 6.4. The output of the laser is fed into a high power optical fiber with a pre-aligned output collimator which produces an output beam with a waist of 0.45 mm. Immediate after the collimator we placed a 60 dB optical isolator which is necessary since back reflection is intrinsic to an optical lattice design and our laser cannot withstand back reflection. After this isolator there is a mechanical shutter which provides a slow turn off of the beams: this allows us to keep the laser on during all the time thereby improving thermal stability and reducing power fluctuations. The shutter is built from a servo actuator which moves a mirror along the beam path: the stirred beam is then properly stopped. After the shutter a sequence of three  $\lambda/2$  waveplates and polarizing beam splitter cubes splits the power for the three beams which are injected into three different AOM's to introduce the appropriate detuning. Each of the three beams is then shaped with a sequence of three lenses: the resulting waists are  $90 \mu\text{m}$ ,  $180 \mu\text{m}$  and  $160 \mu\text{m}$  along the axial, vertical and radial direction respectively and are placed on the position of the magnetic trap to better than  $z_0$ . After the vacuum apparatus each of the beam is retroreflected with a cat-eye configuration to place the waist of the backward beam in the same position as the forward one and to reduce the effect of the misalignment of the retroreflecting mirror.

The coarse alignment of the lattice beam is done differently for the vertical and axial direction than for the radial. In the former directions alignment is done first by superimposing the lattice beams with the two imaging

beams and then taking an absorption image of the atoms inside the magnetic trap and superimposing a suitably attenuated image of the lattice beam on the position of the magnetic trap. For the radial direction since no imaging beam is available, we use a slightly different procedure: we use a guide beam tuned on resonance and align it on the magnetic trap maximizing the induced losses. Having done that the lattice beam is superimposed on the guide beam and a coarse alignment is achieved. This alignment is usually done once after any major change of the optical layout. More frequently a more careful alignment is employed in which first we realize a single beam optical trap with the axial beam: when the beam is properly aligned atoms are held against gravity with less laser power. For the radial and vertical direction, since a single beam trap is not deep enough due to the bigger waists of these two beams, we simply maximize the mechanical effect of the light on a crossed dipole trap: when a second beam is correctly aligned the trap size is minimum.

The finest alignment of the lattice is done during the calibration of the lattice height: in fact it is easy to see that, for a given total intensity, the height of the optical lattice is maximum when the two beams are perfectly counterpropagating. I will now describe the two techniques that we employ to do this calibration.

### 6.2.3 Lattice calibration

The main tool for lattice calibration is an atomic interferometric technique: the atomic diffraction in the thin-grating (Raman-Nath) regime.

Consider a standing wave potential of the form  $U(x) = s E_{\text{rec}} \cos^2(kx)$ : an atomic wavepacket which can be treated as a plain wave with momentum  $p_0$  ( $\Delta p \ll \hbar k \Rightarrow \Delta z \gg \lambda/2$ ), is coupled by the standing wave to plain waves with momentum  $p_0 \pm 2n \hbar k$ , where  $n$  is an integer number. If we now apply the standing wave only for a limited time  $T$  we can ask which is the probability of finding the atoms in the  $n^{\text{th}}$  plane wave. The calculation is straightforward if one can neglect the motion of the atomic center of mass along the lattice during the time  $T$ : in this case one is in the so-called atomic Kapitza-Dirac regime, corresponding to the Raman-Nath light diffraction from a thin grating and the probability is given by [139]

$$\wp(n) = \left| J_n \left( \frac{s}{2} \omega_{\text{rec}} T \right) \right|^2. \quad (6.3)$$

The thin grating approximation requires that the kinetic energy of the

involved plane wave is small with respect to the height of the optical potential. Taking as  $n_c$  the biggest significant order of diffraction and neglecting the initial momentum  $p_0$ , one has that the thin grating condition is equivalent to

$$\frac{(2n_c \hbar k)^2}{2m} \ll s E_{\text{rec}} \Rightarrow 4n_c^2 \ll s.$$

An estimation of  $n_c$  can be done remembering that  $|J_n(z)|^2 \ll 1$  if  $|z| < n$ : this means that

$$n_c \simeq \frac{s}{2} \omega_{\text{rec}} T.$$

With this estimation we can say that the thin grating approximation is equivalent to the following condition

$$s \omega_{\text{rec}}^2 T^2 \ll 1. \tag{6.4}$$

From this expression one sees that, for this technique to be useful for values of  $s > 1$ , one needs to apply the standing wave for a very short time  $T \ll \nu_{\text{rec}}^{-1} \sim 1$  ms.

### Raman-Nath diffraction of a Bose-Einstein condensate

If we now consider a more realistic situation in which the atomic plane wave is replaced by a Bose-Einstein condensate one can follow the same reasoning as above: the condensate get diffracted by the laser standing wave and atomic wavepackets with momenta spaced by  $2\hbar k$  are generated. These packets can be directly seen after the expansion as it is clearly shown in figure 6.5. More quantitatively, if we indicate the condensate wavefunction as  $\psi_0(x)$ , the wave function after the interaction with the lattice in the thin grating approximation is given by

$$\psi_T(x) = \sum_n i^n J_n \left( \frac{s}{2} \omega_{\text{rec}} T \right) e^{-2inkx} \psi_0(x).$$

The corresponding momentum distribution is obtained with a simple Fourier transform

$$\tilde{\psi}_T(p) = \sum_n i^n J_n \left( \frac{s}{2} \omega_{\text{rec}} T \right) \tilde{\psi}_0(p - 2n\hbar k). \tag{6.5}$$

With the assumption that  $\psi_0(x)$  extends over many lattice sites and therefore  $\tilde{\psi}_0(p)$  is narrow on the scale of  $\hbar k$ , it is possible to write the second moment of the momentum distribution as

$$\langle p^2 \rangle = \sum_n \wp(n) \int_{BZ} (q - 2n\hbar k)^2 |\tilde{\psi}_0(q)|^2 dq = \left( \sum_n \wp(n) \right) \langle p^2 \rangle_0 + 4\hbar^2 k^2 \left( \sum_n n^2 \wp(n) \right),$$

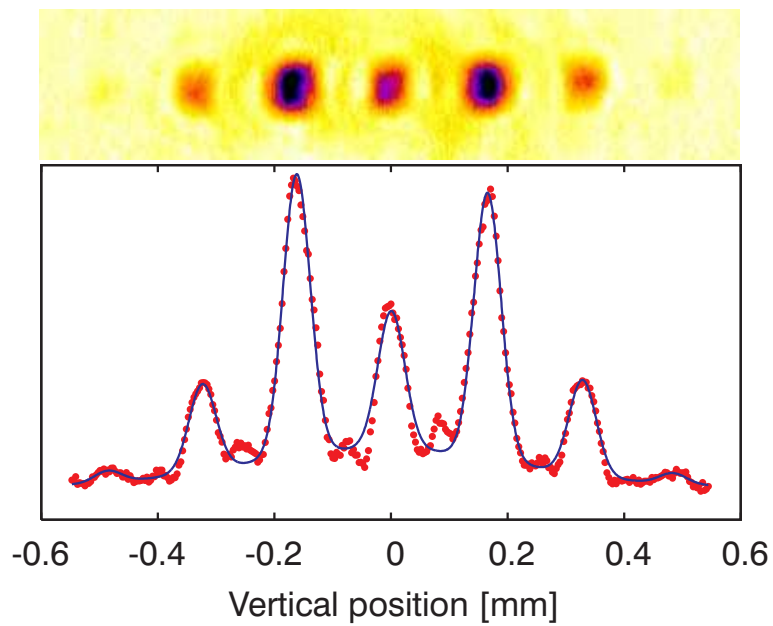


**Figure 6.5.** Atomic diffraction by a standing wave in the Raman-Nath regime. In the upper part an absorption image is shown after a 15 ms expansion: up to three order of diffraction can be seen. In the bottom part we show the density profile integrated along the  $y$  axis of the image: the fit is a sum of seven Gaussian peaks with the same width (see Eq. (6.5)) and a broad Gaussian background. The interaction time with the laser standing wave is  $T = 5\mu\text{s}$ .

where we indicate with  $\langle p^2 \rangle_0$  the second moment of the momentum distribution of the trapped condensate. Using Eq. (6.3) and the sum rules for the Bessel function one finds

$$\langle p^2 \rangle = \langle p^2 \rangle_0 + \frac{1}{2} (\hbar k)^2 (s \omega_{\text{rec}} T)^2. \quad (6.6)$$

This quantity is simply proportional to the RMS width of the cloud after expansion provided that the original size in the trap can be neglected and that the atomic interactions play a negligible role during the expansion: in these approximation we have

$$\sigma_{rms}^2 = \frac{t_{exp}}{m} \langle p^2 \rangle = \left( \sigma_0^2 + \frac{1}{2} (v_{\text{rec}} t_{exp})^2 (\omega_{\text{rec}} T)^2 s^2 \right). \quad (6.7)$$

This equation relates the  $s$  parameter and the expanded RMS size of the condensate.

The experimental procedure is very simple: the condensate is prepared in the magnetic trap and then we let it expand for one millisecond before turning on the lattice for a time  $T = 5 \mu\text{s}$ . After this time the cloud is let expand for  $t_{exp} = 15 \text{ms}$  and imaged with the usual procedure. Typical images are like that shown in figure 6.5: first and second moment of the optical density distribution are computed together with the width of the central peak  $\sigma_0$  and from the solution of Eq. (6.7) one obtains the lattice height. A comparison of this method with a complete fit based on Bessel function shows that the calibration is correct within 10%: for example from the height of the peaks of figure 6.5 one obtains in arbitrary units  $\wp(0, 1, 2, 3) = \{19.6, 39.0, 13.0, 1.6\}$  which can be fitted by  $s \omega_{\text{rec}} T = 3.68$  or  $s = 53$ ; from the same picture one has  $\sigma_0 = 13 \mu\text{m}$  and  $\sigma_{rms} = 102 \mu\text{m}$  which give  $s = 58$ .

This calibration requires in principle only a single image and it is therefore very helpful for the daily alignment of the lattice, furthermore it allows us to evaluate the balance of the lattice height along the different directions. To do this we shine all the three standing waves and image simultaneously both direction on separate regions of the CCD: a typical result is shown in figure 6.6. From the relative weight of the first order diffraction peaks it is possible to evaluate the balance of the heights of the three orthogonal lattice which is very important in order compare the experimental results with the theory.

Two different systematic errors can affect this kind of measurements: the first one is purely technical and it is related to the temporal profile of

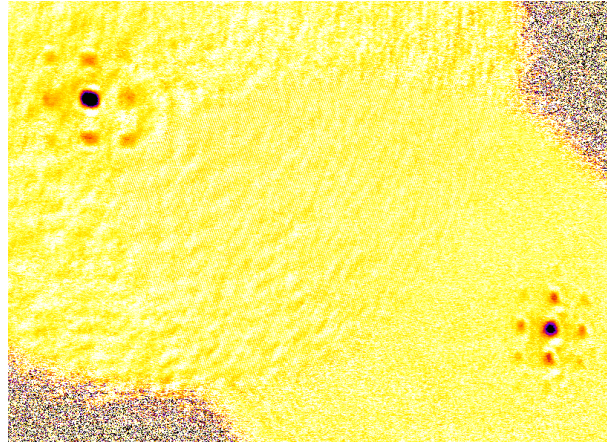


**Figure 6.6.** Atomic Raman-Nath diffraction from three orthogonal standing waves obtained with a pulse duration of  $5 \mu\text{s}$ : the number of atoms in the condensate is around  $10^5$ .

the pulse used to induce diffraction. The phase of the Bessel functions appearing in Eq. (6.5) has that simple form only for a rectangular pulse: in our case, for a  $5 \mu\text{s}$  pulse the turn on of the AOM introduces a rounder shape which causes an underestimate of the actual lattice height. This can be compensated for by introducing an appropriate correction factor into Eq. (6.7). The second systematic source of error is more fundamental and it is given by the atomic interactions. If we apply the pulse of the laser standing wave when atoms are still trapped or anyway too dense, the different momentum components can undergo  $s$ -wave collisions which will reduce the diffraction efficiency: this effect is more severe in the axial direction for which the trapped size is bigger. In this case the physical separation of the different components takes more time and the number of collision is bigger. To avoid this effect, we normally apply the pulse only after 1 ms expansion: during this time the atoms fall by less than  $5 \mu\text{m}$  and therefore experience the same optical lattice as in the trap position, but have a lower density and therefore interactions become negligible. To further test systematics of our calibration we compared the results of the Raman-Nath diffraction with another interferometric technique.

### **Bragg scattering of a Bose-Einstein condensate**

This second technique used for lattice calibration is based on the so-called atomic Bragg diffraction [140, 141, 142]. As the name suggests this technique is reminiscent of the Bragg scattering of neutron from a material

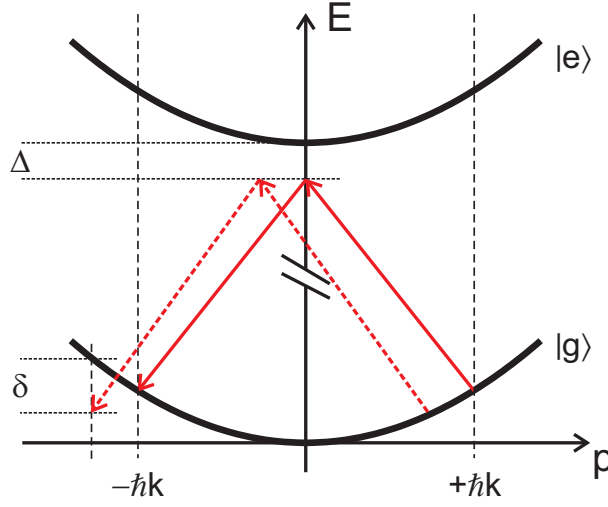


**Figure 6.7.** Scheme of the Bragg scattering two-photon transition. Continuous arrow mark the resonant process, while the two photon transition marked by the dashed line is allowed by the Heisenberg principle only if  $\delta < \hbar/T$ , where  $T$  is the duration of the lattice pulse.

crystal.

Consider a Bose-Einstein condensate in motion with velocity  $v$ : if we shine on it a pulse of the two counterpropagating beams that create the lattice, the atoms can absorb a photon from one of the beams and undergo stimulated emission by the other beam. This two-photon process is summarized in figure 6.7: if the initial momentum of the condensate is  $\hbar k$  the shown sequence transfers the atom into the  $-\hbar k$  state conserving both momentum and energy. The two populations undergo a two-photon Rabi oscillation at a frequency given by

$$\Omega_B = \frac{\Omega_0^2}{2\Delta}. \quad (6.8)$$

This Rabi frequency can be related to the height of the lattice by noting that Eq. (6.1) can be casted in the form

$$U_{dip}(\mathbf{r}) = \frac{\hbar\Omega(\mathbf{r})^2}{\Delta},$$

where  $\Omega(0) = \Omega_0$ . We then obtain

$$U_{dip} = 2\hbar\Omega_B \Rightarrow s = \frac{2\Omega_B}{\omega_{rec}}. \quad (6.9)$$

If the initial velocity of the atom is different from  $\hbar k$  *a priori* it is not possible to satisfy energy and momentum conservation, however if the standing wave is pulsed for a time  $T$ , the Heisenberg principle allows an energy

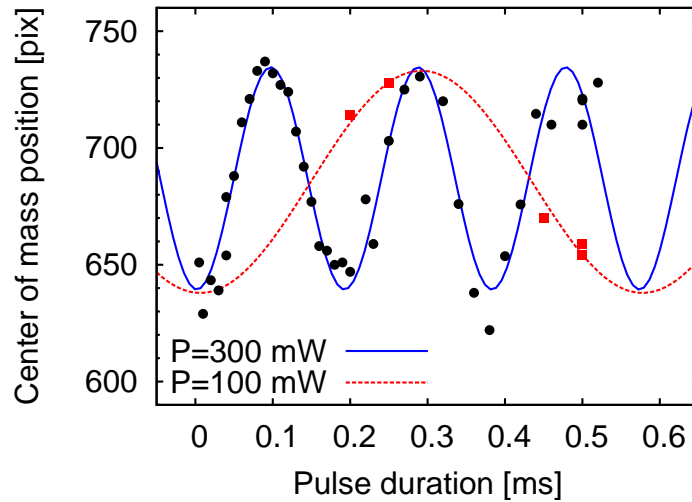


**Figure 6.8.** Oscillation of the center of mass position of the two momentum components created by Bragg diffraction of a condensate induced by the axial beam for two different lattice powers (dots and squares). From the sinusoidal fit to the higher power case (continuous line) we obtain a frequency  $\omega_B = 5.25(5)$  kHz which gives  $s = 5.3$ . In the fit of the lower power data, the frequency is fixed to one third of the previous value showing that data follow the expected scaling.

difference on the order of  $\hbar/T$ : for  $T \lesssim 1$  ms this means an energy width of about  $\Delta E \simeq \hbar 1 \text{ kHz} \simeq E_{\text{rec}}$  and therefore it is possible to observe Bragg oscillation for almost every initial momentum. The only consequence is that the amplitude of oscillation is reduced, i.e. it is not possible to transfer all the initial population.

The experimental procedure to observe Bragg oscillation is the following: for the radial and axial directions the condensate is set in motion by displacing the center of the trap inducing dipole oscillations. When the condensate has the desired velocity the magnetic trap is switched off and within  $200 \mu\text{s}$  the pulse of the lattice light is applied. For the vertical direction the trap is simply switched off and when the atoms have acquired the right velocity by the effect of gravity, the pulse is applied. The two momentum components are allowed to separate by the expansion and the center of mass of the two clouds is measured from the absorption imaging: fitting the oscillation of the c.o.m. as a function of the pulse duration one obtains  $\omega_B$  and hence  $s$ . A typical experimental acquisition is shown in figure 6.8.

### 6.2.4 Loading of $^{87}\text{Rb}$ in the lattice

The process of loading a Bose-Einstein condensate into an optical lattice can be viewed as an adiabatic transfer between the unperturbed condensate and the ground state of the first Bloch band which is the one with zero quasimomentum<sup>4</sup>. The condition on the ramping speed of the lattice that must be fulfilled in order to perform an adiabatic transformation can be derived from the usual adiabatic criterion

$$|\langle u | \partial_t H | w \rangle| \ll \frac{(E_u - E_w)^2}{\hbar} \quad (6.10)$$

where  $|w\rangle$  is the state that one wants to populate and  $|u\rangle$  is the state to avoid nearest in energy. In our case we have that these two states are respectively the Bloch waves  $|0,0\rangle$  and  $|1,0\rangle$  and the criterion (6.10), for  $s \sim 1$  is equivalent to [143]

$$\dot{s} \ll 32\sqrt{2}\omega_{\text{rec}} \sim 580 \text{ ms}^{-1} \quad (6.11)$$

and is even less stringent for  $s \gg 1$ : this requirement is easily fulfilled at all values of  $s$  and, as far as a homogeneous system is concerned, it is the only relevant criterion for adiabaticity. However, for an inhomogeneous system a more stringent criterion is set by the atomic dynamics time scale. Changing the trapping potential in fact requires a change in the density distribution in order to conserve entropy and to adjust with the compression originated by the red detuned lattice beams (see Eq. (1.18)). The relevant timescale of this process is given by the tunneling time  $\hbar/J$  which, as we have seen in 5.2.1, becomes exponentially small with increasing  $s$ . This leads in principle to a difficult condition in which increasing the lattice height demands an increased density redistribution which however occurs at a slower rate. In practice, for deep lattices, the compression induced by the beam is compensated by the increase in the on-site repulsive interaction and therefore a density change is no longer necessary, at least for a 3D lattice [144]. This criterion is therefore relevant only at intermediate lattice depth where the compression is still dominating.

For this reason we ramp up the lattice intensity with an exponentially growing profile depicted in figure 6.9. In principle the slowest the ramp the best the adiabaticity is, however several technical reasons, chiefly the decoherence associated with mechanical noise on the optics, limit the lifetime of

<sup>4</sup>Clearly this is no longer true if the condensate and the lattice have a non-zero relative velocity.

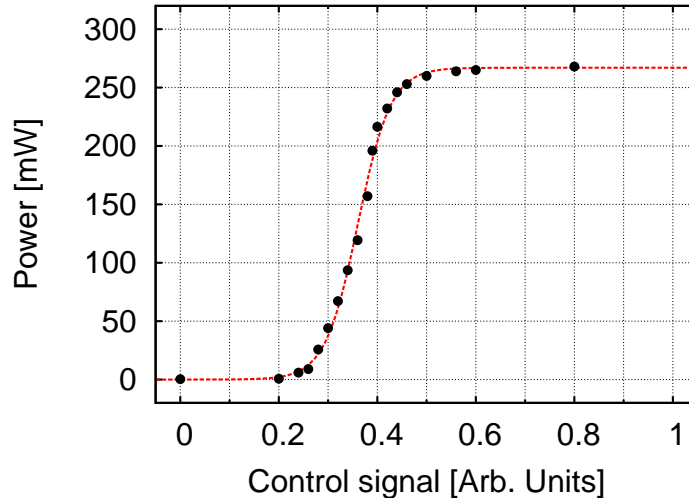


**Figure 6.9.** Typical profile of the ramp-up of the intensity of a lattice beam as a function of the control signal: a linear ramp in the control signal is converted in a smooth one both at the beginning and at the end of the ramp. The dashed line is a fit to a step function.

the sample and increase the heating. For high lattices this heating will ultimately introduce a dephasing among the different lattice sites which would destroy the superfluidity in the system. The ramp parameters are therefore chosen as a careful compromise to ensure adiabaticity and to avoid unwanted heating in the system. The optimization of the ramp parameters is done by ramping up and down the lattice with the same ramp under test: if the ramp is adiabatic the condensate is recovered in its Thomas-Fermi ground state, if the ramp is too fast excitations are visible, mostly as excitation of the surface modes of the condensate. We found that a good compromise, for a broad range of lattice heights, in presence of  $^{87}\text{Rb}$  alone, is given by a ramp duration of 50 ms with a time constant  $\tau_R = 20$  ms.

### 6.3 Experimental results

In this section I will present our experimental results obtained loading the mixture in the optical lattice. The reported experiments are a première in this line and –as we will see– are not fully understood yet. As a first characterization of the experiment I will report first our results on the superfluid to Mott insulator transition in  $^{87}\text{Rb}$  and then I will describe what happen when the second species is added. The chosen regime is that where the  $^{41}\text{K}$  Bose-Einstein condensate acts as a small perturbation on  $^{87}\text{Rb}$ : nev-

ertheless we will show that such a perturbation induces a loss of phase coherence in the  $^{87}\text{Rb}$  condensate at significantly lower lattice heights than in the unperturbed case. I will show that this effect is related to the small overlap of the two condensates and disappears if the two are far apart one respect to the other. I will also exclude the most trivial explanations related to the thermal fraction of the two gases and to the lattice ramp-up time. The tentative explanations for the observation reported here are explored in the next section.

### **6.3.1 The superfluid to Mott insulator transition in $^{87}\text{Rb}$**

The first observation of the superfluid to Mott insulator transition in an atomic gas was made in [6] where M. Greiner and co-workers observed a strong change in the density profile of the condensate after expansion as a function of the lattice height.

Their results were reproduced in our experiment and are shown in figure 6.10. Qualitatively as the lattice height is increased, the coherence between the different sites (typically, our  $^{87}\text{Rb}$  condensate occupies  $1.5 \times 10^4$  lattice sites) give rise to a matter wave interference which is visible after the expansion. This interferogram becomes more and more visible as lattice height is increased until, for a certain value of the lattice height, the contrast starts to decrease and eventually disappears leaving a Gaussian shaped cloud.

The experimental procedure we used to obtain these results is the following: after adiabatically loading the atoms in the lattice with the ramp illustrated in figure 6.9, we wait for 5 ms with the optical lattice at full power and abruptly switch off the lattice beams ( $< 1 \mu\text{s}$ ) and the magnetic trap ( $\sim 100 \mu\text{s}$ ). Then, after a time-of-flight of 20 ms, we make the usual absorption image.

The relation between the loss of interference and the superfluid to Mott insulator phase transition is established noting that this loss is reversible: the coherence can be recovered if the lattice height is ramped down again. Further properties can be extracted with a more quantitative analysis. As we already pointed out in § 6.2.3, the density profile after expansion is related to the momentum distribution which, for the lowest Bloch wave, is given by Eq. (5.15). The transformation from the post-expansion density

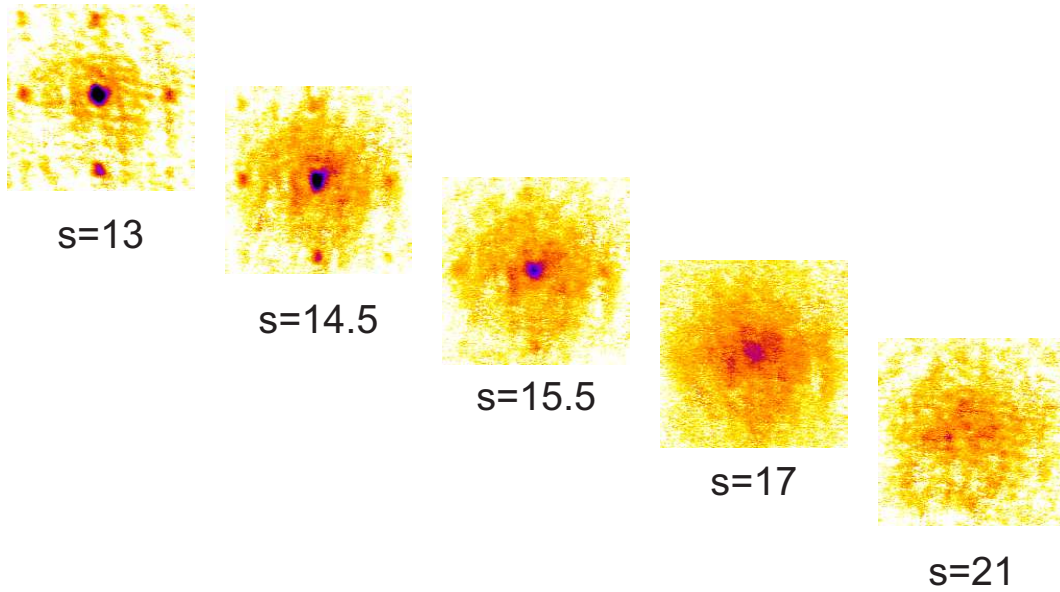


**Figure 6.10.** Absorption images taken with  $^{87}\text{Rb}$  alone at different lattice heights. The contrast of the interference pattern is reducing as lattice height increases.

profile to the momentum distribution is simply given by:

$$n_e(\mathbf{x}) = k_e^6 \left| \tilde{w}(k_e^2 \mathbf{x}) \right|^2 \sum_{i,j} \exp(i k_e^2 \mathbf{x}(\mathbf{r}_i - \mathbf{r}_j)) \langle \hat{a}_i \hat{a}_j \rangle, \quad (6.12)$$

where the scaling factor  $k_e$  depends from the expansion time  $t_e$  as  $k_e^2 = m/(\hbar t_e)$ .

From the above expression we can understand the physics behind figure 6.10. The peaks are in fact the Bragg peaks corresponding to the reciprocal lattice as it can be immediately recognized looking at figure 5.1. The smearing of the peaks is associated to the reduction of the coherence length of the sample with a persisting short range correlation and, when the peaks completely disappear, the remaining Gaussian background is the Fourier transform of the single-site Wannier function.

A more quantitative analysis of the phase coherence of the system across the phase transition can be done by measuring the visibility of the interference pattern [117]. In principle one could fit the image to Eq. (6.12) and extract all the information. This method suffers of a poor accuracy when the peaks start to be smeared because a fitting of separate sharp peaks is not possible. A more robust procedure, introduced in [117], is depicted in figure 6.11: first we perform a sum over four small  $3 \times 3$  pixel window around the first order Bragg peaks that we call  $S_{90}$ , then we repeat

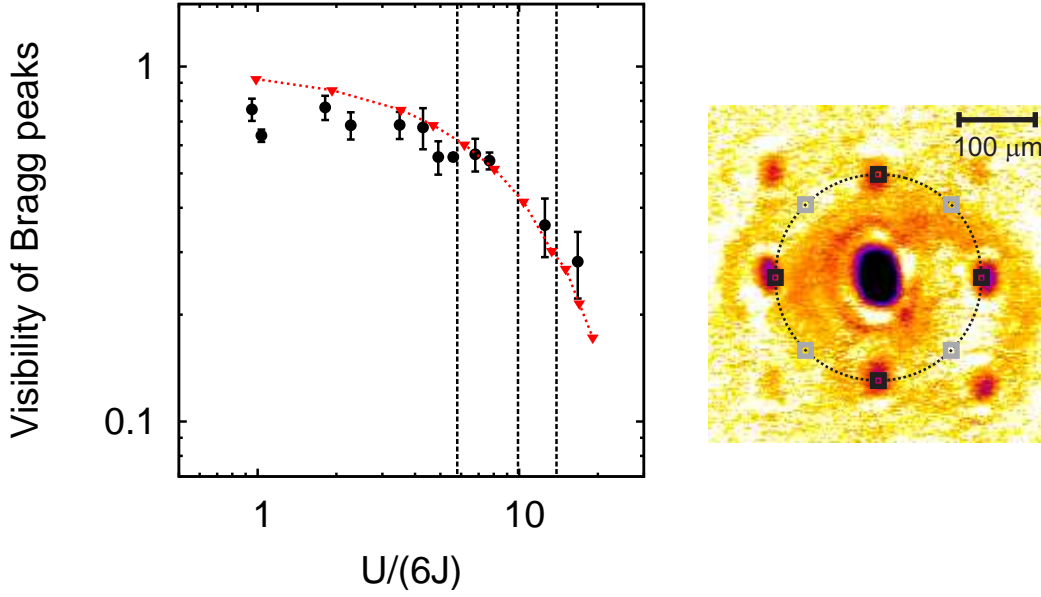


**Figure 6.11.** (Left) Visibility of the Bragg peaks as a function of the adimensional parameter  $U/(6J)$ . The parameter is calculated from Eq. (5.12) with the measured lattice height and the error bars are statistical fluctuation over around 5 measures. The vertical lines mark the expected value for the formation of the first three Mott lobes. Experimental results are compared with the superfluid fraction computed within the site decoupling approximation (red triangles). (Right) Procedure to compute the visibility according to Eq. (6.13): the black squares are used to compute  $S_{90}$  and the gray one to compute  $S_{45}$

the same procedure on another four windows offset by  $45^\circ$  and obtain  $S_{45}$ . From these two quantities we construct a measure of the visibility as

$$v = \frac{S_{90} - S_{45}}{S_{90} + S_{45}} : \quad (6.13)$$

in this way the contribution of the background cancels regardless of the quality of the peaks themselves. The resulting plot of this quantity is shown in figure 6.11: indeed the visibility is almost constant up to a value  $U/(6J) \simeq 6$ , where it begins to drop. The results are compared with the simple model outlined in § 5.2.3: the superfluid fraction defined as  $\sum_i |\psi_i|^2 / N$  closely follows the behavior of the measured visibility.

Another observable which reflects the transition from superfluid to Mott insulator is the width of the  $k = 0$  Bragg peak which measures the coherence length of the system. This quantity is plot in figure 6.12: as we see the width shrinks for increasing lattice height and then has a steep climb around  $U/(6J) \simeq 6$ .

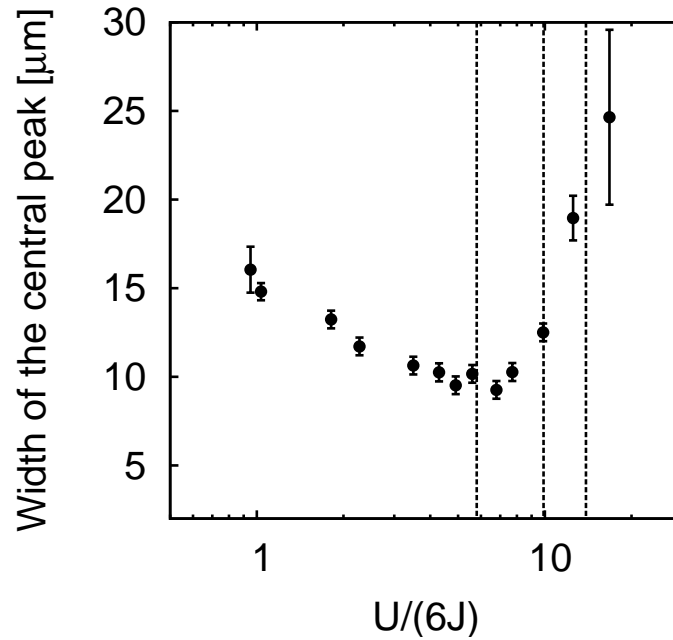


**Figure 6.12.** Width of the zero momentum peak as a function of the adimensional parameter  $U/(6J)$ .

These results show that we can experimentally probe the loss of phase coherence associated to the phase transition from a Bose-Einstein condensate to a Mott insulator and it nicely fits with the prediction based on the Bose-Hubbard model. We are therefore in the position to see how this dynamics is changed by the interaction with another superfluid.

### 6.3.2 Adding the second species

As we pointed out in the introduction to this chapter, the main experimental result of this work is the observation that the lattice strength at which the contrast of the  $^{87}\text{Rb}$  Bragg peaks starts to decrease is largely shifted not only by a minor admixture of  $^{41}\text{K}$  atoms, but also with a marginal spatial overlap.

The experimental procedure adopted is straightforward: first the two condensates are produced as explained in § 6.1 and then the lattice is ramped up at different heights as we have done for the experiment of § 6.3.1. In order to explore a regime in which the second superfluid acts as a perturbation on the first, the number of K atoms is limited to  $N_K = 2(1) \times 10^3$ , less than 10% of the  $^{87}\text{Rb}$  condensate size. The typical number

of  $^{87}\text{Rb}$  atoms in the condensate is  $N_{\text{Rb}} = 3(1) \times 10^4$ . In order to exclude any effect due to the residual thermal fraction and to set stage for further analysis, it is important to give an estimate of the initial temperature before the ramp-up of the lattice. In our case, an estimation can be obtained by noting that, in the presence of potassium, we cannot distinguish any thermal fraction of the  $^{41}\text{K}$  condensate. For  $N_{\text{K}} \simeq 2 \times 10^3$  this means that the condensed fraction is above 50%. Since the condensed fraction scales as

$$\frac{N_0}{N} \simeq 1 - \left(\frac{T}{T_c}\right)^3,$$

we can estimate that the temperature of the mixture is below 73 nK: at this temperature the corresponding condensed fraction of  $^{87}\text{Rb}$  is 83%.

The visibility of the Bragg peaks of  $^{87}\text{Rb}$  in presence of a small  $^{41}\text{K}$  condensate is plotted in the top part of figure 6.13, while the width of the zero momentum peak is reported in the bottom part. To ease the comparison with the case of  $^{87}\text{Rb}$  alone the corresponding data are also plot. As anticipated the visibility starts to decrease for a much weaker lattice and at the same value of lattice height the width of the central peak has a steep climb. To make the effect more evident, the results with two species are plotted as a function of the height of the  $^{87}\text{Rb}$  lattice  $s$  instead of the parameter  $U/(6J)$ . The relation between the two horizontal scales is given by Eq. (5.12).

Quantitatively, we characterized the loss of visibility fitting the data with a phenomenological Fermi function:

$$v = v_0 (1 + \exp(\alpha(s - s_c)))^{-1}. \quad (6.14)$$

This function has the expected flat behavior below the critical height  $s_c$  and then decays as  $\exp(-\alpha s)$  for  $s \gg s_c$ . Note that there is no direct link between the fitted  $s_c$  and  $(U/(6J))_c$ , but we expect that the  $[U/(6J)]_{s=s_c}$  is close to it. From the fits displayed in figure 6.13(top), we obtained the following value for  $s_c$ :

$$\begin{aligned} s_{c0} &= 17.1(0.6)(1.7) & s_{c1} &= 12.8(0.3)(1.3) \\ \alpha_0 &= 0.36(7) & \alpha_1 &= 0.71(8) \end{aligned}$$

where the first error is the statistical contribution of the fit and the second is the systematic uncertainty associated with the lattice calibration that does not affect the difference of the two value which is clearly not compatible with zero.

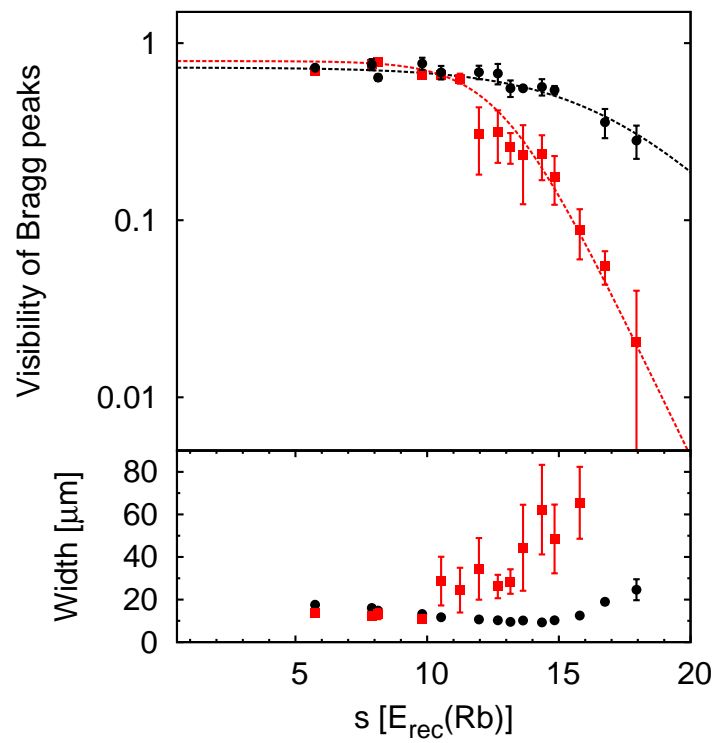


**Figure 6.13.** Visibility of the Bragg peaks of  $^{87}\text{Rb}$  as a function of  $s$  with (squares) and without (dots)  $^{41}\text{K}$ . Error bars are statistical fluctuation over around 5 measures. Dashed line are a fit according to Eq. (6.14).

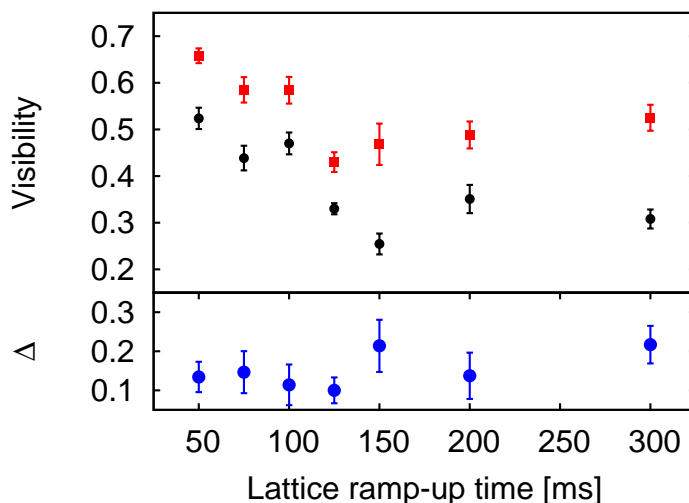


**Figure 6.14.** Measured visibility of  $^{87}\text{Rb}$  as a function of the duration of the ramp-up of the lattice with (squares) and without (dots)  $^{41}\text{K}$ . For all the measurements the ramp as the shape of figure 2.15 with a time constant equal to 0.4 the ramp time. The bottom panel shows the difference between the values with and without  $^{41}\text{K}$ .

According to Eq. (6.2), the corresponding height of the lattice for  $^{41}\text{K}$  is a factor 2.3 smaller and the sample is always deep into the superfluid phase. This, combined with the small number of atoms, makes the detection of the Bragg peaks of K very difficult: the zero momentum peak is however always visible and shows no broadening. Together with the appearance of weak Bragg peaks in the best pictures, this is an indication that no heating takes place during the ramping up of the lattice. This indication is further confirmed by an analysis of the visibility of the  $^{87}\text{Rb}$  peaks as a function of the ramping time with and without  $^{41}\text{K}$ , which is reported in figure 6.14. As we can see, although systematically smaller, the change in the visibility is the same with or without  $^{41}\text{K}$  establishing that the adiabaticity in the loading of the lattice is not modified by the presence of the second condensate. I will come back to this point in § 6.4.1. These measurements also show that there is no significant difference in the lifetime of the sample with and without  $^{41}\text{K}$ : this means that the three-body loss rate is not enhanced by the presence of two species, consistently with the small overlap of the two clouds outlined in section 6.1.

However, given this little overlap, the observed shift is somewhat surprising. Numerical integration of the 3D Gross-Pitaevskii equation with a  $s = 11$  vertical lattice shows that the overlap is restricted to 1 lattice site

out of 11. Generalizing to a 3D lattice, we expect that approximately only 10% of sites are simultaneously filled with both  $^{87}\text{Rb}$  and  $^{41}\text{K}$  atoms. For this reason, one might doubt that the shift is genuinely related to the interspecies interaction. In order to check that this is indeed the case, we repeat the experiment with lower magnetic confinement to increase the differential sag of the two samples (1.48). Once the double-species condensate is achieved, we relax the harmonic frequencies of the magnetic trap to  $\omega_{\perp} = 2\pi \times 108 \text{ Hz}$  and  $\omega_z = 2\pi \times 9.2 \text{ Hz}$ , thereby increasing the vertical separation to  $11 \mu\text{m}$ , more than the summed radii of the condensates that remain well separated even with the additional confinement of the lattice beams. The results for the visibility of the Bragg peaks and the width of the central peak are shown in figure 6.15: as we can see, although the visibility is somewhat lower and the increase of the central peak width is sharper in presence of  $^{41}\text{K}$ , the change in this two parameters takes place at the same lattice height. By fitting the visibility decay as in the case of small overlap we obtain

$$\begin{aligned} s_{c0} &= 16.4(0.6)(1.6) & s_{c1} &= 15.3(0.4)(1.5) \\ \alpha_0 &= 0.51(14) & \alpha_1 &= 0.51(8) \end{aligned}$$

and this time the difference is consistent with zero and the exponent in the deep lattice limit is the same within the experimental uncertainties. We note that in this configuration the critical temperature for  $^{41}\text{K}$  is even lower due to the reduced trap frequency: since however no thermal component of  $^{41}\text{K}$  can be detected, repeating the above reasoning we can set an upper limit for the temperature to  $50 \text{ nK}$ . The corresponding condensed fraction for  $^{87}\text{Rb}$  is above 95% and the presence of the thermal cloud becomes completely negligible.

These results prove that indeed the effect shown in figure 6.13 is due to the interaction between the  $^{87}\text{Rb}$  and the  $^{41}\text{K}$  condensate. Furthermore the most trivial explanations, either related to non-adiabatic effects or to other processes that precede the loading of the lattice, are ruled out by our experimental observations. However no simple arguments exist to relate the observed large shift in the onset of the loss of phase coherence to the small overlap between the two clouds. Increasing this overlap would require to reduce the mutual repulsion between the two species: this can be done –as we have seen in § 3.2– using a Feshbach resonance. Experimental efforts are underway at the moment of my writing to assess the position of these resonance and preliminary results will be presented in chapter 7.

Nevertheless the experimental observations demand a theoretical anal-

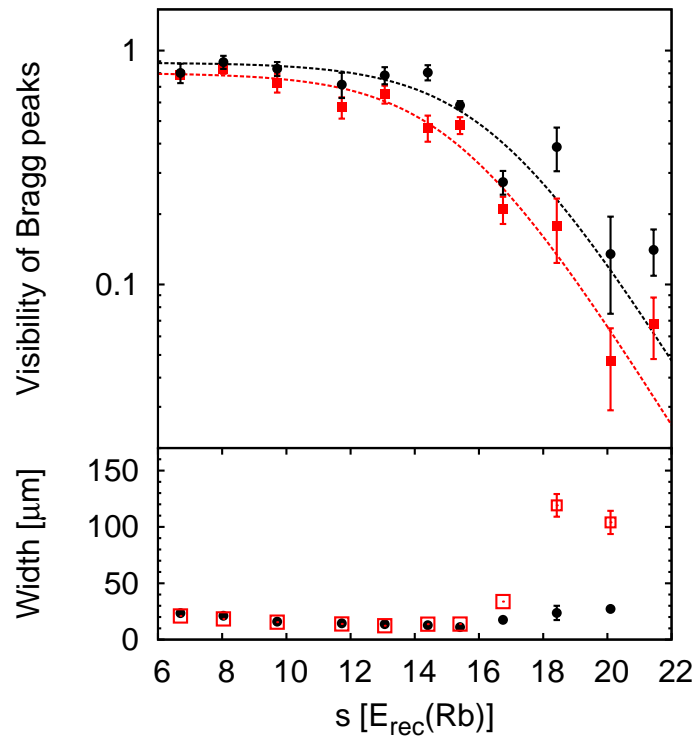


**Figure 6.15.** Visibility of the Bragg peaks of  $^{87}\text{Rb}$  as a function of  $s$  with (squares) and without (dots)  $^{41}\text{K}$  in a weak magnetic trap. Error bars are statistical fluctuation over around 5 measures and where not shown are smaller than point size. Dashed lines are a fit according to Eq. (6.14).

ysis, which is more intriguing since the effect is somehow unexpected. I will discuss the possible explanation in the following section.

## 6.4 Theoretical scenarios

Our experimental findings augment those of the attractive Fermi-Bose mixture [135, 136] to repulsive bosonic impurities and help to shine some light on the induced loss of coherence, whose origin has so far remained unclear, if not controversial.

Among the causes of this shift of the loss of coherence only those related to finite temperature can be translated from fermionic to bosonic impurities. Other explanations such as disorder induced by localized fermions cannot apply to our case since our impurities are superfluid and therefore delocalized. Obviously our experiment does not have any direct implication for the Fermi-Bose case but certainly it pushes the theoretical analysis to look for explanations that can be valid in both cases.

One of the most surprising results shown in previous section is that the observed loss of coherence occurs with a very limited overlap between the two clouds: this in sharp contrast both with the fermionic case and with several theoretical analysis which usually take the interspecies interaction as weak (see § 5.3). As we pointed out above, we think that the ultimate answer to the questions raised by our experimental observation can come only after a systematic analysis of the system as a function of the interspecies scattering length and hence of the overlap. Nevertheless, several hypotheses can provide a partial explanation our results: unfortunately none of them is conclusive but each of them is worth further studies.

### 6.4.1 The issue of finite temperature

The first and most immediate explanation for the loss of phase coherence could follow from heating of the two clouds when the lattice ramps up. Besides technical noise, which plays a role only at longer timescales, we consider the effect of the thermodynamic transformation involved.

The entropy of a Bose gas condensate in a harmonic trap in the Thomas-Fermi regime can be obtained from the energy per particle which, for  $t = T/T_c < 1$ , can be expressed as the sum of two contribution, one is identical to that of the ideal gas and the second depends on the interaction. To the

lowest order in the interaction one has [44, 42]:

$$\frac{E}{N k_B T_c} = \frac{3\zeta(4)}{\zeta(3)} t^4 + \frac{1}{7} \eta (1 - t^3)^{2/5} (5 + 16t^3), \quad (6.15)$$

where  $\zeta$  is the Riemann zeta function and the interaction term is linear in the quantity

$$\eta = \alpha \left( N^{1/6} \frac{a}{\bar{a}_{ho}} \right)^{2/5} \quad (6.16)$$

which is the ratio between the zero temperature chemical potential (2.17) and the critical temperature of the ideal trapped Bose gas (1.23). In the above expression  $\alpha = 15^{2/5} \zeta^{1/3}(3)/2 \simeq 1.57$ ,  $a$  –as in chapter 1– the intraspecies scattering length and  $N$  is the *total* number of atoms including the non-condensed fraction.

From Eq. (6.15) this expression one can obtain the entropy from the known relation [67]

$$\frac{\partial S}{\partial T} = \frac{1}{T} \frac{\partial E}{\partial T}$$

The resulting expression for the entropy of the trapped gas is given by

$$\frac{S}{N k_B} = \frac{4\zeta(4)}{\zeta(3)} t^3 + \frac{6}{7} \eta \int_0^t du u \left[ 8(1 - u^3)^{2/5} - \frac{5 + 16u^3}{5(1 - u^3)^{3/5}} \right], \quad (6.17)$$

where the interacting contribution must be evaluated numerically.

If the lattice is so weak that the system is very well superfluid, a reasonable approximation is to replace the actual mass by the effective mass of the particles in the lattice and continue to consider the gas as harmonically trapped. As it is shown in figure 6.16, increasing the lattice height increases the effective mass and hence  $\eta$ : in order to keep the entropy constant, the reduced temperature  $T/T_c$  decreases, thereby increasing the superfluid fraction of the system. This effect is augmented by the compression induced by the spatial profile of the beams as per Eq. (1.18), since it also increases the entropy.

If one goes to higher lattice, the effect of the shell structure become significant: in this range entropy is confined in sites with number fluctuations i.e. in superfluid shells [145, 146]. As we pointed out in § 5.2.3, the shape of the superfluid shell is very sensitive to the external confinement. The compression induced by the ramping up of the lattice might give rise to a strong increase in the temperature of the system and possibly a reduction of its superfluid fraction. At zero temperature in the limit  $J \rightarrow 0$ , the radius

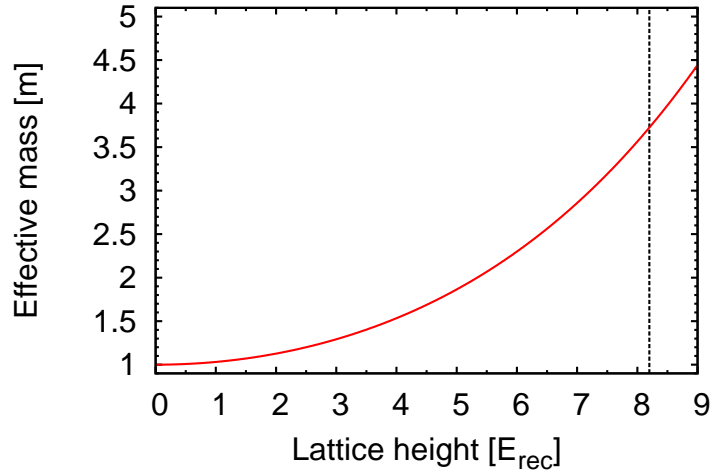


**Figure 6.16.** Effective mass in the ground state of the lattice as a function of the lattice height. Vertical line marks the lattice height for which in  $^{87}\text{Rb } U/(6J) \simeq 1$ .

of the  $n^{\text{th}}$ -shell is given by [124, 145]

$$R_i^{(n)} = \frac{1}{\omega_i} \left( \frac{2(\mu - nU)}{m} \right)^{1/2}, \quad (6.18)$$

where  $\mu$  is the chemical potential at the trap center. The effect of finite temperature is to blur the step between the different shells up to the point in which the gas reverts to its normal state. Based on a simple approximation which takes into account excitation in the form of particle-hole pairs, it is possible to show that the system is still in a Mott insulator state if  $T < T^* \simeq 0.2U$  [146]. For a  $^{87}\text{Rb}$  condensate in a lattice with  $s = 20$  one finds  $T^* \simeq 8 \text{ nK}$ .

In the presence of tunneling however the situation is simplified by the presence of the superfluid layers between the Mott insulating domains. Considering a spherical trap with frequency  $\bar{\omega}$ , one finds that the total entropy associated with the shell structure, for  $k_B T < U$  is [145]

$$S_{\text{shell}}/k_B = \frac{32\pi^3}{3} \frac{k_B T}{m\bar{\omega}^2 \lambda_L^3} \sum_j R^{(j)}. \quad (6.19)$$

From this expression it is possible to calculate the final temperature reached by the atoms in the lattice. In figure 6.17 we report the entropy per particle as a function of temperature for  $^{87}\text{Rb}$ , as obtained from Eq. (6.17) and Eq. (6.19) for  $s = 20$ . The parameters used in the calculation are obtained

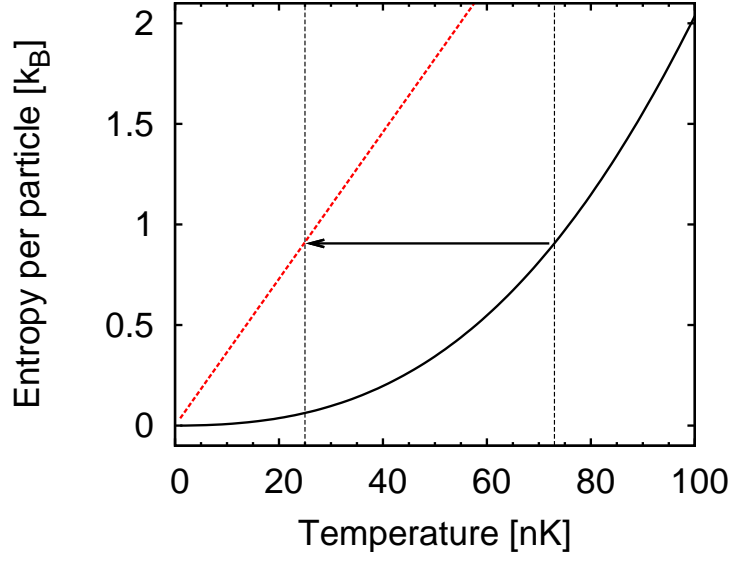


**Figure 6.17.** Entropy per particle as a function of temperature for a harmonically trapped condensate in the Thomas-Fermi approximation (continuous line) and for a inhomogeneous Mott insulator (dashed line) in a lattice with  $s = 20$ . The arrow marks the reduction of the temperature following the adiabatic loading in the lattice.

as follows. The compression generated the lattice is taken into account by introducing in Eq. (1.18) the waists of our lattice beams obtaining:

$$\begin{aligned}\omega_z &= 2\pi \sqrt{16.8^2 + 7.66^2} \text{ s} \text{ Hz} \\ \omega_{\perp} &= 2\pi \sqrt{202^2 + 11.9^2} \text{ s} \text{ Hz}\end{aligned}\quad (6.20)$$

The chemical potential is obtained from a site decoupling simulation fixing the total number of atoms obtained from the estimation of the condensed fraction given above. For  $N = 3.7 \times 10^4$  we have  $\mu = 1.85 E_{\text{rec}}$ .

As we can see from figure 6.17, the adiabatic loading may result in a reduction or an increase of the final temperature depending on the initial one. For an initial temperature of 73 nK, considering for the moment  $^{87}\text{Rb}$  alone, the loading in the lattice results in a reduction of the temperature to about  $T_f = 25$  nK: this means that our treatment is self consistent since  $T_f < U/k_B \simeq 38$  nK. Beside this it is worth remarking that, since entropy is conserved, the thermal fraction (which is the fraction contributing to the entropy) should be constant as well.

With two species, however, the two entropies change at different rates and thermal equilibrium requires an interspecies redistribution of entropy. In our experiment, this increases the entropy of  $^{87}\text{Rb}$  and therefore reduces

its condensed fraction: it might be the case that this reduction accounts for the observed loss of phase coherence. Quantitatively, due to the small overlap, we neglect the interspecies interaction energy and calculate the total entropy as the sum of two independent contributions. At  $s = 0$ , each of the two gases contributes with Eq. (6.17). At  $s = 20$   $[U/(6J)]_K \simeq 0.75$  and therefore, for  $^{41}\text{K}$ , we can apply Eq. (6.17) with the replacement  $m \rightarrow m^* = 4.16 m$  while for  $^{87}\text{Rb}$  it is legitimate to use Eq. (6.19). The final temperature of the mixture and the entropies of the two gas are obtained imposing conservation of entropy and thermal equilibrium:

$$\begin{cases} S_K(0) + S_{Rb}(0) &= S_K(20) + S_{Rb}(20) \\ T_K(20) &= T_{Rb}(20) \end{cases} \quad (6.21)$$

For an initial temperature of 73 nK, which –as we pointed out above– corresponds to a  $^{87}\text{Rb}$  thermal fraction of 20%, the presence of  $^{41}\text{K}$  increases the  $^{87}\text{Rb}$  entropy, hence its thermal fraction, by 20%. As a consequence, the  $^{87}\text{Rb}$  condensed fraction decreases, at most, from 80% to 75% and the visibility by approximately the same amount [112]. It is worth noting that also in this case the obtained final temperature  $T(20) = 29$  nK is lower than  $U/k_B$  and therefore our approach is self consistent. We conclude that this is a minor effect, unable to account for the observed relevant loss of coherence.

### 6.4.2 Effective potentials

The first naive explanation can be obtained from a crude mean field approximation of the interaction term Eq. (5.23). If one consider that potassium is superfluid at all the lattice heights considered in the experiment, a mean field version of the interaction term can be written as

$$H_{int} = V \sum_i \psi_{K i} \hat{n}_{Rb i} = \sum_i \tilde{\mu}_i \hat{n}_{Rb i}.$$

In this form it is straightforward to identify the interaction term as a correction to the local chemical potential: since for our mixture  $V > 0$ , the local chemical potential is increased. The case of commensurate 1 + 1 filling for the  $^{87}\text{Rb}$ - $^{41}\text{K}$  mixture is considered theoretically in [34] but, in sharp contrast with our experiment, calculations are made for a uniform system and the interspecies scattering length is considered such that the overlap is perfect. In this condition the authors of [34] observe that the transition to the Mott insulator phase occurs for deeper lattice opposite to what we observe in our experiment.

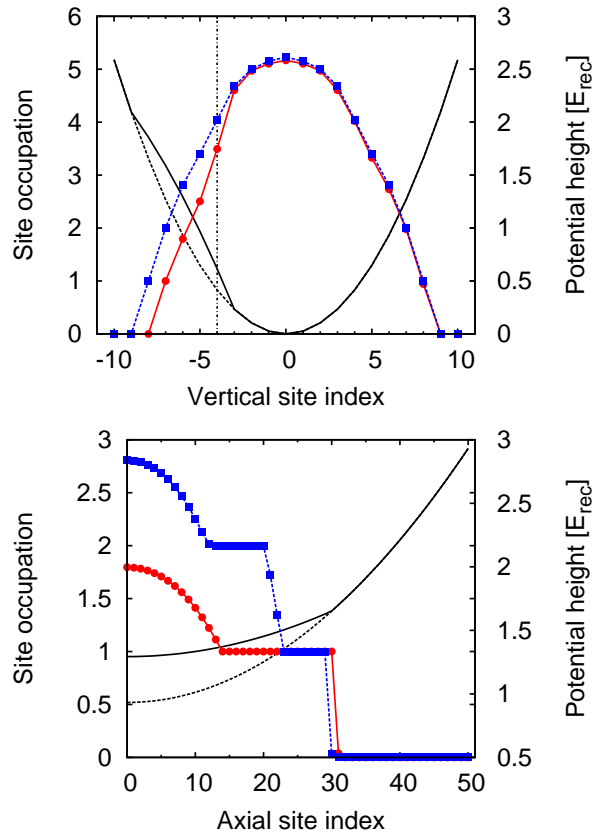


**Figure 6.18.** Cross section of the effective potential seen by  $^{87}\text{Rb}$  in presence (continuous black line) and in absence (dashed black line) of a frozen distribution of  $^{41}\text{K}$  atoms and corresponding density distribution (dots, continuous line and squares, dashed line respectively). The upper plot is taken along the vertical axis, while the lower one is taken along the axial direction at the vertical position marked by the dot-dashed line. The chemical potential is slightly different in the two cases in order to have the same number of atoms within 0.5%.

However, if in presence of harmonic confinement, the situation can be more complicated. Looking at figure 5.4, one sees that not necessarily increasing the chemical potential leads to an increase of the superfluid fraction. Considering the potassium condensate as a static perturbation, the problem for  $^{87}\text{Rb}$  is mapped on an inhomogeneous problem in which the potential is not purely harmonic but reflects the density distribution of  $^{41}\text{K}$  as shown in figure 6.18. In the same figure I report the corresponding density distribution as obtained within the site decoupling approximation: the effect on the density distribution is sizable, but if we compute the superfluid fraction we see only a minor change unable to account for the experimental observation.

The exact result when the potassium distribution is not frozen but is repelled from the  $^{87}\text{Rb}$  distribution is not easy to predict. From very general consideration one should expect no simple answer but whether the superfluid fraction increases or decreases depends on the trapping geometry of *both* species [147]. A theoretical analysis that takes these effects into account is way beyond the experimental character of this thesis. However I think that a further insight into this problem could be helpful also because it could allow a comparison with the fermionic case in which the interspecies interaction is attractive and therefore modifies the trapping potential in the opposite way.

### 6.4.3 Polarons

Here I want to address the last theoretical scenario which can help to understand our experimental findings, especially with respect to the small overlap between the two clouds. This treatment is based on two fundamental assumptions that are verified in our system:

1. Rubidium can be described by a Bose-Hubbard model, while potassium is deep in the superfluid region where the Gross-Pitaevskii equation is still meaningful
2. in the overlap region the coupling between the two clouds is weak because of the reduced density and in spite of the large cross section.

#### The model

The Hamiltonian of the system at our lattice heights can be written as a sum of three contributions: one for each of the two species plus an interaction term. In the spirit of the above mentioned assumption (1), the Hamiltonian of potassium can be taken as Eq. (1.26), while that for  $^{87}\text{Rb}$  is given by the Bose-Hubbard model Eq. (5.8). To work in the grand canonical ensemble a term  $-\hat{\Psi}^\dagger(\mathbf{r}) \mu_K \hat{\Psi}(\mathbf{r}) (-\mu_{Rb} \sum_i \hat{n}_i)$  is added to the potassium (rubidium) Hamiltonian. The interaction term is readily found remembering Eq. (5.7):

$$\mathcal{H}_{int} = g_{12} \hat{\Psi}^\dagger(\mathbf{r}) \hat{\Psi}(\mathbf{r}) |w(\mathbf{r})|^2 \hat{n}, \quad (6.22)$$

where the coupling  $g_{12}$  is that introduced in § 1.3 and it is related to the interspecies scattering length by Eq. (3.9). In this model it is possible to show that  $^{87}\text{Rb}$  atoms interact with the  $^{41}\text{K}$  condensate by creating excitations in the condensate [148]. These excitations “dress” the  $^{87}\text{Rb}$  atoms

and the tunneling of these dressed atoms is slower: this might be at the origin of the observed loss of coherence<sup>5</sup>.

If the effective coupling between the condensate and the tunneling atoms is weak enough, the fluctuations of the condensate from the unperturbed ground state can be considered small and treated with the Bogoliubov approach introduced in § 1.2. It becomes then possible to diagonalize the complete Hamiltonian on a basis of quasiparticles consisting in a <sup>87</sup>Rb atom and a coherent cloud of excitations of the <sup>41</sup>K condensate [148]. These compound objects are reminiscent of polarons in solid-state physics and, as their solid state counterpart, can be characterized by a energy shift which is given by [148]:

$$E_p = \frac{1}{\Omega} \sum_{\mathbf{q}} g_{12}^2 \frac{n_0 \epsilon(\mathbf{q})}{\hbar^2 \omega_{\mathbf{q}}^2} |f(\mathbf{q})|^2. \quad (6.23)$$

In Eq. (6.23)  $\Omega$  is the quantization volume of the system,  $\epsilon(\mathbf{q}) = \hbar \mathbf{q}^2 / (2m_K)$ ,  $\hbar \omega_{\mathbf{q}}$  is the Bogoliubov spectrum and  $f(\mathbf{q})$  is the Fourier transform of the absolute square of the Wannier function:

$$f(\mathbf{q}) = \int_{\Omega} d\mathbf{r} |w(\mathbf{r})|^2 \exp(i\mathbf{q} \cdot \mathbf{r}).$$

In order to obtain an analytic expression for  $E_p$ , I will use the Bogoliubov spectrum of an homogeneous condensate, given by Eq. (1.36) and take for the Wannier function the ground state of the harmonic approximation of the lattice well. Introducing these approximations Eq. (6.23) becomes:

$$E_p = \frac{g_{12}^2}{(2\pi)^{3/2} g_K \xi_K^2 \sigma_w} \frac{1}{\sigma_w} \left( 1 - \sqrt{2\pi} \frac{\sigma_w}{\xi_K} \right), \quad (6.24)$$

where  $\xi_K = \hbar / \sqrt{2mg_K n_K}$  is the healing length already introduced in Eq. (1.44),  $\sigma_w = \lambda s^{-1/4} / (2\pi)$  is the second moment of the real space Wannier function and the above equation is approximated to the order  $(\sigma_w / \xi_K)^2$ .

The dynamics of the polarons depend on the ratio between the temperature and  $E_p$  [148]. For  $k_B T \ll E_p$  the system dynamics can be described by the coherent hopping of polarons with a renormalized tunneling energy given by  $\tilde{J} = J \exp(-S)$ . Within the above mentioned approximations one finds

$$S \simeq \frac{1}{16\pi^2} \left( \frac{g_{12}}{g_K} \right)^2 \frac{\lambda}{n_K \xi_K^4} \quad (6.25)$$

where  $n_K$  is the peak density of the <sup>41</sup>K condensate. On the other hand, for  $k_B T \gg E_p$ , one has that the Bogoliubov excitation undergo incoherent

<sup>5</sup>A similar tentative explanation was also suggested by T. Hänsch.

scattering as the  $^{87}\text{Rb}$  atoms tunnel. Under these conditions the damping of the tunneling rate becomes much more severe and one has [148]

$$\tilde{J} \simeq J^2 \frac{\exp(-E_p/(k_B T))}{\hbar(k_B T E_p)^{1/2}}. \quad (6.26)$$

### The actual experiment

I first check whether the weak coupling condition introduced above is applicable to our case. This might seem at first counter-intuitive since, as we saw in § 6.1, the interspecies repulsion is so strong that induces phase separation between the two condensates. However, for our number of potassium atoms, the density is weak enough that the coupling with  $^{87}\text{Rb}$  represents a perturbation.

More quantitatively the weak coupling is justified if the mean field energy of the  $^{41}\text{K}$  condensate is bigger than the interaction energy with  $^{87}\text{Rb}$  [148]:

$$g_{12} \ll 2\sqrt{2} g_K n(\mathbf{r}) \xi^3(\mathbf{r}) \sim \frac{\hbar^3}{\sqrt{m^3 g_K n(\mathbf{r})}} \sim \frac{\hbar^3}{\sqrt{m^3 g_K n_K}} \quad (6.27)$$

which is equivalent to

$$a_{12} \sqrt{a_K n_K} \ll \left[ 4\pi^{3/2} \left( 1 + \frac{m_{\text{Rb}}}{m_K} \right) \right]^{-1} \simeq 0.02.$$

For our experimental parameters:

$$a_{12} \sqrt{a_K n_K} = a_{12} \sqrt{\frac{1}{8\pi} \frac{m\bar{\omega}}{\hbar} \left( \frac{15 N_K a}{\bar{a}_{ho}} \right)^{1/5}} \simeq 0.003.$$

In the previous equation we made use of Eq. (1.30) and Eq. (1.32) and set  $\bar{\omega} = 2\pi \times 128 \text{ Hz}$  and  $N_K = 2 \times 10^3$ . As we can see the weak coupling approximation is well verified at the center of the condensate but is less and less valid as we approach the edge: given that the overlap between our two condensates is marginal the approximation in our case is only weakly verified. I will come back on this point below.

A similar calculation for the polaron energy yields  $E_p \simeq 1 \text{ nK}$  at  $s = 10$ . We are therefore in the regime at which polarons undergo incoherent scattering and one expects a strong reduction of the tunneling according to Eq. (6.26). For comparison we calculated that the coherent contribution given by Eq. (6.25) is almost negligible. This proves that indeed the incoherent scattering of the  $^{41}\text{K}$  condensate excitations associated to the tunneling of  $^{87}\text{Rb}$  atoms might indeed play a role in our experiment. However,

before claiming that this is the cause of the observed loss of coherence and initiate further investigation aimed at experiments related to polaron physics (see for example [149]), several questions must be answered from the theoretical side. First of all the weak coupling approximation is not very well verified at the edge of the condensate and this requires a more complicated approach, second the presence of the lattice is neglected for  $^{41}\text{K}$  as it is that of the harmonic trap for  $^{87}\text{Rb}$  and third the Bogolioubov spectrum is calculated for a homogeneous condensate which is far from the experimental situation. Last it should be noted that, although the condensate excitations are intrinsically collective and therefore explain how the entire condensate is affected by a local perturbation induced by the  $^{87}\text{Rb}$  atoms, this should at least introduce some cutoff in the wavelength of the excitations summed in Eq. (6.23). By the same token it remains obscure how a perturbation of the tunneling in a marginal region can affect a global property of the  $^{87}\text{Rb}$  gas such as the visibility of the interference pattern. About this issue it has been suggested that, since  $^{87}\text{Rb}$  is close to a quantum phase transition, the influence of boundary condition may become overwhelming [150], but an experimental challenge of this hypothesis is at least cumbersome.

In summary our experimental observation of a loss of phase coherence induced by the presence of a small condensate of another species even in the presence of a small overlap opened several scenario that deserve further investigation, both from the experimental and on the theoretical point of view. From the experimental side, the most obvious step is get rid of this reduced overlap and look how the effect change if the two species are perfectly overlapped: to realize this however, the use of a Feshbach resonance to tune the interspecies interaction is a fundamental tool.



## Chapter 7

# The quest for Feshbach resonances

As it was clearly pointed out in § 6.4, a loss of coherence induced by the presence of a second superfluid was observed in a Bose-Einstein condensate of  $^{87}\text{Rb}$  even though the overlap between the two is only limited. This finding is in sharp contrast to the prediction of [34] which is done for perfectly overlapped gas. For this reason it is very important to acquire the experimental capability of tuning the interspecies scattering length: as shown in § 3.2, this can be done by tuning a uniform magnetic field across a Feshbach resonance.

Heteronuclear Feshbach resonances in the mixture  $^{40}\text{K}$ - $^{87}\text{Rb}$  were among the first to be observed [17], and recently several resonances of this mixture were identified [71, 72]. These determinations allowed to create accurate models of interspecies collisions and, more interesting to us, to predict the position of Feshbach resonances also for the  $^{41}\text{K}$ - $^{87}\text{Rb}$  mixture [71, 72]. However, no experimental determination of these resonances exists so far and therefore, before thinking to any experiment in which interactions can be controlled, these resonances must be found experimentally.

In this chapter I will present preliminary results on the position of two low-field Feshbach resonances of the  $^{41}\text{K}$ - $^{87}\text{Rb}$  mixture. This work ideally concludes the build-up phase of the new apparatus which can now fully explore the physics it was designed for. Before the results are actually presented I will introduce the detail of the experimental setup.

## 7.1 Experimental procedure

The Feshbach field is generated by the same coils that are used for the 3D-MOT and the quadrupole trap. However, in order to generate a uniform magnetic field the current direction in one of the two coils is switched with an electro-mechanical relay. The current flowing in the coil is measured with a high precision Hall probe: the first task we accomplished is a calibration of the probe output as a function of the magnetic field. Since Feshbach resonance are exploited by tuning a homogeneous magnetic field they are intrinsically incompatible with magnetic trapping. For this reason, to calibrate the magnetic field, atoms are held into a 1D optical lattice simply obtained shining only the axial beam with a higher power ( $s \sim 100$ ). The calibration consists in measuring the frequency  $\nu_{21}$  of the  $|2, 2\rangle \rightarrow |1, 1\rangle$  hyperfine transition. In a uniform magnetic field  $B$  the frequency of this transition is given by:

$$\nu_{12} = \langle 1, 1 | A(\mathbf{I} \cdot \mathbf{J}) + (\mu_B/h)(2\mathbf{S} + \mathbf{J} + g_N\mathbf{I}) \cdot \mathbf{B} | 2, 2 \rangle, \quad (7.1)$$

where the first term is the hyperfine splitting which is diagonal on the  $|F, m_F\rangle$  basis,  $\mu_B$  is the Bohr magneton and  $g_N$  is the nuclear magnetic moment in units of  $\mu_B$  which for  $^{87}\text{Rb}$  is  $1.4984 \times 10^{-3}$  [151]. By plugging the right values in Eq. (7.1) one obtains

$$\nu_{12} = \nu_0/2 + \alpha B + \sqrt{\nu_0^2/4 + \beta B + \gamma B^2} \simeq \nu_0 + 1.5 \mu_B B, \quad (7.2)$$

where  $\nu_0$  is the hyperfine separation and the numerical constants are given by

$$\alpha = 1.4006 \text{ MHz/G} \quad \beta = 4779.3 \text{ MHz}^2/\text{G} \quad \gamma = 1.9559 \text{ MHz}^2/\text{G}^2.$$

After this preliminary step we transferred atoms into a crossed optical trap realized with the axial and horizontal beam of the optical lattice. We found out that the position of the waist of the beam is more critical for a single beam trap than for a 1D lattice and therefore this parameter was carefully adjusted by changing the position of the last lens. As we expected from Eq. (1.10) the trap aspect ratio is very big and therefore the trap acts more like a waveguide letting the atoms expand along the axis of the beam: this is clearly shown in figure 7.1(a) where we plot the density distribution of the atoms a few ms after releasing them from the magnetic to the optical trap. The second beam is aligned to minimize the size of the trapped atoms at a constant temperature thereby maximizing the trapping frequency. A

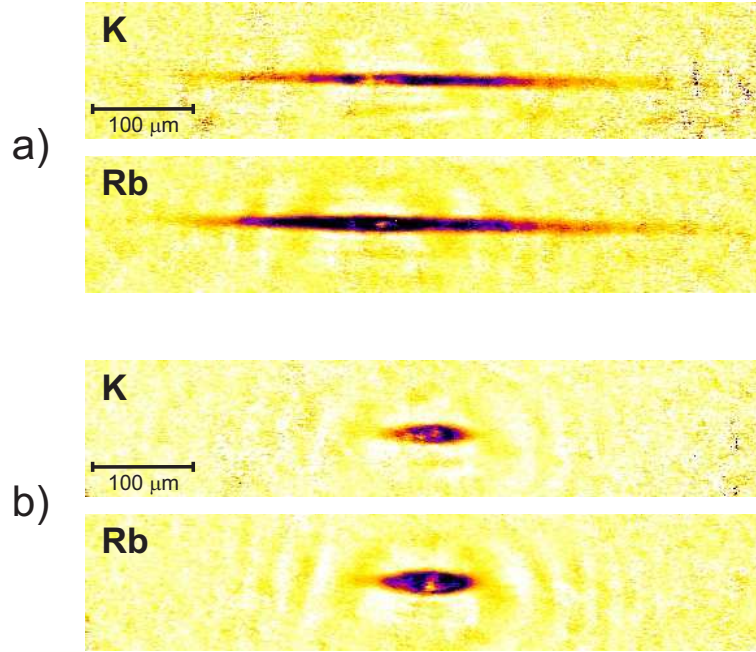


**Figure 7.1.** Absorption images taken in situ inside a single beam dipole trap (a) and a crossed dipole trap (b). The temperature in both cases is around 600 nK. Note that in the case of the single beam trap atoms are still expanding along the axis.

typical picture of the atoms trapped by the crossed dipole trap is shown in figure 7.1(b). The lifetime of the atoms at a temperature slightly below  $1 \mu\text{K}$  is found to be  $22(3)\text{s}$  and the heating rate is less than  $10\text{nK/s}$  with a power of  $2.87\text{W}$  ( $1.43\text{W}$ ) on the axial (radial) beam. We checked that we can control the depth of the trap without displacing the atoms by evaporating the hottest atoms. In order to do that we reduce the laser power so that higher energy atoms experience the effect of gravity and are outcoupled from the trap (see figure 1.3). In this configuration we could easily make a Bose-Einstein condensate of  $^{41}\text{K}$ .

As we pointed out in § 3.2, if both species are in the  $|2, 2\rangle$  state Feshbach resonances cannot occur since the  $\{22, 22, 00\}$  channel is not coupled to any other channel <sup>1</sup>. In order to avoid spin relaxation it is necessary to prepare the mixture in a state which gives rise to a single open channel. The best candidate is the absolute ground state  $\{11, 11, 00\}$ , as it is shown in table 3.2. In order to prepare the desired states the atoms are transferred with a Landau-Zeener sweep across the hyperfine transition. For  $^{87}\text{Rb}$  the frequency is given by Eq. (7.2), while for  $^{41}\text{K}$  the formula is the

<sup>1</sup>Neglecting the weak coupling due to the spin spin interactions (see § 3.2).

same but the hyperfine separation is  $\nu_0(41) = 254.014 \text{ MHz}$  [152], the nuclear magnetic moment is  $g_N(41) = 1.17022 \times 10^{-5}$  [151] and the numerical coefficient obtained from Eq. (7.1) are

$$\alpha = 1.400 \text{ MHz/G} \quad \beta = 177.75 \text{ MHz}^2/\text{G} \quad \gamma = 1.9587 \text{ MHz}^2/\text{G}^2.$$

For the very first measurements, the frequency for the two species is obtained from a synthesized sweeper whose signal is fed into the same amplifier used for the evaporation in the case of  $^{87}\text{Rb}$  and a fixed frequency generator mixed with a low-frequency modulation fed into a 7W broadband amplifier (PHA-4000) for  $^{41}\text{K}$ . It took several weeks of optimization to find the proper antenna to efficiently couple the output amplifier with the atoms. At the end the best solution was to use a single coil tuned around 300 MHz by means of variable capacitors and to eliminate the mixer to gain some extra power: instead of sweeping the microwave frequency at a constant magnetic field one sweeps the magnetic fields keeping the frequency constant. This solution proved effective also for  $^{87}\text{Rb}$ .

The complete experimental sequence is therefore the following: the atoms are transferred from the magnetic into the dipole trap and a uniform magnetic field is turned on around 40 G to lift the degeneracy among the hyperfine levels. Then, in order to avoid dipolar relaxation,  $^{87}\text{Rb}$  is transferred into the  $|1, 1\rangle$  state and the atoms remaining in  $|2, 2\rangle$  ( $< 15\%$ ) are swept away from the trap with a pulse of resonant light. After this stage a similar sequence of transferring and cleaning is applied to  $^{41}\text{K}$ , leaving both species in the desired state.

## 7.2 Preliminary results

Soon after the beginning of the experimental search for the resonances predicted in the  $0 \div 100 \text{ G}$  range, we realized that, probably due to some residual and unidentified ferromagnetic impurity inside the vacuum chamber, our magnetic field is plagued by a gradient of  $5.3 \text{ G/cm}$  at a field of 46 G. The gradient has significant components both in the axial direction and along the vertical. The gradient value was measured by looking at the Zeeman shift given by Eq. (7.2) as a function of the coil position (which we can vary with the translation stage), while the direction was inferred from the perturbation of the free fall of the atoms.

The magnetic field gradient introduces a linear potential which acts in the same way as gravity in Eq. (1.13) and therefore lowers the depth of our

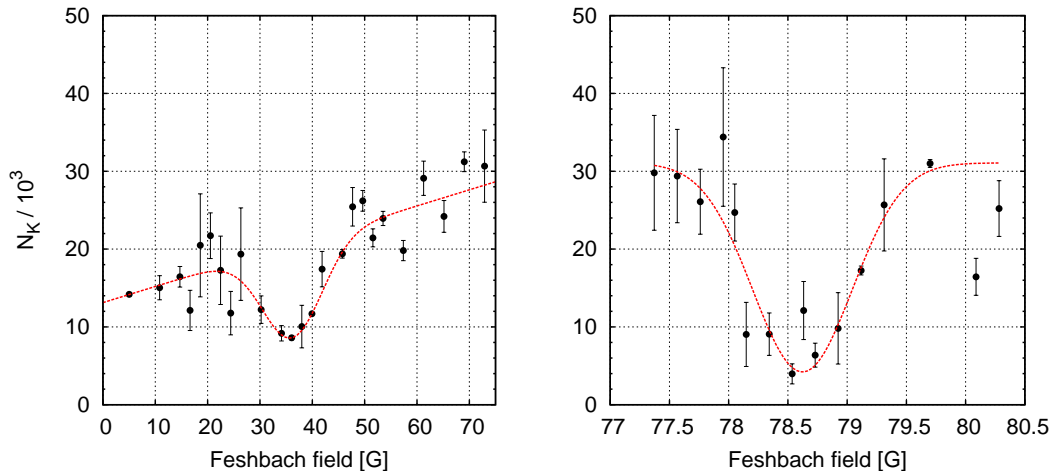


**Figure 7.2.** Number of  $^{41}\text{K}$  atoms as a function of the constant magnetic field. The dashed line is a Gaussian fit. The linear background on the left picture is due to residual noise in the loop controlling the magnetic field at low value of the control voltage.

dipolar trap. We indeed found a position of the coil in which the gradient is minimum, but this position is field-dependent and therefore is not suitable to search for Feshbach resonances which requires to change the field by several gauss. We therefore revert back to the 1D optical lattice where we made the first observation of loss feature compatible with the three body losses induced by a Feshbach resonance. However, for reasons that are still under investigation at the time of my writing, the signal looks very broad. For this reason we decided to modify the design of our dipole trap to increase the confinement and therefore increase the trap depth (see figure 1.3).

After this key improvement a clear signal of the two resonances was found as it is shown in figure 7.2. The experimental sequence is the following: one the mixture is prepared in its absolute ground state as described in the previous section, the Feshbach field is placed at a value in which no resonances are present and then it is ramped in 40 ms to the desired value where it is left on for 1 s. At the end of this sequence the number of atoms of both species is measured after expansion in the usual way. In order to be sure that the observed feature is indeed dependent on the presence of the two species we checked that no losses of  $^{41}\text{K}$  are detected without  $^{87}\text{Rb}$ .

The experimental determination of the center of the two resonances is

$$B_{40} = 36.2(0.5)(0.6) \text{ G} \quad B_{80} = 78.62(0.06)(0.9) \text{ G}.$$

Clearly the loss feature associated to the high-field resonance is narrower

than that of the low-field one. The first error quoted above is statistical and comes from the fit while the second is systematic and comes from the field calibration. These results are compared with a coupled channel calculation based on the existing measurements on other isotopic combinations [153]. The relevant molecular level scheme for our input channel is shown in figure 7.3 for the magnetic field range that we explored. As we can see two levels cross the threshold giving rise to two different Feshbach resonances: furthermore since the crossing slope is different, we expect a different strength of the resonance which explains the different width of the loss feature observed in the experiment. From the accurate computation of the level scheme it is possible to determine the expected position of the two resonances with great accuracy. The expected values are

$$B_{40} = 39.4(4) \quad B_{80} = 78.93(5) \text{ G}.$$

As we can see, the agreement between the theoretical calculation and our measurements is excellent for one of the resonance and moderate for the other one. This small discrepancy will be further investigated by measuring the zero crossing i.e. the value of the magnetic field at which the scattering length is zero: as we can see from figure 7.3, one of these positions is expected around 85 G and the other around 75 G. These positions can be measured independently from the resonance center and provide a further comparison between theory and experiment. Note that, in the single resonance approximation, a measurement of the zero crossing gives an estimate of the resonance width  $\Delta$  appearing in Eq. (3.22). Measurements in this direction are underway at the moment of my writing and will allow a further stringent test of the collisional model used for calculations.

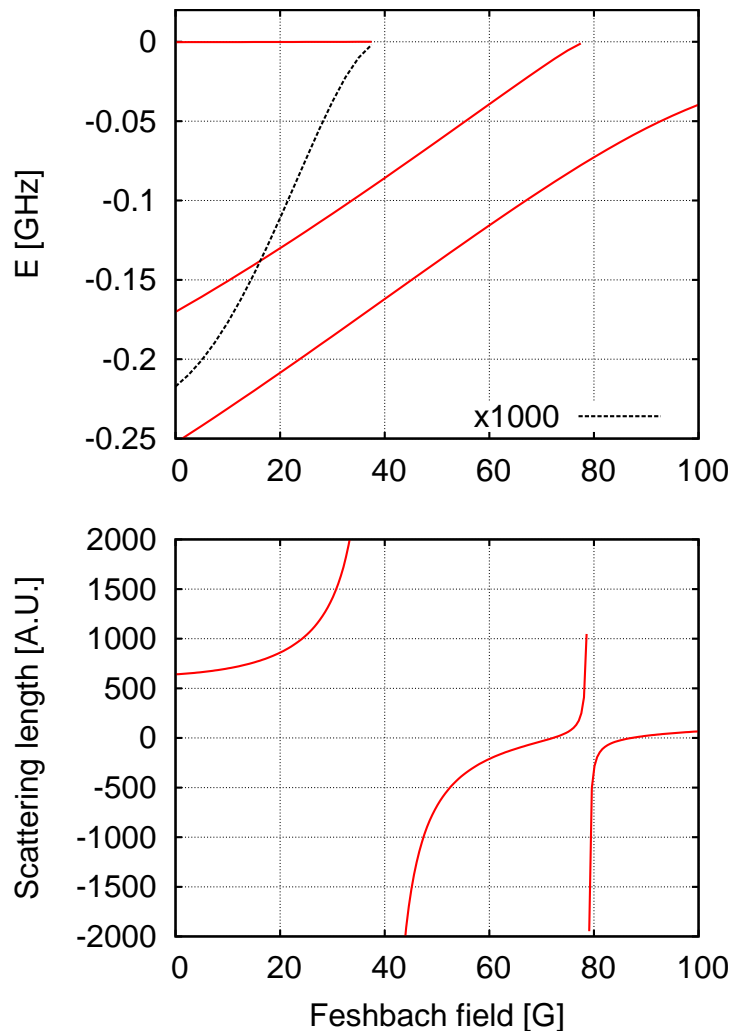


**Figure 7.3.** Molecular levels for the absolute ground state of the  $^{87}\text{Rb}$ - $^{41}\text{K}$  mixture (top): every time that a molecular level crosses the threshold the scattering length diverges (bottom). The dashed line in the top plot represents the energy of the first crossing level multiplied by  $10^3$ . The third level crosses the threshold around 555 G. Calculations by A. Simoni.



# Conclusions

Un poème n'est jamais achevé. C'est toujours un accident qui le termine, c'est-à-dire qui le donne au public.

(Paul Valéry)

“A poem is never finished. It's always an accident that puts an end to it, namely that gives it to its audience”: I think that this quotation of the French writer Paul Valéry might well be adapted to PhD theses and especially to this one. Many interesting work could be done on the Bose-Bose mixture of  $^{87}\text{Rb}$ -and  $^{39}\text{K}$  or  $^{41}\text{K}$  and the feeling is that, at the end of these three years of work, although we know a bit more than when the experiment started from an empty room with a few blueprints and some laser sources, yet more question arose than we could find answer to. On one hand this means that we worked well, enabling the exploration of a field that was left behind, but on the other hand this means that not all the questions that came from the experiments are answered in this thesis.

Among the question that are positively solved is the problem of building an apparatus for the efficient and stable production of two Bose-Einstein condensates. This apparatus has been described in chapter 2 and it is based on two important elements: two bright sources of ultracold atoms (2D-MOT) that allow the independent control on the loading of the two species and a novel kind of Ioffe-Pritchard magnetic trap operating in vacuum. Ideally the build-up of the apparatus is completed by the results presented in chapter 7. These results about interspecies Feshbach resonances, beside the scientific importance in the field of ultracold collision that they have *per se*, pave the way to the control of the interspecies interactions in the  $^{41}\text{K}$ - $^{39}\text{K}$  mixture. With the addition of this last “knob” everything is ready to begin the journey toward the physics of heteronuclear bosonic molecules in an optical lattice.

Another question that found a positive solution, though not by us, is

the possibility to bring  $^{39}\text{K}$  to the degenerate regime. Even if the challenge was taken and won by another experiment at LENS, our work on the collisional properties of this isotope, presented in chapter 4 was instrumental in acquiring the know-how necessary to obtain this result.

More open questions are left by our initial work on degenerate Bose-Bose mixtures in an optical lattice, presented in chapter 6. Indeed we showed that even a small amount of a second superfluid, with a small overlap, induces a loss of phase coherence in the first condensate. Several possible causes were taken into account but no one of them could explain entirely the observed phenomena. Actually the incoherent scattering of the second condensate excitations driven by the tunneling of the atoms of the first species can play a very important role in destroying the phase coherence. However, a definitive answer to this question requires a further effort from the theoretical side that certainly would benefit from a more thorough experimental characterization. Again, a great improvement in the experiments will be given by the possibility to tune the interspecies interactions and hence the overlap between the two clouds.

Access the regime of negligible interspecies interaction can open the possibility of exploring the phase diagram of the two species Bose-Hubbard model that could so far receive attention only from the theoretical point of view (see § 5.3). In particular one could try to observe the two elusive phases of super-counterflow and pairing-superfluidity which have never been observed experimentally and depend crucially on the presence of two different condensates. This could help to shine light on the problem of pairing superfluidity which is a “hot” topic for the physics of ultracold fermions and beyond. Beside this, along the line of ultracold molecules, the increase of the overlap is a necessary step toward the creation of single heteronuclear molecule in each lattice site. It is worth mentioning that anyway these results will require to understand all the mechanisms underlying the dynamics of the bosons in the optical lattice: with this respect, our observation of a loss of phase coherence opens important scenarios that will be extensively explored in the future.

# Bibliography

- [1] M. INGUSCIO, S. STRINGARI AND C. WIEMAN, eds. *Proceedings of the International School of Physics Enrico Fermi, Course CXL: Bose – Einstein condensation in gases*. IOS Press, Amsterdam, 1999.
- [2] R. P. FEYNMAN. “Quantum mechanical computers”. *Opt. News* **11** 11 (1985).
- [3] R. P. FEYNMAN. “Quantum mechanical computers”. *Found. Phys.* **16** 507 (1986).
- [4] S. LLOYD. “Universal quantum simulators”. *Science* **273** 1073 (1996).
- [5] I. BLOCH. “Ultracold quantum gases in optical lattices”. *Nature Physics* **1** 23 (2005).
- [6] M. GREINER, O. MANDEL, T. ESSLINGER, T. W. HÄNSCH AND I. BLOCH. “Quantum phase transition from a superfluid to a Mott insulator in a gas of ultracold atoms”. *Nature* **415** 39 (2001).
- [7] T. STÖFERLE, H. MORITZ, C. SCHORI, M. KÖHL AND T. ESSLINGER. “Transition from a strongly interacting 1d superfluid to a Mott insulator”. *Phys. Rev. Lett.* **92** 130403 (2004).
- [8] B. PAREDES, A. WIDERA *et al.* “Tonks-Girardeau gas of ultracold atoms in an optical lattice”. *Nature* **429** 277 (2004).
- [9] Z. HADZIBABIC, P. KRÜGER, M. CHENEAU, B. BATTELIER AND J. DALIBARD. “Berezinskii-Kosterlitz-Thouless crossover in a trapped atomic gas”. *Nature* **441** 1118 (2006).
- [10] C. J. MYATT, E. A. BURT, R. W. GHRIST, E. A. CORNELL AND C. E. WIEMAN. “Production of two overlapping Bose-Einstein condensates by sympathetic cooling”. *Phys. Rev. Lett.* **78** 586 (1997).
- [11] B. DEMARCO AND D. S. JIN. “Onset of Fermi degeneracy in a trapped atomic gas”. *Science* **285** 1703 (1999).
- [12] F. SCHRECK, L. KHAYKOVICH *et al.* “Quasipure Bose-Einstein condensate immersed in a Fermi sea”. *Phys. Rev. Lett.* **87** 080403 (2001).
- [13] Z. HADZIBABIC, C. A. STAN *et al.* “Two-species mixture of quantum degenerate Bose and Fermi gases”. *Phys. Rev. Lett.* **88** 160401 (2002).
- [14] C. SILBER, S. GÜNTHER, C. MARZOK, B. DEH, P. W. COURTEILLE AND C. ZIMMERMANN. “Quantum-degenerate mixture of fermionic lithium and bosonic rubidium gases”. *Phys. Rev. Lett.* **95** 170408 (2005).
- [15] G. ROATI, F. RIBOLI, G. MODUGNO AND M. INGUSCIO. “Fermi-Bose quantum degenerate  $^{40}\text{K}$ - $^{87}\text{Rb}$  mixture with attractive interaction”. *PRL* **89** 150403 (2002).

- [16] G. MODUGNO, G. FERRARI, G. ROATI, R. J. BRECHA, A. SIMONI AND M. INGUSCIO. “Bose-Einstein condensation of potassium atoms by sympathetic cooling”. *Science* **294** 1320 (2001).
- [17] S. INOUE, J. GOLDWIN, M. L. OLSEN, C. TICKNOR, J. L. BOHN AND D. S. JIN. “Observation of heteronuclear Feshbach resonances in a mixture of bosons and fermions”. *Phys. Rev. Lett.* **93** 183201 (2004).
- [18] C. A. STAN, M. W. ZWIERLEIN, C. H. SCHUNCK, R. S. M. F. AND W. KETTERLE. “Observation of Feshbach resonances between two different atomic species”. *Phys. Rev. Lett.* **93** 143001 (2004).
- [19] A. SIMONI, F. FERLAINO, G. ROATI, G. MODUGNO AND M. INGUSCIO. “Magnetic control of the interaction in ultracold K-Rb mixtures”. *Phys. Rev. Lett.* **90** 163202 (2003).
- [20] G. MODUGNO, G. ROATI, F. RIBOLI, F. FERLAINO, R. J. BRECHA AND M. INGUSCIO. “Collapse of a degenerate Fermi gas”. *Science* **297** 2240 (2002).
- [21] C. OSPELKAUS, S. OSPELKAUS, K. SENGSTOCK AND K. BONGS. “Interaction-driven dynamics of  $^{40}\text{K}$ - $^{87}\text{Rb}$  fermion-boson gas mixtures in the large-particle-number limit”. *Phys. Rev. Lett.* **96** 020401 (2006).
- [22] G. MODUGNO, M. MODUGNO, F. RIBOLI, G. ROATI AND M. INGUSCIO. “Two atomic species superfluid”. *Phys. Rev. Lett.* **89** 190404 (2002).
- [23] C. A. REGAL, C. TICKNOR, J. L. BOHN AND D. S. JIN. “Creation of ultracold molecules from a Fermi gas of atoms”. *Nature* **424** 47 (2003).
- [24] K. E. STRECKER, G. B. PARTRIDGE AND R. G. HULET. “Conversion of an atomic Fermi gas to a long-lived molecular Bose gas”. *Phys. Rev. Lett.* **91** 080406 (2003).
- [25] J. HERBIG, T. KRAEMER *et al.* “Preparation of a pure molecular quantum gas”. *Science* **301** 1510 (2003).
- [26] K. XU, T. MUKAIYAMA, J. R. ABO-SHAER, J. K. CHIN, D. E. MILLER AND W. KETTERLE. “Formation of quantum-degenerate sodium molecules”. *Phys. Rev. Lett.* **91** 210402 (2003).
- [27] S. DÜRR, T. VOLZ, A. MARTE AND G. REMPE. “Observation of molecules produced from a Bose-Einstein condensate”. *Phys. Rev. Lett.* **92** 020406 (2004).
- [28] M. GREINER, C. A. REGAL AND D. S. JIN. “Emergence of a molecular Bose-Einstein condensate from a Fermi gas”. *Nature* **426** 537 (2003).
- [29] S. JOCHIM, M. BARTENSTEIN *et al.* “Bose-Einstein condensation of molecules”. *Science* **302** 2101 (2003).
- [30] G. THALHAMMER, K. WINKLER, F. LANG, S. SCHMID, R. GRIMM AND J. H. DENSCHLAG. “Long-lived Feshbach molecules in a three-dimensional optical lattice”. *Phys. Rev. Lett.* **96** 050402 (2006).
- [31] F. SCHREK. “Feshbach resonances in a fermionic mixture of lithium and potassium”. Talk at ICTP summer school on novel quantum phases (2007).
- [32] M. TAGLIEBER, A.-C. VOIGT, T. AOKI, T. HÄNSCH AND K. DIECKMANN. “Quantum degenerate two-species Fermi-Fermi mixture coexisting with a Bose-Einstein condensate”. ArXiv:0710.2779v1 [cond-mat.other].

- 
- [33] E. WILLE, F. SPIEGELHALDER *et al.* “Exploring an ultracold Fermi-Fermi mixture: Interspecies Feshbach resonances and scattering properties of  ${}^6\text{Li}$  and  ${}^{40}\text{K}$ ”. ArXiv:0711.2916v1 [cond-mat.other].
- [34] B. DAMSKI, L. SANTOS *et al.* “Creation of a dipolar superfluid in optical lattices”. *Phys. Rev. Lett.* **90** 110401 (2003).
- [35] J. DALIBARD AND C. COHEN-TANNOUDJI. “Atomic motion in laser light: connection between semiclassical and quantum descriptions”. *Journal of Physics B: Atomic and Molecular Physics* **18** 1661 (1985).
- [36] D. BOIRON, A. MICHAUD *et al.* “Cold and dense cesium clouds in far-detuned dipole traps”. *Phys. Rev. A* **57** R4106 (1998).
- [37] C. FORT, A. BAMBINI *et al.* “Cooling mechanisms in potassium magneto-optical traps”. *Eur. Phys. J. D* **3** 113 (1998).
- [38] A. BAMBINI AND A. AGRESTI. “Radiative cooling force in atoms with multiplet structure”. *Phys. Rev. A* **56** 3040 (1997).
- [39] R. GRIMM, M. WEIDEMULLER AND Y. B. OVCHINIKOV. “Optical dipole trap for neutral atoms”. *Adv. At., Mol., Opt. Phys.* **42** 95 (2000).
- [40] G. VAROQUAUX, N. ZAHZAM *et al.* “I.C.E.: An ultra-cold atom source for long-baseline interferometric inertial sensors in reduced gravity” (2007). Presentation at the Rencontres de Moriond: Gravitational Waves and Experimental Gravity.
- [41] A. EINSTEIN. “Quantentheorie des einatomigen idealen Gases. Zweite Abhandlung”. *Sitz. Kgl. Preuss. Akad. Wiss.* 3 (1925).
- [42] F. DALFOVO, S. GIORGINI, L. P. PITAEVSKII AND S. STRINGARI. “Theory of Bose-Einstein condensation in trapped gases”. *Rev. of Mod. Phys.* **71** 463 (1999).
- [43] J. M. GREBOWSKY AND J. P. MCKELVEY. “Density-of-states function for the harmonic oscillator: A simple and direct approach”. *American Journal of Physics* **35** 352 (1967).
- [44] S. GIORGINI, L. P. PITAEVSKII AND S. STRINGARI. “Thermodynamics of a trapped Bose-condensed gas”. *J. of Low Temp. Phys.* **109** 309 (1997).
- [45] L. PITAEVSKII AND S. STRINGARI. *Bose-Einstein condensation*. Clarendon Press, 2003.
- [46] E. A. DONLEY, N. R. CLAUSSEN, S. L. CORNISH, J. L. ROBERTS, E. A. CORNELL AND C. E. WIEMAN. “Dynamics of collapsing and exploding Bose-Einstein condensates”. *Nature* **412** 295 (2001).
- [47] F. RIBOLI AND M. MODUGNO. “Topology of the ground state of two interacting Bose-Einstein condensates”. *Phys. Rev. A* **65** 063614 (2002).
- [48] P. AO AND S. T. CHUI. “Binary Bose-Einstein condensate mixtures in weakly and strongly segregated phases”. *Phys. Rev. A* **58** 4836 (1998).
- [49] J. CATANI. *A new apparatus for ultracold K-Rb Bose-Bose atomic mixtures*. Ph.D. thesis, Università di Firenze (2006).
- [50] J. CATANI, P. MAIOLI, L. DE SARLO, F. MINARDI AND M. INGUSCIO. “Intense slow beams of bosonic potassium isotopes”. *Phys. Rev. A* **73** 033415 (2006).
- [51] T. E. BARRETT, S. W. DAPORE-SCHWARTZ, M. D. RAY AND G. P. LAFYATIS. “Slowing atoms with  $\sigma^-$  polarized light”. *Phys. Rev. Lett.* **67** 3483 (1991).

- [52] Z. T. LU, K. L. CORWIN, M. J. RENN, M. H. ANDERSON, E. A. CORNELL AND C. E. WIEMAN. “Low-velocity intense source of atoms from a magneto-optical trap”. *Phys. Rev. Lett.* **77** 3331 (1996).
- [53] K. DIECKMANN, R. J. C. SPREEUW, M. WEIDEMÜLLER AND J. T. M. WALRAVEN. “Two-dimensional magneto-optical trap as a source of slow atoms”. *Phys. Rev. A* **58** 3891 (1998).
- [54] W. WOHLLEBEN, F. CHEVY, K. MADISON AND J. DALIBARD. “An atom faucet”. *Eur. Phys. J. D* **15** 237 (2001).
- [55] J. SCHOSER, A. BATÄR *et al.* “Intense source of cold Rb atoms from a pure two-dimensional magneto-optical trap”. *Phys. Rev. A* **66** 023410 (2002).
- [56] M. PREVEDELLI, F. S. CATALIOTTI *et al.* “Trapping and cooling of potassium isotopes in a double-magneto-optical-trap apparatus”. *Phys. Rev. A* **59** 886 (1999).
- [57] S. CHAUDHURI, S. ROY AND C. S. UNNIKRISHNAN. “Realization of an intense cold Rb atomic beam based on a two-dimensional magneto-optical trap: Experiments and comparison with simulations”. *Phys. Rev. A* **74** 023406 (2006).
- [58] P. A. MOLENAAR, P. VAN DER STRATEN, H. G. M. HEIDEMAN AND H. METCALF. “Diagnostic technique for Zeeman-compensated atomic beam slowing: technique and results”. *Phys. Rev. A* **55** 605 (1997).
- [59] W. H. WING. “On neutral particle trapping in quasistatic electromagnetic fields”. *Progr. in Quant. Elec.* **8** 181 (1984).
- [60] C. W. E.A. CORNELL, J.R. ENSHER. “Experiments in dilute atomic Bose-Einstein condensation”. In M. INGUSCIO, S. STRINGARI AND C. WIEMAN, eds., *Proceedings of the International School of Physics Enrico Fermi, Course CXL: Bose – Einstein condensation in gases*, 15–66. IOS Press, Amsterdam, 1999.
- [61] W. KETTERLE AND N. J. VAN DRUTEN. “Evaporative cooling of trapped atoms”. In B. BEDERSON AND H. WALTHER, eds., *Advances in Atomic, Molecular and Optical Physics*, volume 37, 181–236. Academic Press, San Diego, 1996.
- [62] T. BERGEMAN, G. EREZ AND H. J. METCALF. “Magnetostatic trapping fields for neutral atoms”. *PRA* **35** 1535 (1987).
- [63] R. WANG, M. LIU, F. MINARDI AND M. KASEVICH. “Reaching  $^7\text{Li}$  quantum degeneracy with a minitrap”. *Phys. Rev. A* **75** 013610 (2007).
- [64] M. GREINER, I. BLOCH, T. W. HÄNSCH AND T. ESSLINGER. “Magnetic transport of trapped cold atoms over a large distance”. *Phys. Rev. A* **63** 031401 (2001).
- [65] H. J. LEWANDOWSKI, D. M. HARBER, D. L. WHITAKER AND E. A. CORNELL. “Observation of anomalous spin-state segregation in a trapped ultracold vapor”. *Phys. Rev. Lett.* **88** 070403 (2002).
- [66] Parker-Hannifin GmbH. *Synchronous servo motor*. Technical manual.
- [67] K. HUANG. *Statistical Mechanics*. Wiley, Hoboken, 1988, 2 edition.
- [68] W. KETTERLE, D. DURFEE AND D. STAMPER-KURN. “Making, probing and understanding Bose-Einstein condensates”. In M. INGUSCIO, S. STRINGARI AND C. WIEMAN, eds., *Proceedings of the International School of Physics Enrico Fermi, Course CXL: Bose – Einstein condensation in gases*, 67–176. IOS Press, Amsterdam, 1999.

- [69] Y. CASTIN AND R. DUM. “Bose-Einstein condensates in time dependent traps”. *Phys. Rev. Lett.* **77** 5315 (1996).
- [70] G. BARONTINI. *Miscela di bosoni ultra-freddi in una nuova trappola magnetica: raffreddamento simpatico  $^{39}\text{K}$ - $^{87}\text{Rb}$* . Master’s thesis, Università degli Studi di Firenze (2006).
- [71] F. FERLAINO, C. D’ERRICO *et al.* “Feshbach spectroscopy of a K-Rb atomic mixture”. *PRA* **73** 040702(R) (2006).
- [72] F. FERLAINO, C. D’ERRICO *et al.* “Erratum: Feshbach spectroscopy of a K-Rb atomic mixture”. *Phys. Rev. A* **74** 039903(E) (2006).
- [73] G. ROATI, M. ZACCANTI *et al.* “ $^{39}\text{K}$  Bose-Einstein condensate with tunable interactions”. *Phys. Rev. Lett.* **99** 010403 (2007).
- [74] L. D. LANDAU AND E. M. LIFSHITZ. *Quantum mechanics, non-relativistic theory*. Pergamon press, Oxford, 1976, 3 edition.
- [75] J. DALIBARD. “Collisional dynamics of ultra-cold atomic gases”. In M. INGUSCIO, S. STRINGARI AND C. WIEMAN, eds., *Proceedings of the International School of Physics Enrico Fermi, Course CXL: Bose – Einstein condensation in gases*. IOS Press, Amsterdam, 1999.
- [76] E. FERMI. “Sul moto dei neutroni nelle sostanze idrogenate”. *La ricerca scientifica* (II serie) **2** 13 (1936).
- [77] G. F. GRIBAKIN AND V. V. FLAMBAUM. “Calculation of the scattering length in atomic collisions using the semiclassical approximation”. *Phys. Rev. A* **48** 546 (1993).
- [78] I. BLOCH, J. DALIBARD AND W. ZWERGER. “Many-body physics with ultracold gases”. arxiv:0704.3011.
- [79] E. G. M. VAN KEMPEN, S. J. J. M. F. KOKKELMANS, D. J. HEINZEN AND B. J. VERHAAR. “Interisotope determination of ultracold rubidium interactions from three high-precision experiments”. *Phys. Rev. Lett.* **88** 093201 (2002).
- [80] H. WANG, A. N. NIKOLOV *et al.* “Ground-state scattering lengths for potassium isotopes determined by double-resonance photoassociative spectroscopy of ultracold  $^{39}\text{K}$ ”. *Phys. Rev. A* **62** 052704 (2000).
- [81] T. LOFTUS, C. A. REGAL, C. TICKNOR, J. L. BOHN AND D. S. JIN. “Resonant control of elastic collisions in an optically trapped Fermi gas of atoms”. *Phys. Rev. Lett.* **88** 173201 (2002).
- [82] L. DE SARLO, P. MAIOLI, G. BARONTINI, J. CATANI, F. MINARDI AND M. INGUSCIO. “Collisional properties of sympathetically cooled  $^{39}\text{K}$ ”. *Phys. Rev. A* **75** 022715 (2007).
- [83] C. D’ERRICO, M. ZACCANTI *et al.* “Feshbach resonances in ultracold  $^{39}\text{K}$ ”. *New Journal of Physics* **9** 223 (2007).
- [84] A. DEREVIANKO, J. F. BABB AND A. DALGARNO. “High-precision calculations of van der Waals coefficients for heteronuclear alkali-metal dimers”. *Phys. Rev. A* **63** 052704 (2001).
- [85] C. TICKNOR, C. A. REGAL, D. S. JIN AND J. L. BOHN. “Multiplet structure of Feshbach resonances in nonzero partial waves”. *Phys. Rev. A* **69** 042712 (2004).

- [86] V. V. FLAMBAUM, G. F. GRIBAKIN AND C. HARABATI. “Analytical calculation of cold-atom scattering”. *Phys. Rev. A* **59** 1998 (1999).
- [87] T. KÖHLER, K. GÓRAL AND P. S. JULIENNE. “Production of cold molecules via magnetically tunable Feshbach resonances”. *Reviews of Modern Physics* **78** 1311 (2006).
- [88] A. J. MOERDIJK, B. J. VERHAAR AND A. AXELSSON. “Resonances in ultracold collisions of  $^6\text{Li}$ ,  $^7\text{Li}$ , and  $^{23}\text{Na}$ ”. *Phys. Rev. A* **51** 4852 (1995).
- [89] F. H. MIES, E. TIESINGA AND P. S. JULIENNE. “Manipulation of Feshbach resonances in ultracold atomic collisions using time-dependent magnetic fields”. *Phys. Rev. A* **61** 022721 (2000).
- [90] N. NYGAARD, B. I. SCHNEIDER AND P. S. JULIENNE. “Two-channel R-matrix analysis of magnetic-field-induced Feshbach resonances”. *Phys. Rev. A* **73** 042705 (2006).
- [91] M. ANDERLINI AND D. GUÉRY-ODELIN. “Thermalization in mixtures of ultracold gases”. *Phys. Rev. A* **73** 032706 (2006).
- [92] G. DELANNOY, S. G. MURDOCH, V. BOYER, V. JOSSE, P. BOUYER AND A. ASPECT. “Understanding the production of dual Bose-Einstein condensation with sympathetic cooling”. *Phys. Rev. A* **63** 051602 (2001).
- [93] T. A. SAVARD, K. M. O’HARA AND J. E. THOMAS. “Laser-noise-induced heating in far-off resonance optical traps”. *Phys. Rev. A* **56** R1095 (1997).
- [94] C. R. MONROE, E. A. CORNELL, C. A. SACKETT, C. J. MYATT AND C. E. WIEMAN. “Measurement of Cs-Cs elastic scattering at  $T = 30\mu\text{K}$ ”. *Phys. Rev. Lett.* **70** 414 (1993).
- [95] M. ARNDT, M. BEN DAHAN, D. GUÉRY-ODELIN, M. W. REYNOLDS AND J. DALIBARD. “Observation of a zero-energy resonance in Cs-Cs collisions”. *Phys. Rev. Lett.* **79** 625 (1997).
- [96] N. R. NEWBURY, C. J. MYATT AND C. E. WIEMAN. “ $s$ -wave elastic collisions between cold ground-state  $^{87}\text{Rb}$  atoms”. *Phys. Rev. A* **51** R2680 (1995).
- [97] K. B. DAVIS, M.-O. MEWES, M. A. JOFFE, M. R. ANDREWS AND W. KETTERLE. “Evaporative cooling of sodium atoms”. *Phys. Rev. Lett.* **74** 5202 (1995).
- [98] B. DEMARCO, J. L. BOHN, J. P. BURKE, M. HOLLAND AND D. S. JIN. “Measurement of  $p$ -wave threshold law using evaporatively cooled fermionic atoms”. *Phys. Rev. Lett.* **82** 4208 (1999).
- [99] P. O. SCHMIDT, S. HENSLER *et al.* “Determination of the  $s$ -wave scattering length of chromium”. *Phys. Rev. Lett.* **91** 193201 (2003).
- [100] J. GOLDWIN, S. INOUE, M. L. OLSEN, B. NEWMAN, B. D. DEPAOLA AND D. S. JIN. “Measurement of the interaction strength in a Bose-Fermi mixture with  $^{87}\text{Rb}$  and  $^{40}\text{K}$ ”. *Phys. Rev. A* **70** 021601 (2004).
- [101] S. BRANDT. *Data Analysis: Statistical and Computational Methods for Scientists and Engineers*. Springer, 1998, 3 edition.
- [102] H. WU AND C. J. FOOT. “Direct simulation of evaporative cooling”. *J. Phys. B: At. Mol. Opt. Phys.* **29** L321 (1996).
- [103] G. A. BIRD. *Molecular gas dynamics and the direct simulation of gas flows*. Clarendon Press, Oxford, 1994.

- 
- [104] W. H. PRESS, B. P. FLANNERY, S. A. TEUKOLSKY AND W. T. VETTERLING. *Numerical Recipes in C: The Art of Scientific Computing*. Cambridge University Press, Cambridge, 1992, 2nd edition.
- [105] J. C. SLATER. "A soluble problem in energy bands". *Phys. Rev.* **87** 807 (1952).
- [106] O. MORSCH AND M. OBERTHALER. "Dynamics of Bose-Einstein condensates in optical lattices". *Reviews of Modern Physics* **78** 179 (2006).
- [107] J. HECKER DENSCHLAG, J. E. SIMSARIAN *et al.* "A Bose-Einstein condensate in an optical lattice". *Journal of Physics B: Atomic, Molecular and Optical Physics* **35** 3095 (2002).
- [108] N. W. ASHCROFT AND N. D. MERMIN. *Solid state physics*. Hartcourt College, Fort Worth, 1976.
- [109] D. JAKSCH, C. BRUDER, J. I. CIRAC, C. W. GARDINER AND P. ZOLLER. "Cold bosonic atoms in optical lattices". *PRL* **81** 3108 (1998).
- [110] B. EIERMANN, T. ANKER *et al.* "Bright Bose-Einstein gap solitons of atoms with repulsive interaction". *Phys. Rev. Lett.* **92** 230401 (2004).
- [111] L. FALLANI, L. DE SARLO *et al.* "Observation of dynamical instability for a bose-einstein condensate in a moving 1d optical lattice". *Phys. Rev. Lett.* **93** 140406 (2004).
- [112] F. GERBIER, A. WIDERA, S. FOLLING, O. MANDEL, T. GERICKE AND I. BLOCH. "Interference pattern and visibility of a mott insulator". *Phys. Rev. A* **72** 053606 (2005).
- [113] W. ZWERGER. "Mott-Hubbard transition of cold atoms in optical lattices". *Journal of Optics B: Quantum and Semiclassical Optics* **5** S9 (2003).
- [114] V. A. KASHURNIKOV, N. V. PROKOF'EV AND B. V. SVISTUNOV. "Revealing the superfluid-Mott-insulator transition in an optical lattice". *Phys. Rev. A* **66** 031601 (2002).
- [115] R. ROTH AND K. BURNETT. "Superfluidity and interference pattern of ultracold bosons in optical lattices". *Phys. Rev. A* **67** 031602 (2003).
- [116] P. PEDRI, L. PITAEVSKII *et al.* "Expansion of a coherent array of Bose-Einstein condensates". *Phys. Rev. Lett.* **87** 220401 (2001).
- [117] F. GERBIER, A. WIDERA, S. FOLLING, O. MANDEL, T. GERICKE AND I. BLOCH. "Phase coherence of an atomic Mott insulator". *Phys. Rev. Lett.* **95** 050404 (2005).
- [118] D. VAN OOSTEN, P. VAN DER STRATEN AND H. T. C. STOOF. "Quantum phases in an optical lattice". *Phys. Rev. A* **63** 053601 (2001).
- [119] K. SHESHADRI, H. R. KRISHNAMURTHY, R. PANDIT AND T. V. RAMAKRISHNAN. "Superfluid and insulating phases in an interacting-boson model: Mean-field theory and the RPA". *Europhys. Lett.* **22** 257 (1993).
- [120] G. PUPILLO, C. J. WILLIAMS AND N. V. PROKOF'EV. "Effects of finite temperature on the Mott-insulator state". *Phys. Rev. A* **73** 013408 (2006).
- [121] B. CAPOGROSSO-SANSONE, N. V. PROKOF'EV AND B. V. SVISTUNOV. "Phase diagram and thermodynamics of the three-dimensional Bose-Hubbard model". *Phys. Rev. B* **75** 134302 (2007).

- [122] M. P. A. FISHER, P. B. WEICHMAN, G. GRINSTEIN AND D. S. FISHER. “Boson localization and the superfluid-insulator transition”. *Phys. Rev. B* **40** 546 (1989).
- [123] F. ALET AND E. S. S. RENSEN. “Generic incommensurate transition in the two-dimensional boson Hubbard model”. *Phys. Rev. B* **70** 024513 (2004).
- [124] B. DEMARCO, C. LANNERT, S. VISHVESHWARA AND T.-C. WEI. “Structure and stability of Mott-insulator shells of bosons trapped in an optical lattice”. *Phys. Rev. A* **71** 063601 (2005).
- [125] A. B. KUKLOV AND B. V. SVISTUNOV. “Counterflow superfluidity of two-species ultracold atoms in a commensurate optical lattice”. *Phys. Rev. Lett.* **90** 100401 (2003).
- [126] A. KUKLOV, N. PROKOF'EV AND B. SVISTUNOV. “Commensurate two-component bosons in an optical lattice: Ground state phase diagram”. *Phys. Rev. Lett.* **92** 050402 (2004).
- [127] E. ALTMAN, W. HOFSTETTER, E. DEMLER AND M. D. LUKIN. “Phase diagram of two-component bosons on an optical lattice”. *New Journal of Physics* **5** 113 (2003).
- [128] A. ISACSSON, M.-C. CHA, K. SENGUPTA AND S. M. GIRVIN. “Superfluid-insulator transitions of two-species bosons in an optical lattice”. *Phys. Rev. B* **72** 184507 (2005).
- [129] T. MISHRA, R. V. PAI AND B. P. DAS. “Phase separation in a two-species Bose mixture”. *Phys. Rev. A* **76** 013604 (2007).
- [130] G.-H. CHEN AND Y.-S. WU. “Quantum phase transition in a multicomponent Bose-Einstein condensate in optical lattices”. *Phys. Rev. A* **67** 013606 (2003).
- [131] G.-P. ZHENG, J.-Q. LIANG AND W. M. LIU. “Phase diagram of two-species Bose-Einstein condensates in an optical lattice”. *Phys. Rev. A* **71** 053608 (2005).
- [132] L.-M. DUAN, E. DEMLER AND M. D. LUKIN. “Controlling spin exchange interactions of ultracold atoms in optical lattices”. *Phys. Rev. Lett.* **91** 090402 (2003).
- [133] A. KUKLOV, N. PROKOF'EV AND B. SVISTUNOV. “Superfluid-superfluid phase transitions in a two-component Bose-Einstein condensate”. *Phys. Rev. Lett.* **92** 030403 (2004).
- [134] S. FÖLLING, S. TROTZKY *et al.* “Direct observation of second-order atom tunnelling”. *Nature* **448** 1029 (2007).
- [135] S. OSPELKAUS, C. OSPELKAUS *et al.* “Localization of bosonic atoms by fermionic impurities in a three-dimensional optical lattice”. *Phys. Rev. Lett.* **96** 180403 (2006).
- [136] K. GÜNTER, T. STÖFERLE, H. MORITZ, M. KÖHL AND T. ESSLINGER. “Bose-Fermi mixtures in a three-dimensional optical lattice”. *Phys. Rev. Lett.* **96** 180402 (2006).
- [137] J. CATANI, L. DE SARLO, G. BARONTINI, F. MINARDI AND M. INGUSCIO. “Degenerate Bose-Bose mixture in a 3D optical lattice” (2007). Arxiv:0704.3011.
- [138] G. FERRARI, M. INGUSCIO, W. JASTRZEBSKI, G. MODUGNO, G. ROATI AND A. SIMONI. “Collisional properties of ultracold K-Rb mixtures”. *Phys. Rev. Lett.* **89** 053202 (2002).
- [139] P. L. GOULD, G. A. RUFF AND D. E. PRITCHARD. “Diffraction of atoms by light: The near-resonant Kapitza-Dirac effect”. *Phys. Rev. Lett.* **56** 827 (1986).

- 
- [140] M. KOZUMA, L. DENG *et al.* “Coherent splitting of Bose-Einstein condensed atoms with optically induced Bragg diffraction”. *Phys. Rev. Lett.* **82** 871 (1999).
- [141] J. STENGER, S. INOUE, A. P. CHIKKATUR, D. M. STAMPER-KURN, D. E. PRITCHARD AND W. KETTERLE. “Bragg spectroscopy of a Bose-Einstein condensate”. *Phys. Rev. Lett.* **82** 4569 (1999).
- [142] J. STENGER, S. INOUE, A. P. CHIKKATUR, D. M. STAMPER-KURN, D. E. PRITCHARD AND W. KETTERLE. “Erratum: Bragg spectroscopy of a Bose-Einstein condensate [Phys. Rev. Lett. 82, 4569 (1999)]”. *Phys. Rev. Lett.* **84** 2283 (2000).
- [143] M. BEN DAHAN, E. PEIK, J. REICHEL, Y. CASTIN AND C. SALOMON. “Bloch oscillations of atoms in an optical potential”. *Phys. Rev. Lett.* **76** 4508 (1996).
- [144] M. GREINER. *Ultracold quantum gases in three-dimensional optical lattice potentials*. Ph.D. thesis, Ludwig-Maximilians-Universität München (2003).
- [145] T.-L. HO AND Q. ZHOU. “Intrinsic heating and cooling in adiabatic processes for bosons in optical lattices”. *Phys. Rev. Lett.* **99** 120404 (2007).
- [146] F. GERBIER. “Boson Mott insulators at finite temperatures”. *Phys. Rev. Lett.* **99** 120405 (2007).
- [147] C. KOLLATH. Private communication (2007).
- [148] M. BRUDERER, A. KLEIN, S. R. CLARK AND D. JAKSCH. “Polaron physics in optical lattices”. *Phys. Rev. A* **76** 011605 (2007).
- [149] M. BRUDERER, A. KLEIN, S. R. CLARK AND D. JAKSCH. “Transport of strong-coupling polarons in optical lattices”. ArXiv:0710.4493v1 [quant-ph].
- [150] G. JONA-LASINIO. Private communication (2007).
- [151] N. E. HOLDEN. “Table of the isotopes”. In D. R. LIDE, ed., *CRC Handbook of Chemistry and physics*, 11–38. CRC Press, Boca Raton, Florida (USA), 1995, 76 edition.
- [152] E. ARIMONDO, M. INGUSCIO AND P. VIOLINO. “Experimental determinations of the hyperfine structure in the alkali atoms”. *Rev. of Mod. Phys.* **49** 31 (1977).
- [153] A. SIMONI. private communication (2006).



# Index

- 2SF, 125
- aspect ratio, 19
- attractive condensate, 26
- ballistic expansion, 71
- bar bending, 62
- Beer law, 68
- Bogolioubov spectrum, 27
- Brillouin zones, 112
- C6 potential, 80
- chemical potential, 26
- collapse, 26
- column density, 68
- cooling
  - time, 44
- D2 line, 16
- detuning, 14
- dichroic waveplate, 38
- dipole
  - crossed trap, 18
  - force, 14, 17
- effective range, 83
- epoxy, 40
- equation
  - Gross-Pitaevskii, 25
  - Bogolioubov-De Gennes, 27
- ergodic mixing, 100
- frame transfer, 69
- gravitational sag, 31
- hard sphere, 24
- harmonic oscillator
  - length, 23
- heating rate, 19
- Ioffe-Pritchard, 54
- isospin, 127
- jerk, 63
- magnification, 68
- Majorana spin-flip, 54
- optical lattice, 21
- optical molasses, 14
- parametric heating, 97
- phase shift, 78
- phase space density, 66
- PSMI, 125
- PSSF, 125
- quadrupole, 53
- quantum depletion, 26
- quasimomentum, 112
- radiation pressure, 14
- Raman-Nath, 141
- Rayleigh range, 18
- recoil
  - energy, 15
  - temperature, 15

run-away evaporation, 64

s, lattice height, 21

scattering

    amplitude, 78

    channel, 85

    length, 79

Sisyphus cooling, 15

spin-spin interaction, 86

TEM, 18

temperature

    critical, 23

    Doppler, 14

Thomas-Fermi, 25

trap depth, 20

trap frequencies

    average, 23

Wannier, 114

# Acknowledgments

This work is the outcome of three exciting years of work at the department of physics of the University of Florence in contiguity with the LENS. When I officially begun my thesis in January 2005 the lab was simply an empty room. If I could take part in the wonderful adventure that turned that empty room into a state-of-the-art laboratory working at the frontier of atomic physics, I owe it to my supervisor: prof. Massimo Inguscio. To him my gratitude first for believing in my qualities even when I doubted about them, second for giving me the opportunity to join his group where I met so many extraordinary people and last for trying to share with all of us his vision of science and the struggle for discovering something new even when everything, from technical difficulties to the wrong scientific policy of a nation, seems to cross all the efforts.

The BEC3 experiment I worked in is directed by dr. Francesco Minardi with whom I discussed every single piece of my work. I thank him for his legendary patience, his extraordinary culture and for having always helped me to look beyond the difficulties of the circumstances. I will not forget the many lessons I've learned from him and will keep as a treasure his many advices on atomic physics but also on the life in and outside the lab. Together with Francesco I've had the pleasure to work with two exceptional scientists who joined the BEC3 experiment as post-docs: Paolo Maioli and Gregor Thalhammer. I want to express my gratitude to both of them for the many things they taught me but most of all for sharing their passion for experimental physics.

I am deeply indebted to the two PhD students who worked with me during these years. First and foremost Jacopo Catani with whom I shared the hard times of the building up of everything: I bet that –like me– he cannot find a single thing that could be completed *exactly* as planned but every time I was glad he was there and indeed his dogged attitude helped me to overtake my limits and finally to achieve our objectives. Second, my “junior” partner Giovanni Barontini who proved himself a continuous source of surprises having often the right answer hidden beyond a humble disclaimer. I thank him for accepting *almost* every duty without complaints and for always be ready for discussions at every level, from field theories to mirror coating.

Finally I would like to thank all the members of the degenerate gases group at LENS, its director prof. Roberto Righini and all the technicians who contributed

so much to the build-up of the experiment often teaching lessons that I will never forget. I thank also professors Anna Vinattieri and Philippe Bouyer who accepted to report on the manuscript.

Adesso, in italiano, qualcosa di meno istituzionale: sono tante le persone che hanno reso questi anni un periodo straordinario che ha fatto di me, nonostante le tante difficoltà e gli inevitabili errori, una persona migliore. Non me ne vorranno gli altri se ancora ringrazio Massimo Inguscio per aver sempre uno sguardo al lato umano delle cose tanto che oggi, partire dal LENS mi pare un po' come lasciare una seconda casa. Ringrazio di cuore Francesco per i tanti consigli, su tutto, per aver sempre avuto una parola di conforto anche nei momenti di grande scoraggiamento. Un grazie di cuore a Paolo per tutto quello che ha fatto per me, per avermi sempre incoraggiato a fare le cose... *my way* e per avermi insegnato quanto l'umiltà sia importante anche e soprattutto dentro ad un laboratorio. Grazie a Gregor (so che può leggere anche in italiano) per le tante risate fatte insieme, per Python, per i Berner wurst e per avermi mostrato quanto Innsbruck è vicina, non solo geograficamente. Un grazie incredibile a Jacopo: non abbiamo parlato troppo io e lui, ma ogni volta sapevamo di poter contare uno sull'altro; senza di te non ce l'avrei mai fatta, tu lo sai, ma non me l'hai mai fatto pesare: grazie. Grazie a Giovanni, anche solo per quella "del cammello e della duna", grazie per questa amicizia che è venuta fuori un po' per caso un po' perché forse abbiamo in comune più di quel che sembra. Grazie agli altri membri di questo gruppo eccezionale, grazie a Chiara e a Leonardo che sono semplicemente unici e che davvero non dimenticherò mai, grazie a Giacomo, Marco e Giovanni e a Michele e Mattia, ma soprattutto un grazie ai miei amici dottorandi: Chiara, Matteo e Vera. Quando si dice essere sulla stessa barca... auguri per tutto, di cuore.

Grazie anche alla mia meravigliosa famiglia che ha sempre sopportato tutto, coperto tutto e sperato per il meglio: grazie dunque ai miei genitori, a Giulia, Antonio, Katja, Gabriele e naturalmente al piccolo Lorenzo. Grazie a Carlo ed Esther che si sono prodigati per assistere quella parte di me che rischiava di rimanere soffocata dalle preoccupazioni e grazie a tutti i vecchi amici, alcuni dei quali completano o stanno completando questa stessa fatica: Lorenzo, Antonio, Eleonora e Claudio, Matteo, Ludovico, Rodolfo, Luca, Tommaso, Nicola e tanti altri che sicuramente perdoneranno l'omissione.

Grazie Valentina, del resto, lo sai.

Luigi

Firenze, December 2007.